Modeling of delamination and interface strength in printed circuit boards

Essossinam Simlissi

THÈSE

présentée et soutenue publiquement le 13 décembre 2019
pour l'obtention du titre de :

Docteur de l'Université de Lorraine

Ecole Doctorale C2MP
Chimie-Mécanique-Matériaux-Physique

Spécialité : Sciences des Matériaux
Discipline : Mécanique des Matériaux

Par

Essossinam SIMLISSI

Modeling of delamination and interface strength in printed circuit boards

Composition du Jury:

Franck DELVARE, Professeur, Université de Caen-Normandie	Rapporteur
Laurent STAINIER, Professeur, Ecole centrale de Nantes	Rapporteur
Gregory COVAREL, Maître de Conférences, Université de Haute Alsace	Examinateur
Alexandrine GUEDON-GRACIA, Maître de Conférences, Université de Bordeaux	Examinateur
Jean-Marc RAULOT, Professeur, Université de Lorraine	Examinateur
Laurent BODIN, Directeur General, CIMULEC	Invité
Mohamed-Slim BAHI, Ingénieur de recherche, Université de Lorraine	Invité
Marion MARTINY, Professeur, Université de Lorraine	Directrice de Thèse
Sébastien MERCIER, Professeur, Université de Lorraine	Directeur de Thèse

Laboratoire d'Étude des Microstructures et de Mécanique des Matériaux
LEM3, UMR CNRS 7239, 7 rue Félix Savart 57073 Metz
Université de Lorraine – Pôle M4 : Matière, Matériaux, Métallurgie, Mécanique

REMERCIEMENT

Cette thèse est le fruit d'une collaboration entre le Laboratoire d'Etude des Microstructures et de Mécanique des Matériaux (LEM3) de l'Université de Lorraine (UL), CIMULEC fabriquant de Circuits Imprimés dans le cadre du Projet européen H2020 OUTCOME (European Union's Horizon2020 Programme, Excellent Science, Marie-Sklodowska-Curie Actions).

Je souhaite présenter mes remerciements aux membres du jury pour avoir accepté d'évaluer mes travaux. Merci à Laurent Stainier et Franck Delvare pour avoir accepté de rapporter cette thèse, ainsi qu'à Jean-Marc Raulot, Alexandrine Guedon-Gracia et Grégory Covarel pour avoir examiné mes travaux. La discussion avec l'ensemble du jury a soulevé un ensemble de suggestions importantes qui alimentent la poursuite des travaux.

J'adresse un grand merci à mes deux directeurs de thèse Marion Martiny et Sébastien Mercier pour l'accompagnement tout au long de ces trois années. Merci d'abord de m'avoir offert l'opportunité de faire cette thèse, merci aussi pour la confiance que vous m'avez accordée et pour m'avoir guidé toute au long de cette thèse. Votre bonne humeur, votre présence à mes côtés dans les moments difficiles de cette thèse, vos apports scientifiques m'ont permis de mener à bien ce travail. Un grand Merci également à José A. Rodríguez-Martínez le coordinateur du Projet OUTCOME de m'avoir accepté sur ce projet.

Mes remerciements vont également aux membres de CIMULEC, principalement Laurent Bodin, François Lechleiter et Sandrine Thomann, qui ont toujours été présents à mes côtés et m'ont permis à travers de nombreux échanges de comprendre les procédés de fabrication des circuits imprimés. Leur grande expérience fut précieuse pour m'expliquer les enjeux industriels liés à la tenue des interfaces. Je les remercie aussi pour le support technique lors de la réalisation des éprouvettes.

Merci également à Slim Bahi, Quentin Schenique et Gautier Girard pour l'aide précieuse apportée lors des essais expérimentaux au cours de cette thèse. Votre soutien a été fondamental pour le bon déroulement de ce travail.

Je profite aussi de cette occasion pour remercier tous les membres du laboratoire LEM3, la direction, les secrétaires, les doctorants et tous les chercheurs pour leur convivialité et leur soutien durant cette période de thèse. Merci aussi à mes amis doctorants du projet OUTCOME en France, en Espagne et en Israël avec qui j'ai partagé des moments chaleureux lors de nos rencontres.

Un grand merci à ma femme Marthe qui m'a soutenu et supporté pendant ces trois années de thèse. Merci également à mon ami et frère Christian Zogbekor qui depuis le Togo m'accorde toujours son soutien inconditionnel. Je remercie également et particulièrement mes camarades Togolais avec qui j'ai partagé des moments conviviaux et aussi tous ceux qui m'ont toujours soutenu malgré la distance.

Enfin je veux par cette occasion remercier toute ma famille, mes parents, mes frères, mes oncles, mes tantes qui par leur soutien de tous les jours m'ont permis d'aller jusqu'au bout de ce travail de recherche.

Je dédie cette thèse

à mes parents,

à Christian et mes frères,

à Marthe et Romuald.

Table of Contents

1 Préambule 1
1.1 Résumé de la thèse en Français 1
1.1.1 Introduction 1
1.1.2 Essais expérimentaux : pelage et traction 2
1.1.3 Théorie sur le pelage 5
1.1.4 Modèle Numérique 6
1.1.5 Résultats et discussion 7
1.1.6 Conclusion 9
1.2 General Introduction 11

2 STATE OF THE ART ON THE MECHANICS OF PEELING 15
2.1 Introduction 15
2.2 Peel test 16
2.3 Modeling of the peel test based on energy consideration 21
2.4 Numerical simulation 31
2.5 Conclusion 33

3 PEELING EXPERIMENT OF AN ELASTIC-PLASTIC THIN FILM ON AN ELASTIC SUBSTRATE 36
3.1 Introduction 36
3.2 Specimen materials 36
3.3 Specimen manufacturing 37
3.4 Uniaxial response copper thin film 38
3.5 Elastic behavior of the substrate 42
3.6 Peel test experiments 43
3.7 Conclusion 53

4 ELASTIC-PLASTIC ANALYSIS OF THE PEEL TEST FOR DUCTILE THIN FILM WITH SATURATION OF THE YIELD STRESS 55
4.1 Introduction 55
4.2 Configuration 55
4.3 Results 65
4.4 Conclusion 69

5 NUMERICAL MODELING OF PEELING 72
5.1 Introduction 72
5.2 Geometric configuration of peel test and cohesive elements 72
5.2.1 Position of the problem 72
5.2.2 Cohesive behavior 74
5.3 Material response based on a Voce hardening law 76
5.4 Application to copper used in the PCB industry 87
5.4.1 Elastic-plastic behavior 87
5.4.2 Effect of the peel angle 91
5.4.3 Effect of the film thickness on the peel force and on the film radius 93
5.4.4 Energy balance based on the numerical peel model 95
5.4.5 Evolution of the plastic strain in copper film 95
5.4.6 Mixed mode evaluation 96
5.5 Comparison between experiments and simulation 100
5.6 Conclusion 102

6 General conclusion and future work 104
Future works 105

Appendix A 108
References 111
List of Figures 116
List of Tables 122

1 Préambule

1.1 Résumé de la thèse en Français

ETUDE DU DELAMINAGE ET DE LA RESISTANCE DES INTERFACES DANS LES CIRCUITS IMPRIMES

1.1.1 Introduction

Cette thèse s'intéresse aux circuits imprimés (PCB) multicouche constitués alternativement de matériaux diélectriques et de cuivre. Pour des applications aérospatiales, satellites par exemple, la fiabilité de ces PCB doit être garantie pendant des décennies pour assurer le fonctionnement des dispositifs électroniques (maintenance difficilement envisageable). Les phases de qualification de ces PCB sont alors sévères. En effet, les PCB doivent résister entre autres à un nombre de cycles prédéfinis suivant les applications dans la plage [-55 ° C, + 125 ° C] selon la norme IPC 2.4.8.2. Un des points primordiaux à vérifier est que le cuivre ne présente pas de rupture et que les interfaces restent sûres.

De nombreuses recherches sont consacrées à l'amélioration des propriétés interfaciales, Venables [1], Mathieson and Bradley [2]**.** Dans ce travail, nous nous concentrons plus particulièrement sur la résistance de l'interface entre un composite tissé (fibres de verre et résine époxy) et un film mince de cuivre. Pour cela nous allons mettre en place et exploiter des résultats expérimentaux issus du test de pelage. Ce test mécanique se caractérise par la mesure de la force d'adhésion. En général, l'adhérence entre le métal et le polymère est assez faible, de sorte que pour les applications industrielles, la fiabilité des assemblages reste problématique. L'étude fondatrice pour la modélisation du test de pelage est celle réalisée par Rivlin [3] en 1944, où une relation simple a été établie, dans le contexte d'un film inextensible, entre l'énergie de décohésion et la force de pelage. La première analyse théorique du test de pelage est présentée par Spies [4], qui a examiné le pelage à 90° d'un film mince. Concernant le problème des films minces élastiques sur un substrat rigide, le modèle classique de Kendall [5] montre

que la force de pelage dépend non seulement de l'énergie d'adhésion mais également de la déformation élastique du film et de l'angle de pelage. Pour la problématique de ce présent travail, nous sommes dans le cas où la plasticité est activée lors du pelage. De nombreux travaux de la littérature étudient ce cas. On peut citer, sans être exhaustif, l'analyse théorique du pelage d'un film mince élasto-plastique collé sur un substrat élastique développée par Kim et Aravas [6]. Dans le cas de la flexion pure d'un matériau élasto-plastique en déformation plane, ils ont défini une relation moment/courbure à partir de la théorie de poutres élasto-plastiques. Ils ont également présenté une analyse du pelage en régime stationnaire et une méthode de calcul de la dissipation plastique. De plus en faisant un bilan énergétique, ils ont relié la force de pelage mesurée expérimentalement à l'énergie de décohésion. Wei et Hutchinson [7] ont quant à eux simulé en régime stationnaire le processus de pelage de couches minces en utilisant la méthode des éléments finis (le film étant considéré comme un matériau élasto-plastique).

1.1.2 Essais expérimentaux : pelage et traction

Afin de déterminer la résistance de l'interface entre le film mince de cuivre et le substrat composite, un dispositif de pelage expérimental a été acheté au début de la thèse. A l'aide d'une machine MTS équipée d'une table coulissante, on effectue des tests de pelage à différents angles allant de 0° à 180°. Le déplacement maximum de la machine MTS est de 1000 mm et sa vitesse maximale est de 50 mm/s. La capacité du capteur de force utilisée pour les tests de pelage est de 50 N. Au cours des essais, les vitesses de la traverse et de la table sont identiques (0.5 mm/s) car la traverse et la table sont reliées par un câble (Fig.1.1(a)). Ainsi l'angle de pelage est constant pendant l'essai.

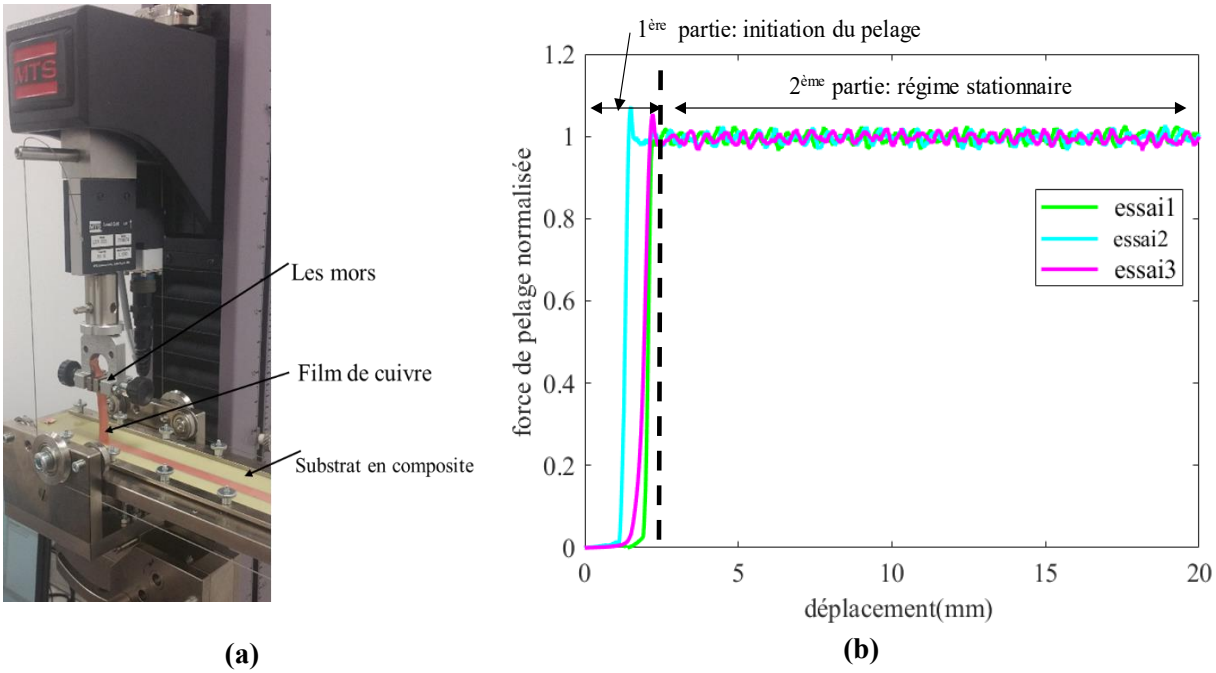

(a) **(b)**

Figure 1.1: (a) Dispositif utilisé dans les tests de pelage **(b)** Courbe force-déplacement obtenue suite au test de pelage, mettant en évidence deux phases : initiation et régime stationnaire.

Des échantillons représentatifs sont réalisés à partir des matériaux utilisés dans les applications réelles. Ainsi des pré-imprégnés de fibres de verre-époxy et un feuillard de cuivre ont été assemblés conformément à l'usage industriel. Le pressage à chaud des matériaux assure l'adhésion du cuivre. Des bandes de cuivre (10 mm de largeur, 30 cm de long et 35µm ou 70µm d'épaisseur) sont ensuite gravées à la surface de l'échantillon avant essai. L'expérience est menée à température ambiante. Nous avons réalisé des tests de pelage pour cinq angles de pelage différents (45°, 60°, 90°, 120° et 135°). Les tests de pelage ont été répétés plusieurs fois pour chaque angle de pelage. A l'aide du capteur de force du dispositif expérimental, on enregistre l'évolution de la force de pelage en fonction du déplacement de la traverse. Fig. 1.1(b) présente la réponse force-déplacement pour un essai à 90°. On peut observer deux parties : une première phase où le film se met en place suivie d'une deuxième où on atteint le régime stationnaire : force constante tout au long du pelage. C'est cette phase stationnaire qui est retenue pour cette étude.

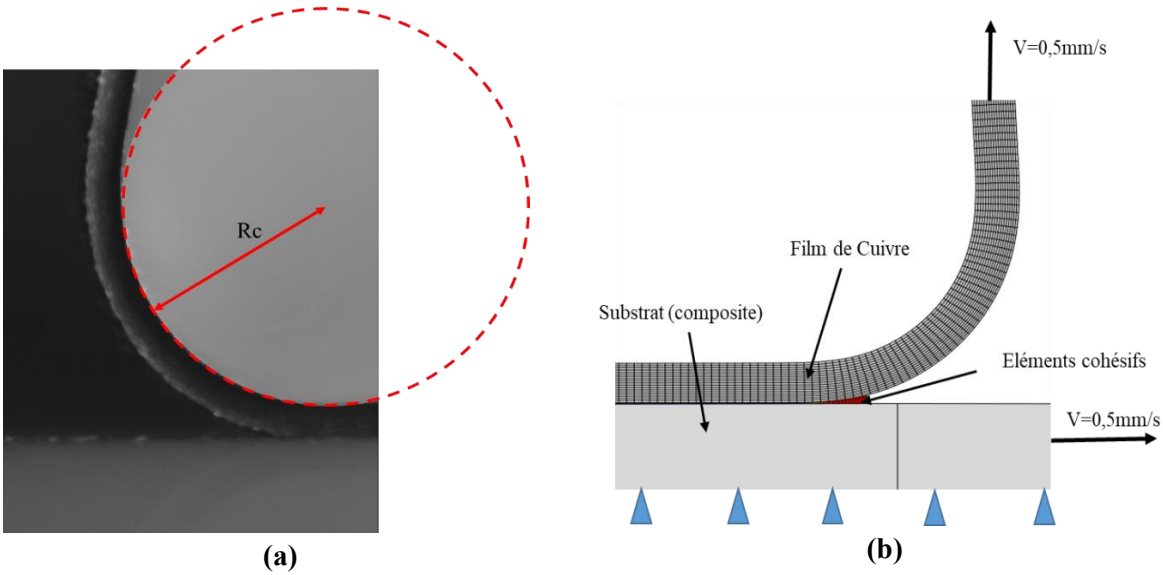

Figure 1.2: (a) Visualisation de la zone de décohésion avec mesure du rayon de courbure. **(b)** Modèle Eléments Finis développé pour la simulation du test de pelage.

Pour déterminer expérimentalement l'énergie de décohésion entre le cuivre et le substrat (composite), la connaissance du rayon de courbure du film de cuivre en régime stationnaire est très importante. Ainsi, le rayon de courbure du film de cuivre pour chaque angle de pelage est mesuré à l'aide d'une caméra haute résolution équipée d'un objectif macroscopique. Des images de la courbure sont prises et enregistrées automatiquement lors de l'essai de pelage. La Fig. 1.2 (a) montre la zone de décohésion avec ajustement d'un cercle à la racine du film, lors d'un essai à 90°. La même technique est appliquée aux autres angles de pelage. Le rayon de courbure du film est alors déterminé.

Des essais de traction sont aussi réalisés sur des feuillards de cuivre (35µm et 70µm d'épaisseur) ayant subi le même cycle thermique que lors de la fabrication des éprouvettes de pelage. A partir de ces essais de traction, nous avons mis en évidence le comportement élasto-plastique du cuivre que nous allons utiliser dans la partie analytique et dans la partie modélisation numérique. Tous les résultats issus de la thèse sont présentés dans le chapitre 3.

1.1.3 Théorie sur le pelage

Dans cette étude, nous considérons que la plasticité du cuivre joue un rôle fondamental dans le processus de pelage. Comme dans la littérature, nous réalisons un bilan énergétique permettant de relier le travail des forces extérieures dW_{ext} à l'énergie d'interface dU_s, à l'énergie élastique stockée dans le film soumis à la force de pelage dU_{el} (due à la traction) et à l'énergie dissipée plastiquement lors du pelage dU_p :

$$dW_{ext} = dU_{el} + dU_s + dU_p \tag{1.1}$$

avec :

$$dW_{ext} = F(1 - \cos\theta)\Delta l \tag{1.2}$$

$$dU_{el} = \frac{F^2}{2Ebh}\Delta l \tag{1.3}$$

$$dU_s = b\Gamma\Delta l \tag{1.4}$$

Δl correspond à l'avancée de la décohésion. b, h, E, Γ et θ sont respectivement la largeur, l'épaisseur, le module d'Young du cuivre, l'énergie de décohésion et l'angle de pelage. Plus exactement, dU_p est le travail dû à la flexion plastique du film lors de la décohésion. Dans la suite, on appellera également ce terme, dissipation plastique même si ce terme contient une partie d'énergie stockée lors de la phase de pelage (flexion et flexion inverse). Dans toute cette campagne d'expérimentation, on considère une largeur b=10 mm et on teste deux épaisseurs : h=35µm ou 70µm. L'énergie élastique dans le film mince soumis à la force de pelage étant très faible voir nulle dans le cas où le film est inextensible, l'équation (1.1) peut s'écrire :

$$(1 - \cos\theta)F\Delta l = \Gamma b\Delta l + dU_p \tag{1.5}$$

En divisant par l'aire $b\Delta l$, on aboutit à la relation proposée dans Aravas et al. [8] définissant l'énergie de décohésion

$$\Gamma = (1 - \cos\theta)\frac{F}{b} - \varphi \tag{1.6}$$

où

$$\varphi = \frac{1}{b}.\frac{dU_p}{dl} \tag{1.7}$$

Dans la suite, on note $P = \frac{F}{b}$, la force de pelage par unité de largeur. Pour un matériau parfaitement plastique (voir Aravas et al [8]), l'énergie dissipée plastiquement vaut :

$$\varphi = \frac{3P}{\eta}(2k_B - 5 + \frac{10}{3k_B}) \tag{1.8}$$

avec

$$\eta = \frac{6EP}{h\sigma_0^2} \tag{1.9}$$

$$K_e = \frac{\sqrt{3}\sigma_0}{Eh} \tag{1.10}$$

$$k_B = \frac{K_B}{K_e} \tag{1.11}$$

où η représente la force de pelage adimensionnelle et K_e, la courbure limite pour laquelle le film reste entièrement élastique. La courbure du film $K_B = \frac{1}{R_C}$ est issue de la mesure expérimentale (voir Fig. 1.2 (a)). k_B est la courbure adimensionnelle et σ_0 la limite d'élasticité du film de cuivre. On voit bien que la dissipation plastique dépend du rayon de courbure mesuré et du comportement du film de cuivre. L'énergie de décohésion Γ depend de la force de pelage mesurée et de la dissipation plastique.

Nous avons développé dans cette thèse une expression de la dissipation plastique prenant en compte le comportement élasto-plastique du cuivre, voir chapitre 4. Cela va nous permettre de déterminer l'énergie de décohésion utile pour la simulation numérique.

1.1.4 Modèle Numérique

Pour simuler le test de pelage, un modèle numérique par éléments finis (ABAQUS / standard) en 2D a été développé pour des films de cuivre d'épaisseur 35µm et 70µm. La géométrie et les conditions aux limites du modèle numérique sont illustrées sur la Fig. 1.2 (b). Une étude de convergence au maillage a été conduite. Pour un essai à 90°, un maillage avec 9 et 18 éléments dans l'épaisseur donne des résultats indépendants de celui-ci. L'interface entre le film de cuivre et le substrat (composite) a été modélisée

par des éléments cohésifs avec une loi de traction-séparation, disponible sous ABAQUS. La réponse des éléments cohésifs est régie par l'initiation et la propagation du délaminage. Le critère d'initiation est quadratique comme présenté en Eq. (1.12). Le critère de propagation adopté se met sous la forme d'une loi linéaire Eq. (1.13). Au travers de ces deux lois, un couplage entre le mode normal et le mode tangentiel opère.

$$\left(\frac{\sigma_n}{\sigma_{n,c}}\right)^2 + \left(\frac{\sigma_t}{\sigma_{t,c}}\right)^2 = 1 \tag{1.12}$$

$$\frac{G_n}{\Gamma_I} + \frac{G_t}{\Gamma_{II}} = 1 \tag{1.13}$$

où, Γ_I et Γ_{II} sont les énergies de rupture de l'interface en mode I et mode II. $\sigma_{n,c}$ et $\sigma_{t,c}$ sont les contraintes critiques en traction et en cisaillement. Comme dans la littérature (voir par exemple Martiny et al [9]), on adopte : $\Gamma_I = \Gamma_{II} = \Gamma$ et $\sigma_{n,c} = \sigma_{t,c} = \hat{\sigma}$ dans la simulation**.** Des informations complémentaires sont disponibles au chapitre 4**.**

1.1.5 Résultats et discussion

Les forces de pelage et les rayons de courbure pour les angles 45°, 60°, 90°, 120° et 135° sont mesurés. Au moins trois tests sont réalisés pour chaque angle afin d'obtenir des résultats représentatifs voir Fig. 1.1 (b). On remarque expérimentalement et numériquement dans ce travail que la force de pelage diminue lorsque l'angle de pelage augmente pour les deux épaisseurs de cuivre ($35\mu m$ et $70\mu m$), ce qui est en accord avec des travaux précédents de Williams and Kauzlarich [10], Molinari and Ravichandran [11]. Dans le cas du pelage d'un film mince de cuivre sur un substrat en composite, il est essentiel de tenir compte de la plasticité engendrée lors de la flexion et de la déflexion du film de cuivre pour déterminer les propriétés de l'interface. A partir de la force de pelage et du rayon de courbure déterminés lors d'un essai de pelage à 90°, les paramètres de la loi cohésive sont obtenus. La Fig. 1.3 montre que les forces de pelage simulées par éléments finis concordent bien avec les résultats expérimentaux. De même, les rayons de courbure numériques sont aussi en accord avec ceux expérimentaux, voir Fig. 1.4.

De plus d'après les résultats numériques et expérimentaux, nous vérifions bien que la force de pelage et le rayon de courbure augmente lorsque l'épaisseur du film augmente.

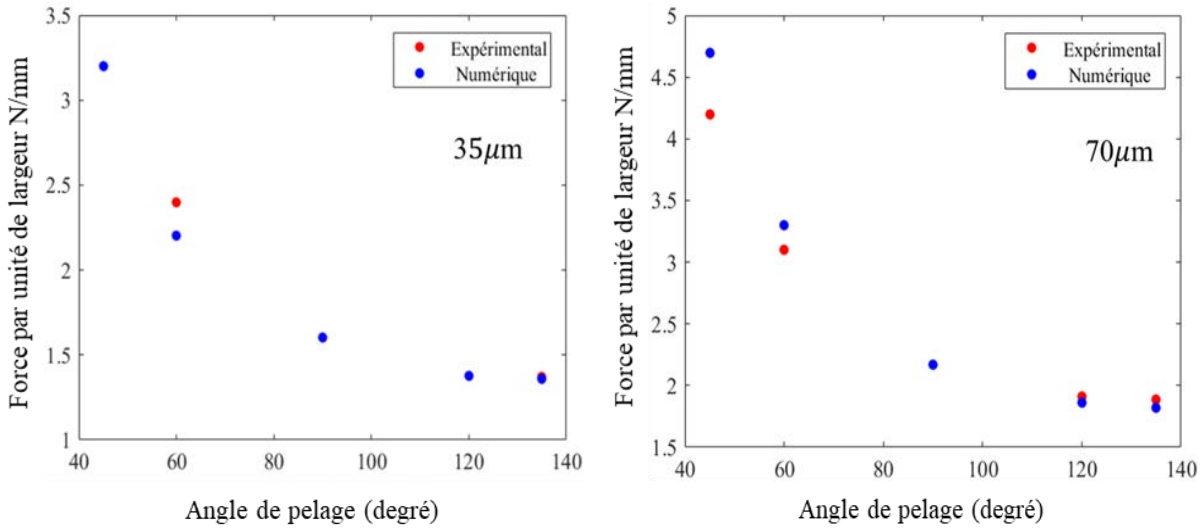

Figure 1.3: Force de pelage par unité de largeur en fonction de l'angle de pelage. Comparaison entre expérience et simulation. Deux épaisseurs de cuivre sont considérées : 35 μm et 70 μm.

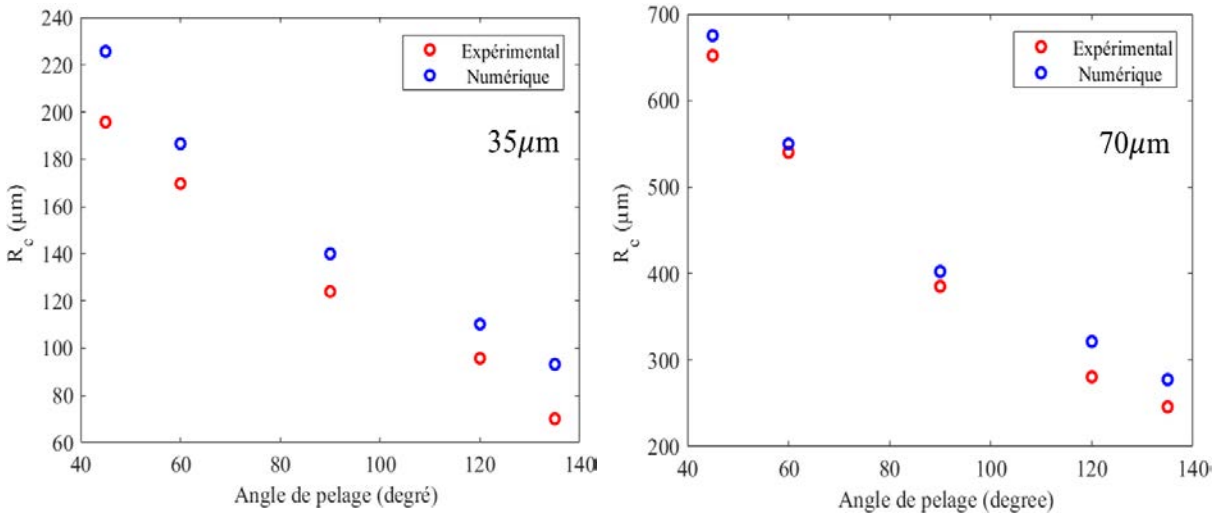

Figure 1.4: Rayon de courbure en fonction de l'angle de pelage pour des films de cuivre d'épaisseur : 35 µm et 70 µm. Comparaison entre expérience et simulation.

1.1.6 Conclusion

Des tests de pelage ont été réalisés pour mesurer les forces de pelage et les rayons de courbure pour différents angles afin de définir les propriétés de l'interface entre le cuivre et le substrat (composite). Un développement analytique basé sur la flexion et la déflexion du film de cuivre lors du pelage nous a permis d'obtenir une expression explicite de la dissipation plastique. Une simulation par éléments finis du processus de pelage a été réalisée**.** Des éléments cohésifs entre le film de cuivre et le substrat (composite) ont été utilisés pour représenter l'interface. On a montré qu'il est possible de reproduire les résultats expérimentaux en termes de force de pelage et de rayon de courbure pour deux épaisseurs du film de cuivre. Nous pouvons ainsi estimer l'énergie de rupture de l'interface. Il est montré que la dissipation plastique joue un rôle prépondérant et que négliger cet effet pourrait conduire à des énergies d'interface bien trop élevées.

1.2 General Introduction

The present work was funded by the European Union ITN Marie Sklodowska Curie action via OUTCOME project untitled: Engineering Structures Subjected to Extreme Loading Conditions. Five partners (University Carlos III of Madrid in Spain, Technion in Israel, Université de Lorraine (UL)), two SME (AEROSERTEC (Spain) and CIMULEC (France)) and two major groups (EADS Space and RAFAEL) are forming the consortium. In detail, my research work is a collaborative work between CIMULEC, manufacturer of Printed Circuit Boards (PCB) for Space and Aeronautics application and UL (LEM3 laboratory). CIMULEC and LEM3 (UL) are partners in a common laboratory called LEMCI. The reliability of PCB has always been an important topic for manufacturers, especially in the aerospace industry. A PCB is a multi-layer, multi-material assembly (see Fig. 1.5 (a)). It allows to interconnect electronic components soldered on the outer layers in order to realize a complex electronic system. A schematic cross section of the PCB is present in Fig. 1.5 (b). The PCB is developed for a very specific goal. Predicting its reliability requires expertise in mechanical and material sciences. The reliability of assemblies (PCB with chip resistors or BGA...) is out of the scope of the thesis even it is known that the failure of the solder layer can be often observed (see for instance Sabbah et al [12]). Coombs [13] in its Printed Circuits Handbook presents printed circuit boards and the manufacturing processes. A PCB is made mostly of woven composite (glass fiber + resin) and copper. For specific applications, the number of copper layers is larger than 10. The thickness of the PCB is around 1mm. As a consequence, the woven composite layers are around 100 µm while the copper layer is quite thin. For PCB application, it is in the range of [17 µm – 70 µm]. To be qualified, the PCB has to face a number of standards (mostly prescribed by the Institute for Printed Circuits (IPC)). The reliability of the PCB is crucial since it provides the electrical connectivity between chips and the device (satellite, aircraft, …).

Two main modes of failure are observed in PCB. Cracks in plated through hole are the major concern of failure (see figure 1.6 (a)). Due to the mismatch in coefficient of thermal expansion between copper and composite, failure by low cycle fatigue is observed during thermal cycles. Depending on the PCB configuration, manufacturers have to ensure that the PCB will be able to sustain a given number of cycles without occurrence of any defects**.** The second type of defect is the possible delamination between

layers (see figure 1.6 (b)), when the PCB will experience very large temperature variation. This may occur when the PCB is equipped by components and the temperature can be as large as 270°C.

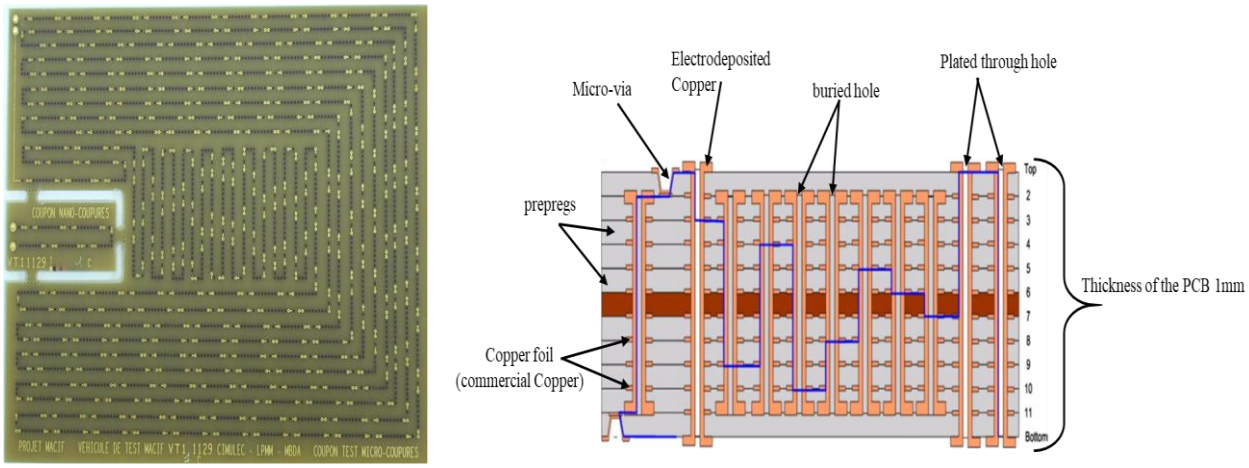

(a) **(b)**

Figure 1.5: Printed circuit boards (PCB): **(a)** View of multilayer printed circuit boards and **(b)** Schematic cross section of the PCB *[14]*.

My PhD work concerns this second type of defect. Two types of copper are present in PCB. The copper path (thin layers in the PCB plane) is usually made of a commercial copper. The different layers are interconnected via plated through holes containing the second type of copper present in PCB (named electrodeposited copper) and produced by the PCB manufacturer. In the present work, I will concentrate only on commercial copper called HTE (High Temperature Elongation) Grade 3.

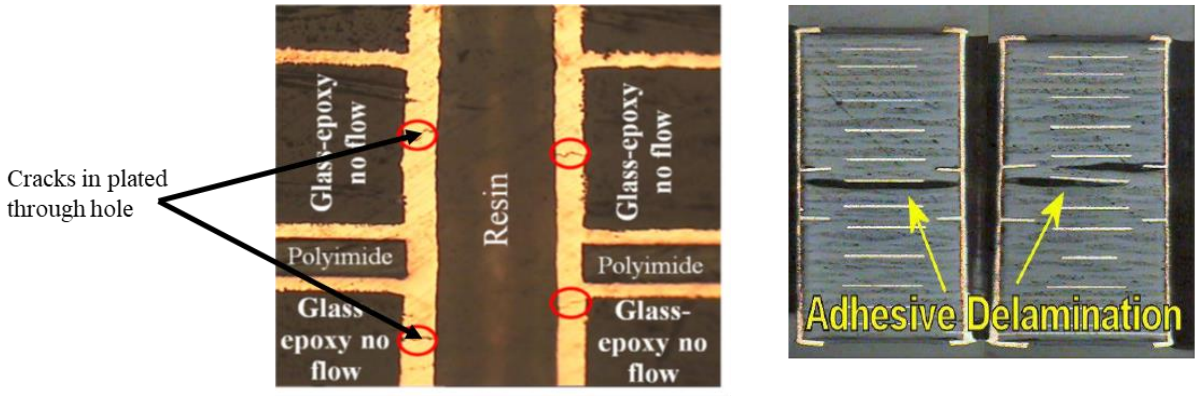

(a) **(b)**

Figure 1.6: Printed circuit boards (PCB): **(a)** Cross sections of a plated through hole after thermal cycling [14]. Some cracks are observed in the electrodeposited copper and **(b)** Delamination between layers in PCB [15].

The producer, via the datasheet, provides some information concerning the interface fracture energy. For that purpose, the manufacturer is carrying out peel tests. But quite often the laminate used by the PCB manufacturer has a different weaving pattern. As a consequence, it is not sure that the provided data is representative of the material configuration adopted in the design of the PCB. In addition, the interface fracture energy is deduced from the peel force without consideration of the plastic dissipation. This may overestimate the interface strength.

The goal of my research work is threefold:

-developing measurements on real materials used by the PCB manufacturer,

-modeling the deformation process of copper film during peel tests,

-analyzing the tests by finite element calculations.

The combination of experiments, modeling, FE calculations will enable to provide estimate for the interface energy between copper and woven composite.

The manuscript is organized as follows. In the second chapter, I will present experimental, numerical and analytical works of the literature on peeling for different types of thin film. In chapter 3, I will describe the experimental methodology and tests performed during my PhD to get reliable data. In the fourth chapter, based on the elastic-plastic response of copper, we have proposed a new expression of the plastic dissipation in the copper film during peeling. Finally, we have conducted finite element calculations of the peel test to validate the modeling proposed to describe the experimental results. The main result of the PhD is the development of a combined strategy (experiment, finite element simulation, analytical modeling) which seems to be efficient for the determination of the interface fracture energy.

2 STATE OF THE ART ON THE MECHANICS OF PEELING

2.1 Introduction

Peel test is a simple mechanical test adopted to determine the properties of the interface when a thin film is deposited on a substrate. Peeling is widely adopted in many technological applications. At the industrial level, the peel test is used to compare strength of the interface. Many experimental efforts, analytical expressions and numerical models have been devoted to analyze the peel test in the literature. Peeling may be carried out by applying a constant force but usually the film is strained at constant velocity, see Kovalchick, Molinari and Ravichandran [16]. As a consequence, the resulting force to separate the interface is measured, called the peel force. It must be linked to the interface fracture energy. The magnitude of the resulting peel force depends on variables such as the peel angle, the temperature, the peel arm thickness and the substrate. The first analysis of peel test was investigated by Rivlin [3] in 1944, where the peeled film was considered as inextensible. A relationship between the interface fracture energy and the peel force was established. The peel test was after that adopted by aerospace companies as a method of quality control of bonded aircraft components, Spies [4]. Kendall [5] extended Rivlin's approach by taking into account the elastic strain energy, but restricted the analysis to small deformation. In the case of my PhD, the plasticity of copper plays a significant role in peeling so a large attention will be devoted to this aspect in the theoretical part of this chapter.

Finding the interface fracture energy is an important issue for many industrial applications, more specifically when multi-layered materials are adopted to combine different properties of each medium. Delamination is an issue since the early seventies and the introduction of laminated composites in structures. To experimentally determine the interface properties, a large literature has been proposed. One of the most popular set-up is the double-cantilever beam (DCB). DCB was already present in the literature at the end of the fifthies. Indeed Benbow and Roesler [17] developed a device where a flat strip is split in two parts via a wedge driven by a screw. One of the pioneering work on the measurement

of the interface strength is the work of Obreimoff [18] on Mica. Because of the wide production of composite materials, the interface properties between layers can be measured by DCB test according to ASTM- D 5525-94 a) standard. For the PCB industry, the critical interface is located between the woven composite and copper path. A different test is classically adopted: the peel test. As the peel test is adopted in my PhD, next I will focus only on the description of the peel test. In the following of this section, I will present experiments. Then I will also decribe analytical models developed in the literature. Finally, I will also present how numerical simulations have been used in the literature.

2.2 Peel test

Experimental peel tests are developed to provide information on the adhesion energy. In Kim and Kim [19], the peel test is carried out with a standard machine whereas Peng et al [20] proposed in Fig. 2.1 (a), a peel-rig in order to vary the peel angle conveniently for characterizing the adhesive properties between an adhesive tape and a glass substrate materials. The peel force is measured with a load cell, see Fig. 2.1(a). On the Fig. 2.1(b), the load-displacement curve is presented. We can observe that there are two stages during peeling: the first stage corresponds to the initiation of peeling. In the second stage the peel force reaches a stable value. Fig. 2.1(c) shows that the peel force at steady state decreases when the peel angle increases, see Molinari and Ravichandran [11]. The peel force during the stationary part of the test is usually the main information which is always provided in experiments. Some studies have tried to capture additional information by observing the process zone. In Kovalchick et al [21], a fibrillation zone is present at the contact point between the elastic adhesive film and a rigid substrate, (see Fig. 2.2(a)). In the case of peeling of copper film bonded on a rigid substrate, the process zone behaves differently, with a small radius of curvature, see Fig. 2.2(b). In Zhao and Wei [22] the film thickness is less than 10 μm.

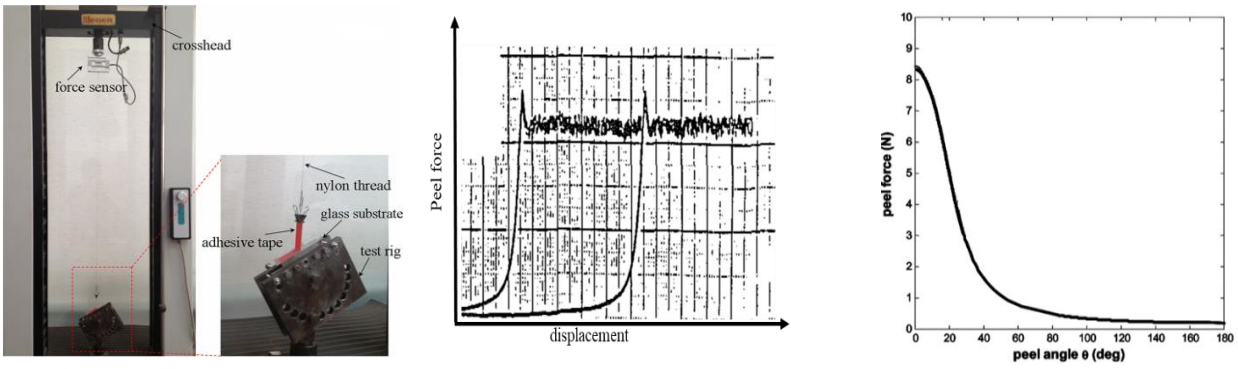

(a) **(b)** **(c)**

Figure 2.1: Peel test: **(a)** A standard peeling machine with a dedicated rig to tune the peel angle [20], **(b)** Load-displacement curve obtained during peeling [19], **(c)** Peel force as a function of the peel angle [11].

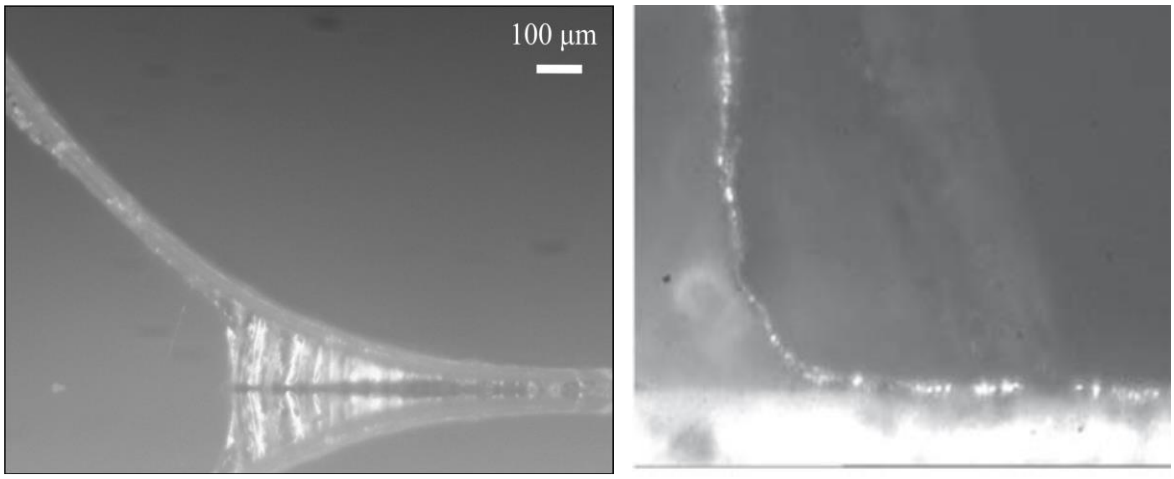

(a) **(b)**

Figure 2.2: **(a)** Process zone for an elastic adhesive bonded on a rigid substrate for a peel test at 70° *[21]*. The film thickness is 50 μm **(b)** Process zone of copper film bonded on a rigid substrate. The film thickness is less than 10 μm *[22]*.

Kovalchick, Molinari, Ravichandran [16] have developed an experimental configuration to investigate the stability of the peeling process for elastic tapes. Different angles were tested. They benefit from the work of Kovalchick [23] where using digital camera, the position of the film in the vicinity of the crack tip was recorded, see Fig. 2.3(a). The shape of the film in the process zone was modeled by adopting an elliptical profile, see Fig. 2.3(b).

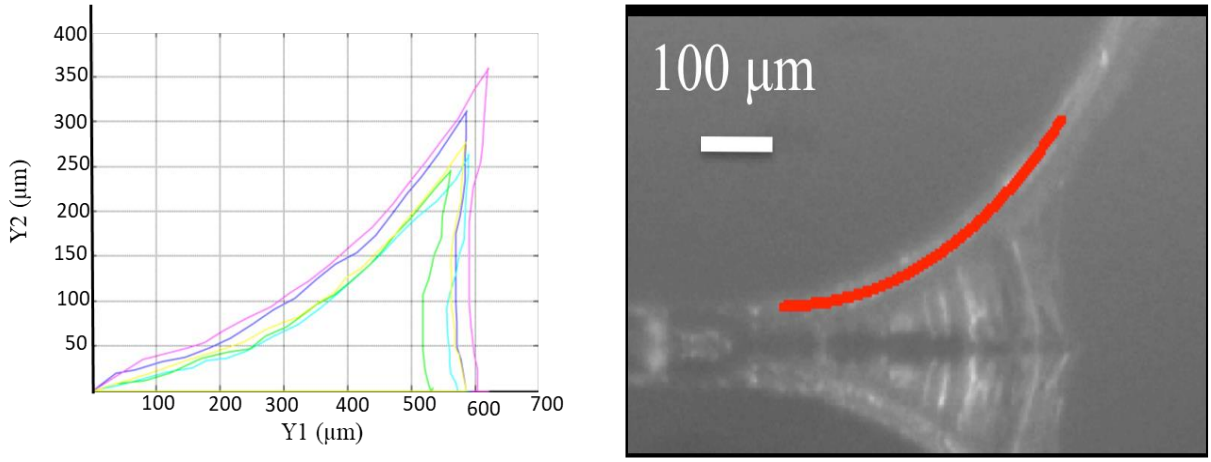

(a) **(b)**

Figure 2.3: **(a)** Process zone shape at five separate time increments during the steady state regime. The peel angle is 90° *[23]* , **(b)** Image of the process zone for a 90° peel test where an elliptical profile (red line) is fitted to reproduce the shape of the tape backing *[23]*.

Peng et al [20] has studied peeling of viscoelastic polyvinylchloride (PVC) thin-film on a rigid substrate (glass). Afferante and Carbone [24] presented some examples of peeling of an elastic film on different substrates. In Fig. 2.4(a), a tape is bonded on a human skin (viscoelastic substrate). In Fig. 2.4(b) the same tape is bonded on a rigid substrate.

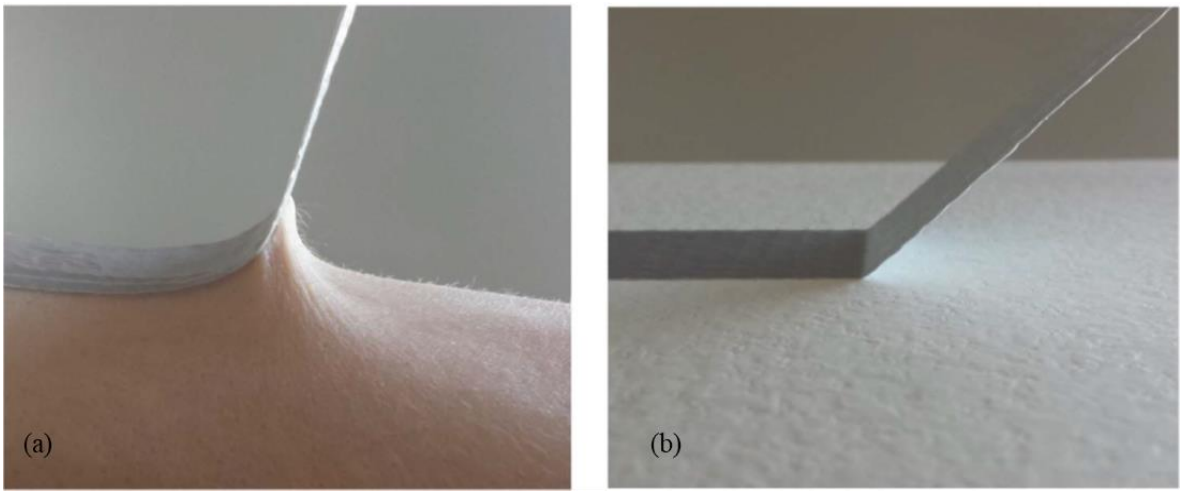

Figure 2.4: Different peeling behaviors of a tape on human skin **(a)** and on rigid substrate **(b)** *[24]*

Wei and Zhao [25] developed an experimental peel device for testing the adhesion of ductile thin films on ceramic substrates.

Many researchers focus also on the film curvature. Kawashita, Moore and Williams [26] developed an experimental method based on high resolution digital camera. With macro lenses, they produced pictures of the specimen during the peeling process. With a dedicated software, they computed automatically the local curvature. Fig. 2.5 illustrates the methodology for this calculation. The radius of curvature R of the central surface is deduced from the radius of the upper surface by adding the peel arm half thickness (h/2), where (h) is the thickness of the film. Zhao and Wei [22] have performed peel tests to estimate the interface toughness and the separation strength between copper thin film and Al_2O_3 substrate. Zhao and Wei [22] have also used a Questar measuring microscope with long focus to take micrographs of the film curvature, see Fig. 2.2(b). They have determined the curvature R of the film at the crack tip using multiple point approximation. They showed that the radius is kept constant when the peel force reaches a stable value during the peeling. This observation is valid when the film thickness is larger than 10 µm. For a film thickness of 3µm, the peel force reaches a stabilized value but with some fluctuations which corresponds to cyclic folding and unfolding process. Thus, the curvature of the film is not available. Note that for submicron thin films, the peel test is not used and other test methods like the scratch test have been proposed in the literature, see for instance Covarel et al [27] and Boddaert et al [28].

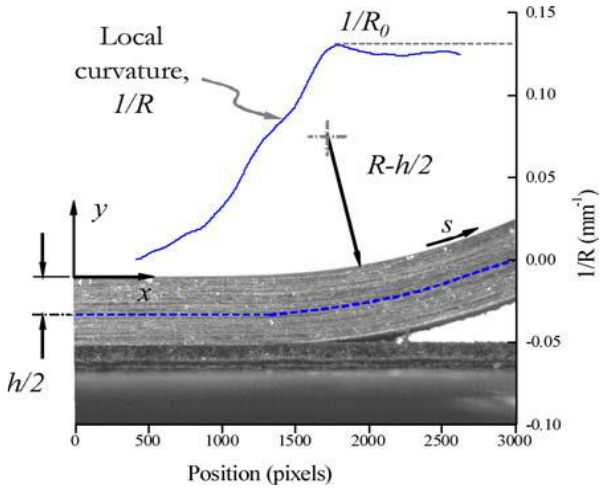

Figure 2.5: Illustration of curvature measurement using digital photography *[26]*.

Song and Yu [29] investigated T-peel test, as shown in Fig. 2.6(a). They considered polyimide-metal specimens. During the test, they took micrographs of the process zone during T-peel tests as shown in Fig. 2.6(b). From this figure, they measured the curvature of the metal and the polymeric films at the peel front by fitting circles. So from experimental tests, one can mention that it is possible to measure the peel force under steady state. In addition, the geometrical configuration of the process-zone can be clearly captured by digital camera. These information will be necessary to provide consistent estimate of the interface fracture energy when plasticity is developing in the film.

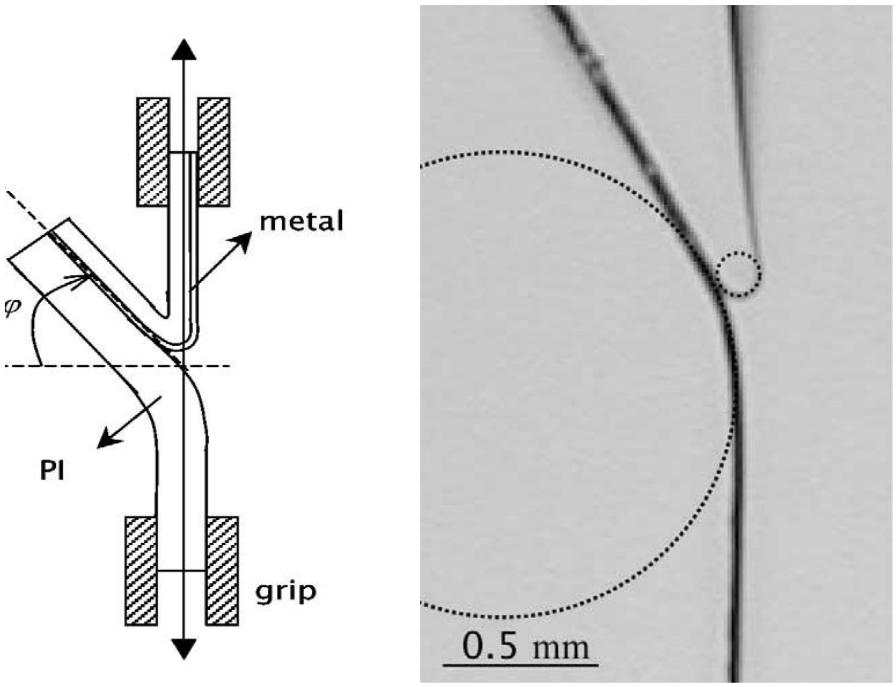

(a) **(b)**

Figure 2.6: **(a)** Schematic presentation of T-peel test *[29]*, **(b)** A micrograph illustrates the configuration during steady state. The curvatures are measured by considering that circles present the best fit *[29]*.

2.3 Modeling of the peel test based on energy consideration

The most significant study of peel test is that of Rivlin [3] in 1944, where a simple relation was derived in the context of an inextensible film on a rigid substrate. He proposed a simple link between interface fracture energy in the peeling process and the peel force, see Eq. (2.1).

$$\Gamma = \frac{F}{b}(1 - \cos\theta) \tag{2.1}$$

where F is the peel force, Γ is the interface fracture energy per unit area, b is the width of the film and θ is the peel angle.

The formula (2.1) is derived as follows, see Fig. 2.7(a). Consider the energy balance during the peeling of the film from position B to B'. The distance BB' is Δl. As the film is inextensible and the substrate rigid, we have only two contributions: the surface energy dU_s for the creation of new surfaces and the work done by the force F, dW_{ext}. From energy consideration, the input of external work is absorbed to separate the interface:

$$dW_{ext}=dU_s \tag{2.2}$$

The amount of energy required to peel the film on a distance $\Delta \boldsymbol{l}$ is:

$$dU_s = \Gamma b \Delta l \tag{2.3}$$

The external work dW_{ext} of the peel force is:

$$\vec{F}.\overrightarrow{AA'} = F(1 - \cos\theta)\Delta l \tag{2.4}$$

From relationship (2.2), Eq. (2.1) is obtained**.** The Rivlin model is based on an energy balance, so it does not provide any information, such as stress or displacements, near the crack tip. The corresponding evolution of the peel force F versus the peel angle θ is shown on Fig. 2.7(b). For peel angle larger than 90°, the peel force is varying slowly while for small peel angle, the peel force increases strongly. One

of the restriction of Eq. (2.1) is that the peel force tends to infinity as θ tends to zero. Therefore, the effect of the elasticity should be important for such configuration.

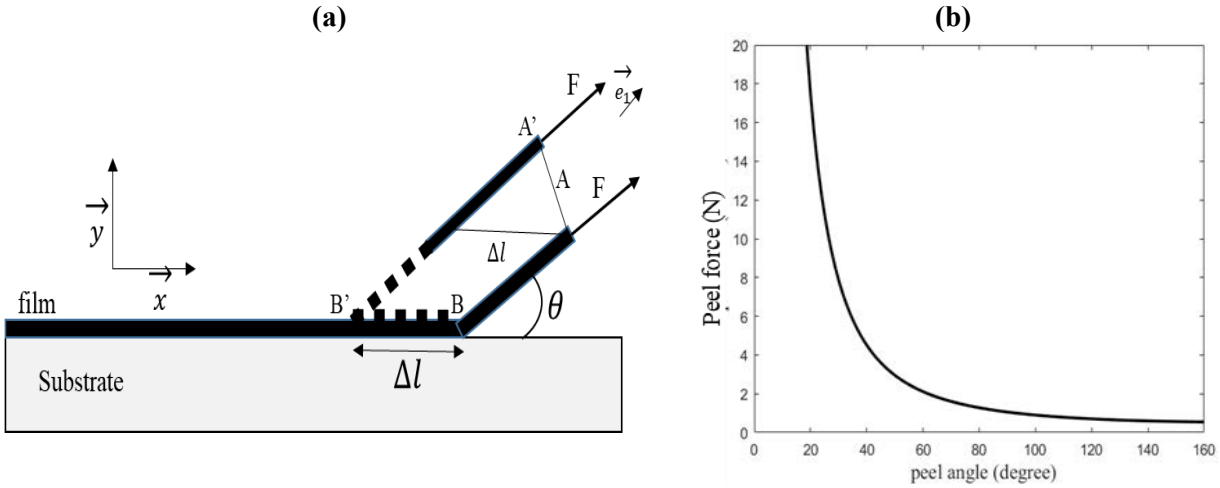

Figure 2.7: (a) Peeling of an inextensible film on a rigid substrate. The thickness of the film is **h** and the width is **b**. **(b)** Peel force as a function of peel angle for an inextensible film. Material and geometrical parameters are listed in Table 2.1.

Kendall [5] investigated the peel test for elastic film. He provided simple analytical relations to describe the different phenomena that govern the peel test. Consider that the film is elastic, with Young's modulus E. The substrate is still rigid. In that case, the energy balance must account for an elastic contribution term. For the energy conservation during the peeling of an elastic thin film, three contributions are present: a surface energy term dU_s for the creation of new surfaces, the external work done by the peel force dW_{ext} and an elastic energy term dU_{el} due to the extension of the film under the applied force. The last term has been evaluated by Kendall [5]**:**

$$dU_{el} = \frac{F^2}{2Ebh}\Delta l \tag{2.5}$$

The expression of dW_{ext} is different from Eq. (2.4) since the film is elastic. Taking into account that the increase of the length of the free arm is $\Delta l(1 + \frac{F}{Ebh})$, one obtains for dW_{ext}

$$dW_{ext} = F(1 - \cos\theta)\Delta l + \frac{F^2}{Ebh}\Delta l \tag{2.6}$$

Note that the kinetic energy is neglected when compared to other contributions since the peeling velocity is always small (around V=0.5mm/s).

From the energy balance:

$$dW_{ext} = dU_{el} + dU_s \tag{2.7}$$

and combining Eqs (2.3), (2.5), (2.6) and (2.7) we obtained the relation between the peel force F and the interface fracture energy Γ for an elastic film:

$$\Gamma = \frac{F}{b}(1 - \cos\theta) + \frac{F^2}{2b^2Eh} \tag{2.8}$$

Equation (2.8), quadratic in $\frac{F}{b} = P$, shows how the three energy terms (elastic, external work and surface energy) interact. An explicit expression for the peel force by unit film width can be expressed in term of the interface fracture energy, Young's Modulus, peel angle and geometrical features. Note that when the Young' s modulus E is large compared to $F/_{bh}$, the stored elastic energy contribution is negligible. In that case, the expression (2.1) of Rivlin is retrieved. The elastic energy may play a signifiant role for the evaluation of the peel force when the peel angle tends to zero. Fig. 2.8 shows that, in the case of peeling of an elastic film, the peel force decreases also when the peel angle increases, see Molinari and Ravichandran [11]. For large peel angle, Eq. (2.1) and Eq. (2.8) coincide almost. For the Rivlin model, the peel force tends to infinity when θ tends to zero. With the elastic contribution, the peel force has a finite limit. Indeed from Eq. (2.8) when θ=0: $F(\theta = 0) = b\sqrt{2Eh\Gamma}$.

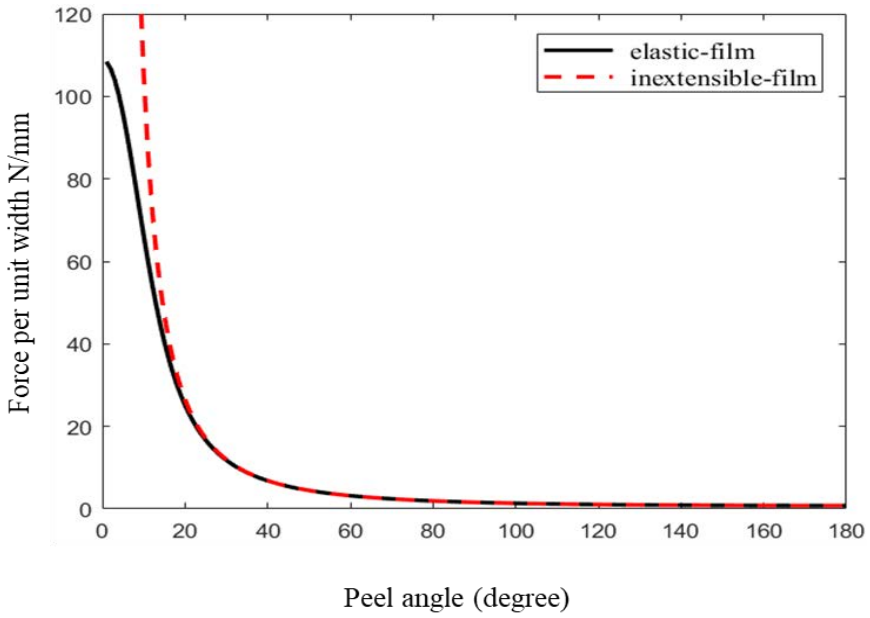

Figure 2.8: Peel force versus peel angle: comparison between elastic and inextensible film. Material and geometrical parameters are listed in Table 2.1. Comparison between the Rivlin and Kendall models.

In some circumstances, the film may be pre-tensioned with an initial pre strain, $\varepsilon_1 = \frac{F_1}{Ebh} > 0$, see Fig. 2.9. In that case, the elastic energy stored in the bonded film (length $\Delta \boldsymbol{l}$) is given by:

$$dU_E = \frac{{F_1}^2}{2Ebh}\Delta l \tag{2.9}$$

The influence of the film pre-strain during peeling was analyzed by Williams and Kauzlarich [30]. When the pre-strain is taken into account in the energy balance for an elastic film, we have a new relation between the peel force F and the peel angle:

$$dW_{ext} + dU_E = dU_{el} + dU_s \tag{2.10}$$

Where

$$dW_{ext} = F(1-\cos\theta)\Delta l + \frac{F(F-\mathrm{F_1})}{Ebh}\Delta l \tag{2.11}$$

Combining Eqs (2.9), (2.10), (2.11), the interface fracture energy Γ is given by:

$$\Gamma = \frac{F}{b}(1-\cos\theta) + \frac{(F-F_1)^2}{2b^2Eh} \tag{2.12}$$

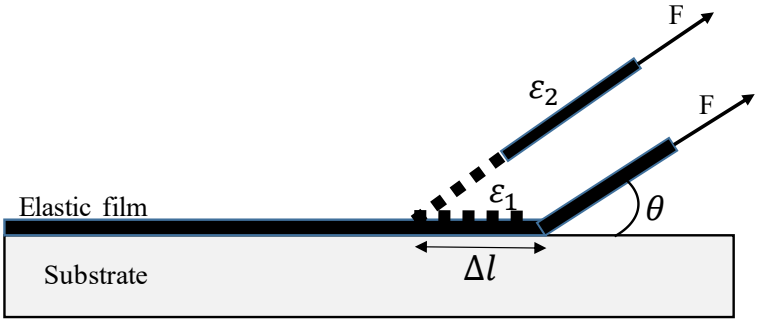

Figure 2.9: Elastic film bonded on the rigid substrate, with an initial pre-strain ε_1. The strain ε_2 is due to the presence of peel force **F**. ($\boldsymbol{\varepsilon_2 = F/Ebh}$)

Fig. 2.10 presents the effect of the pre-strain on the peel force for an elastic film material. The geometrical parameters are shown in Table 2.1. For large values of the peel angle, it appears that the peel force slightly decreases with a pre-strain of $\varepsilon_1 = 0.01$. On the contrary the effect on the peel force is large for small values of the peel angle. Note that when deformation becomes large, a small strain theory is no more valid. Therefore, Molinari and Ravichandran [11] have extended the previous work by proposing a large strain formalism.

b (mm)	10
h (mm)	0.035
E(GPa)	106
Γ(N/mm)	1.6

Table 2.1: Material and geometrical parameters of the film

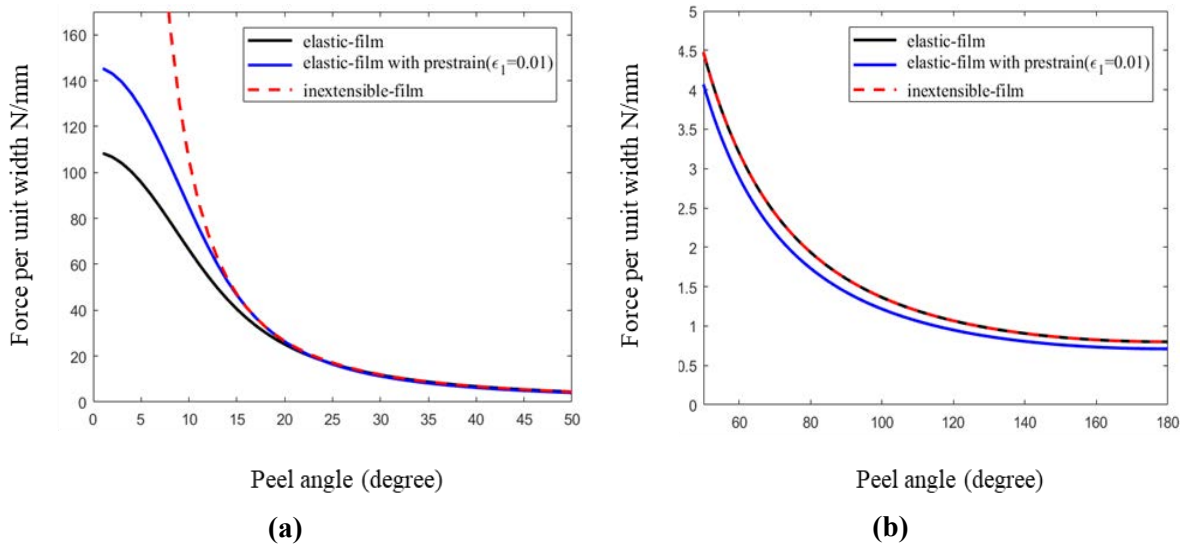

Figure 2.10: **(a)**: Effect of the pre-strain ε_1 on the peeling force, for small peel angle [11] and **(b)**: Effect of the pre-strain ε_1 on the peeling force, for large peel angle [11]. Parameters are provided in Table 2.1

In the previous works, the material is considered as elastic so no dissipation inherited from the material behavior exists. When dissipation in the film during peeling occurs, the energy balance is modified:

$$dW_{ext} + dU_E = dU_{el} + dU_s + dU_{dis} \tag{2.13}$$

Some authors have considered that the film or the substrate may be visco-elastic (this is clear for instance when polymeric films are considered).

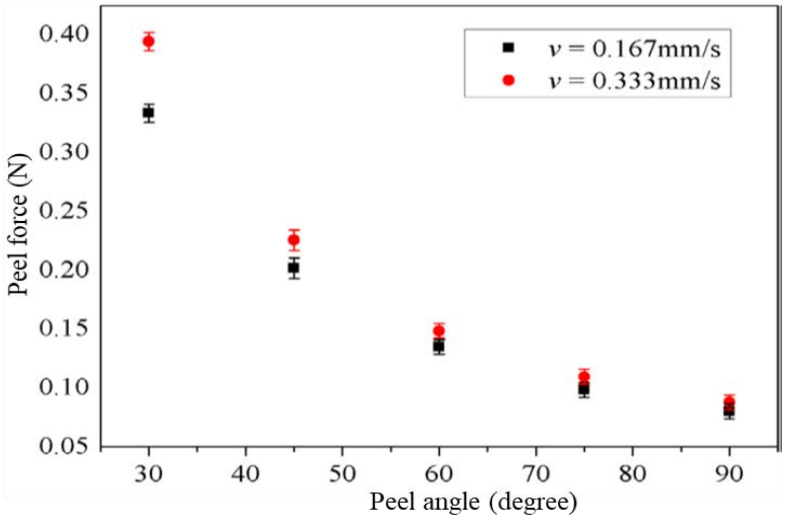

Figure 2.11: Peel force as a function of the peel angle for a visco-elastic film bonded on a rigid substrate *[20]*.

Peeling of a viscoelastic thin-film bonded on a rigid substrate with a viscoelastic interlayer was experimentally considered by Peng et al [20]. They found that the peeling velocity, peeling angle, film thickness and surface roughness have significant influences on the interface fracture energy. It is observed in Fig. 2.11 that the peel force still decreases with the increase of the peel angle for a fixed peel velocity as in the case of an elastic film, see Peng et al [20]. Nevertheless, as the velocity increases, the dissipation is enlarged, so is the peel force. The increase of the force is mostly observed for small peel angle. The viscoelastic effect of a polymeric film was investigated by Loukis and Aravas [31], in which the thin-film was modeled as a cantilever beam subjected to pure bending. Based on the work of Loukis and Aravas [31], Chen et al. [32] further analyzed the peeling problem theoretically for a visco-elastic film considering both the tensile (due to the force) and bending effects. The peeling of an elastic thin tape from a flat smooth viscoelastic substrate was investigated by Afferrante and Carbone [24]. Adhesion mechanism of a viscoelastic material on a substrate has been widely investigated theoretically, numerically and experimentally by many researchers (Kaelble [33], Andrews and Kinloch [34]). Kim and Aravas [6], in their study, analyzed the deformation of a viscoelastic film bonded on a rigid substrate.

For metallic film like copper, plasticity plays an important role so plastic dissipation during peeling needs to be evaluated. Plastic dissipation is taking place near the crack tip as well as during bending which is often considered as the predominant mode of deformation. In that case, the determination of the sole experimental peel force is not sufficient for evaluation of the interface fracture energy. One needs to be able to calculate the plastic dissipation during peeling. Elastic-plastic finite element analysis of the peel test, however, shows that the effects of the crack tip singularities are limited to a small region near the crack tip and that bending is the predominant mode of deformation of the film, for low to moderate cohesive strength, see Kim and Aravas [6].

Effects of plasticity were first considered by Chen and Flavin [35]. They assumed that when the film deformed plastically is unloaded, it forms a circular arc of constant curvature. An approximate analysis of elastic-plastic peeling was presented later by Gent and Hamed [36]. A numerical solution of the elastoplastic peel problem was analyzed by Crocombe and Adams [37] who used the finite element

method to calculate the stress distribution ahead of the interfacial crack. A very approximate method for the calculation of plastic dissipation was presented by Chang et al [38] who considered the energy balance of end loaded cantilever beams. During steady-state peeling, as mentioned in Kim and Aravas [6], Wei and Hutchinson [7], any material point will be subjected to a dominant bending/ reverse plastic bending. The different loading conditions in the vicinity of the crack tip are presented in Fig. 2.12(a). Under the action of an external force per unit width ($P = \frac{F}{b}$) the thin film undergoes mainly bending and reverse elastic bending. In Fig. 2.12(b), IA, AB, BD and DE are referring to the elastic bending, elastic–plastic bending, unloading and to the reverse plastic bending, see Kim and Aravas [6], Wei and Hutchinson [7]. Many contributions have tried to analyze the consequence of the deformation stages highlighted in Fig. 2.12(a). An important contribution was proposed by Kim and Aravas [6]. From the moment curvature relation, see Fig. 2.12(b) for the peel arm (assuming pure bending under plane strain), the plastic dissipation (or more precisely work expenditure or work done by bending plasticity) is obtained. In the following we will adopt the term plastic dissipation. Based on their work, the knowledge of the peel force and the slope of the film at the tip of the process zone was needed to predict the interface fracture energy. They investigated the case of materials presenting hardening (power law expression for the flow stress). Kim et al. [39], Aravas et al. [8] considered next that the material is elastic-perfectly plastic. With that behavior, an explicit moment curvature relation during the bending and the reverse bending was obtained. A closed form expression for the plastic dissipation (or work expenditure) was in addition proposed:

$$\varphi = \frac{3P}{\eta}\left(2k_B - 5 + \frac{10}{3k_B}\right) \tag{2.14}$$

With

$$\eta = \frac{6EP}{h\sigma_0^2} \tag{2.15}$$

$$k_B = \frac{K_B}{K_e} \tag{2.16}$$

$$K_e = \frac{\sqrt{3}\sigma_0}{Eh} \tag{2.17}$$

$$K_B = \frac{1}{R} \tag{2.18}$$

σ_0 is the yield stress, E the Young's Modulus, P the peel force per unit width, K_B the maximum curvature and K_e the elastic limit curvature**.**

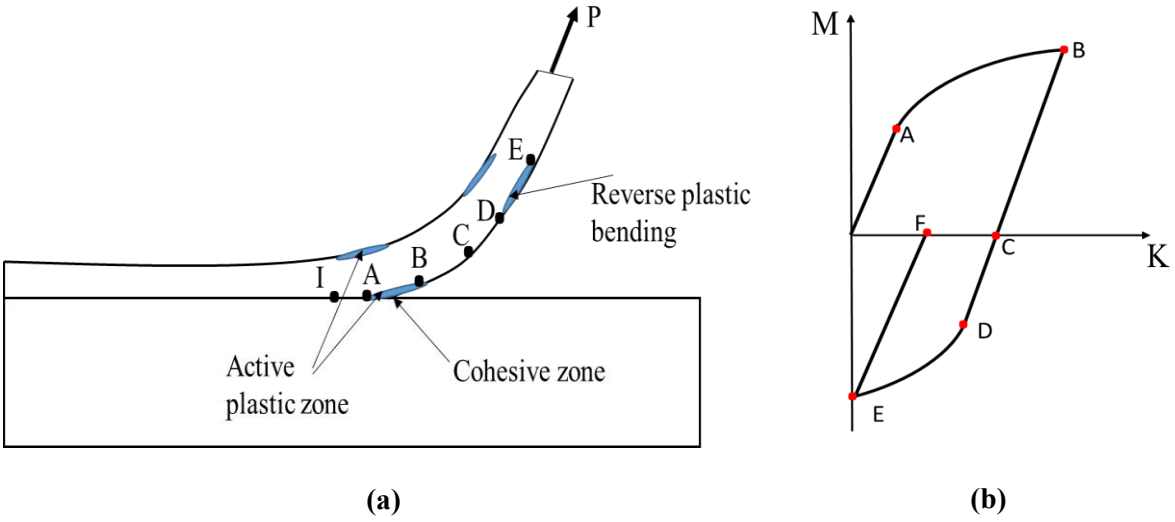

(a) **(b)**

Figure 2.12: (a) Schematic view of the process zone during peeling of elastic-plastic thin film *[40]* **(b)** Moment versus curvature under plane strain *[40]*.

As a consequence, from the energy balance of the peel test, the interface fracture energy can be derived from the knowledge of two experimental observations: force and angle at the tip. This model has been adopted and discussed widely in the literature. Kinloch et al [41] analyzed the case where the film may develop also plasticity during the test. Instead of considering a power law relation for the hardening behavior as in Kim and Aravas [6], they considered that for a certain class of material, the nonlinear response of the material can be modeled by a bilinear relationship. Therefore, an explicit expression for the plastic dissipation was also found. Wei and Hutchinson [7] adopted finite element calculations to analyze in detail the mechanical response of the system in the vicinity of the process zone, the detached arm still being analyzed with the bending approach. The interface response was modeled by introducing

cohesive elements. They also proposed a parametric analysis of the peel test based on non-dimensional parameters, see also Kim and Kim [19]. They clearly showed that the interface fracture energy is depending upon material parameters (elastic and plastic responses). Wei [40] compared the bending model of Kim and Aravas [6] and Aravas et al. [8] with the combined model of Wei and Hutchinson [7]. Wei [40] extended also the previous approach by accounting for the elastic compressibility. By still adopting a power law relationship for the hardening response of the film, a semi-analytical expression was found for the link between moment and curvature during the bending, but it was not possible to provide a simple expression for the reverse bending phase. So clearly, as the material description becomes more complex, the possibility to derive analytical or semi-analytical expression for the plastic dissipation is reduced.

Wei and Zhao [25] proposed a critical assessment of the different methods (bending versus combined bending + FE approaches). They illustrated their findings on specific configurations of metallic films of Aluminum or Copper on a ceramic. Peel tests were conducted at various angles (135° and 180°) in addition to 90 degrees. The thickness of the Al film was varying from 20 to 200 microns. They also considered ultra-thin film of copper deposited on the ceramic (from 1 to 15 microns). Based on the previous works (Wei and Hutchinson [7], Wei [40]), they concluded that the combined model (cohesive elements and bending of the free arm) is valid for a weak interface strength. For a strong interface case, a full finite element model is preferable. Zhao and Wei [22] confirmed that a two-parameter model is needed to obtain the interface energy from a peel test. Instead of measuring the base angle at the crack tip, they measured the curvature of the film during the bending/reverse bending process. With these two informations (force + curvature), the strength of the interface can be determined precisely. They were able to propose values for the cohesive law parameters (fracture energy and the separation strength). Experimental evidence based on copper thin films was discussed. To analyze T-peel tests on Cu/Cr/ polyimide system, Song and Yu [29] determined the mechanical response in tension of both Cu/Cr and polyimide. The plastic response of Cu was shown to saturate at very small plastic strain so the authors considered that copper has an elastic-perfectly plastic response. From the theoretical expression of the

plastic dissipation proposed by Kinloch et al. [41], Kim and Aravas [6] and Aravas et al. [8], the interface fracture energy was obtained.

2.4 Numerical simulation

As seen previously, some theoretical models provide interesting insights in the analysis of the peel test. Nevertheless, a complete description of the process can be only captured by finite element simulations. In the present part, we will discuss only contributions where the fracture of the interface is modeled by a cohesive zone. Clearly other methods to analyze the interface failure process in laminates exist in the literature. One can mention for instance the thick level set method, see Moes et al [42] and Gorris et al [43].

The cohesive zone model proposes to describe the mechanical behavior of the interface. It is based on the Dugdale [44] or Barenblatt [45] analyses of fracture mechanics problem in presence of plasticity near the crack tip. As mentioned in Tvergaard and Hutchinson [46], the cohesive law should be regarded as a phenomenological characterization of the zone where separation takes place. The cohesive law model was implemented in finite element calculation first by Needleman [47] to describe the process of void nucleation by inclusion debonding. Later, Needleman [48] developed a cohesive zone type interface model to study the decohesion of a visco-plastic block from a rigid surface. He observed that when the carrying capacity of the block is larger in tension then the interfacial strength, the decohesion is triggered in a tensile mode. Clearly, this work is of fundamental importance for the analysis of peel test.

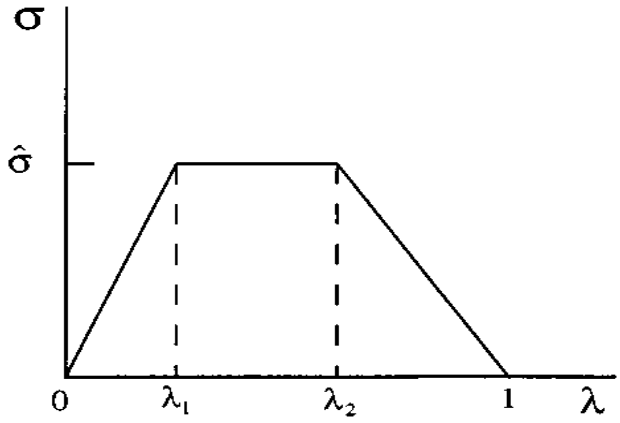

Figure 2.13: Traction-separation relation governing separation of the interface *[49]*.

Tvergaard and Hutchinson [46] adopted the same concept of cohesive law where the interface resistance is modeled through a traction-separation relation (Fig. 2.13) to analyze the crack growth initiation and propagation in elastic-plastic solids. The traction separation law in mode I is specified by the knowledge of three parameters: the interface strength $\hat{\sigma}$, the shape parameters $\lambda_1 = \frac{\delta_1}{\delta_c}$ and $\lambda_2 = \frac{\delta_2}{\delta_c}$ ($\lambda_1$and λ_2 are non-dimensional crack separation). δ_c can be viewed as the critical crack tip opening displacement (the critical displacement). The interface fracture energy is by construction:

$$\int_0^{\delta_c} \sigma d\delta = \frac{1}{2}\hat{\sigma}(\delta_c + \delta_2 - \delta_1) \tag{2.19}$$

This cohesive law was extended to mixed mode (traction and shear) by Tvergaard and Hutchinson [49]. These pioneering works have been adopted widely in the literature, so clearly it is impossible to summarize all the contributions even in the field of decohesion of interface. Wei and Hutchinson [7] have clearly mentioned that the most important parameters for the cohesive law are $\hat{\sigma}$ and δ_c. So the determination of the interface fracture energy is for sure related to the elastic or elastic-plastic properties of the bulk materials but also to the cohesive law parameters.

Various shapes of the traction-separation law were proposed in the literature. Kovalchick et al [21] adopted a power law formulation which was based on observations of the process zone, see Fig. 2.14. In Kovalchick et al [21], still two parameters are needed to calibrate the interface law. Their values are estimated based on observation of the shape of the peel arm in the vicinity of the tip.

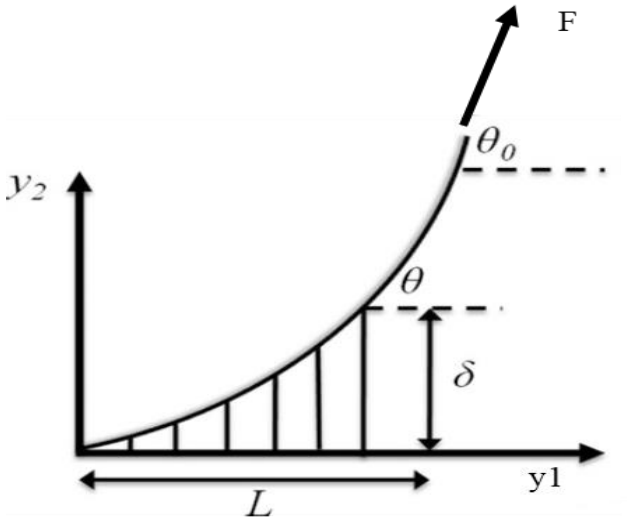

Figure 2.14: Cohesive zone for an elastic adhesive film bonded on a rigid substrate *[21]*.

Martiny et al. [9] developed a quasi-static steady-state FE model of the wedge-peel and fixed arm peel tests. In their model, the local fracture process ahead of the crack front was accounted for by embedding a cohesive zone between layers of elastic–plastic solid elements which represented the adhesive. Cohesive law parameters ($\hat{\boldsymbol{\sigma}}$, $\boldsymbol{\delta_c}$) were identified via an inverse method. Therefore, their FE model was compared to experimental data in terms of peel force and also curvature for three different angles. Cui et al. [50] adopted a critical fracture strain as a failure criterion. They considered aluminum peel arms of different thicknesses with an epoxy adhesive on rigid substrate. They observed cohesive failure during the peel test. With recourse to experimental data from 90° peel tests, the numerical FE model was calibrated to mimic data.

2.5 Conclusion

In this chapter, we saw through the state of the art, that a large number of studies concerns the peeling of thin films. From Kendall's [5] work about the peeling of elastic thin films onto a rigid substrate, the properties of the interface can be determined by using an energy balance. For the case of inextensible films, it has been seen that the decohesion energy of the interface is equal to the peel force (for a peel

test at 90°). This is not the case when plasticity is developed in the film. In peel test experiments, both the peel force and the film curvature at the peel front can be measured. We have seen in the work of Kim and Aravas [6] that the knowledge of the peel force alone is not sufficient to determine the properties of the interface during the peeling of an elastic-plastic thin film. Based on the previous analysis of the state of the art, in my PhD, we propose first to develop in chapter 3, dedicated experiments on the copper-composite materials. One needs in addition to calculate the plastic dissipation during elastic-plastic peeling. Indeed, as shown in Song and Yu [29], the flow stress of copper may saturate. As a consequence, instead of adopting an elastic-perfectly plastic response as proposed in Song and Yu [29], we propose to adopt a Voce type law to mimic such saturation like behavior. In chapter 4, we develop an analytical model for such behavior. From the study of Wei and Hutchinson [7], we adopt finite element calculations to analyze the peeling of an elastic-plastic thin film. Cohesive elements will be considered for that purpose. From the experimental data of chapter 3, for a peel angle of $\boldsymbol{\theta = 90°}$ the cohesive law will be calibrated. Finite element simulations of peel tests for various angles will be performed in chapter 5. It will be shown that the calibration enables to obtain consistent prediction for various peel angles. Finally, the validity of the IPC-TM-650 2.4.8 Standard [51] widely adopted in the PCB industry is discussed.

3 PEELING EXPERIMENT OF AN ELASTIC-PLASTIC THIN FILM ON AN ELASTIC SUBSTRATE

3.1 Introduction

In this chapter, we present all experiments conducted to measure the interface strength. Some of the equipments have been bought thanks to the support of ANR (Agence Nationale de la Recherche). Indeed, ANR has funded the LEMCI laboratory which is a common laboratory between LEM3 laboratory and CIMULEC. The peel test is widely used as the reference mechanical test for measuring the interface properties in the PCB industry. Experimental peel tests are conducted on specimens provided by CIMULEC company. Before doing the peeling test, we characterize the different materials used to manufacture specimens for the peel test. To determine the elastic and plastic properties of copper thin film, one needs to carry out tensile tests. Afterwards, peeling experiments of copper thin film on an elastic substrate are performed. During peeling, the peel force and copper film curvature are measured for each configuration (film thickness and peel angle). All the experiments are carried out at a room temperature 20°C, for two thicknesses: 35µm and 70µm.

3.2 Specimen materials

For the experimental part, we have prepared samples which are representative of materials used in real applications. For that purpose, pre-impregnated (pre-preg) epoxy glass fibers material and copper thin film have been processed according to the industrial standard by CIMULEC company. The specimens used in this thesis for the peel test is made of copper thin foil (35µm and 70µm thick) and of woven composite made (glass fibers and epoxy resin). In this PhD we will consider only HTE (High Tension Elongation) grade 3 copper film**.**

3.3 Specimen manufacturing

The condition of the delamination between materials is strongly influenced by the way, the film is bonded to the substrate. Processing conditions including time, temperature, and pressure are identical for all the specimens because adhesion properties can be affected by these conditions. After stacking copper film on the composite (pre-preg), a pressure was applied using a hot press at a temperature of 192°C (step a, Fig. 3.1). The curing of the pre-preg materials at elevated temperature ensures the adhesion of copper foil. After 60 min, the specimen is removed from the hot chamber and cooled at room temperature (step b, Fig. 3.1). Note that the bonding of the copper film is realized only on 2/3 of the total length of the specimen so that the unbonded part of the film can be peeled manually and fixed in the grip of the MTS peeling machine. After cooling the specimen to room temperature, a 10 mm width of the copper film is etched on the surface of the sample (step c, Fig. 3.1). Finally, the specimen is ready for peeling (step d, Fig. 3.1). The copper film used in our investigation has 10 mm width and 35µm or 70 µm thickness. The composite substrate used for the specimen has the following dimensions: 200mm, 55mm, 1 mm for the length, width, and thickness, respectively. The shape and the dimension of the specimen are shown in Fig. 3.2.

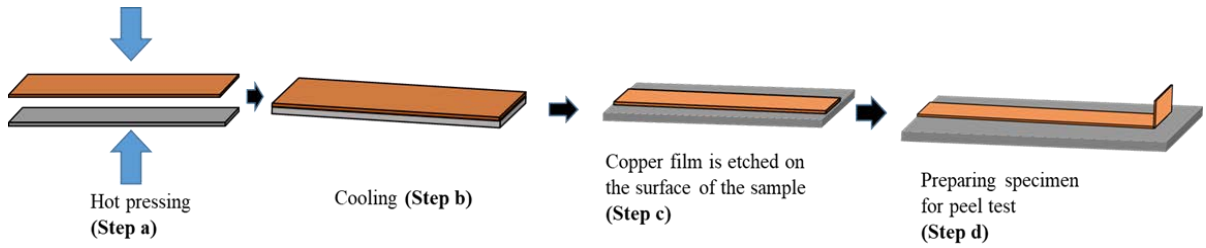

Figure 3.1: Method for preparing specimens used in the peel tests.

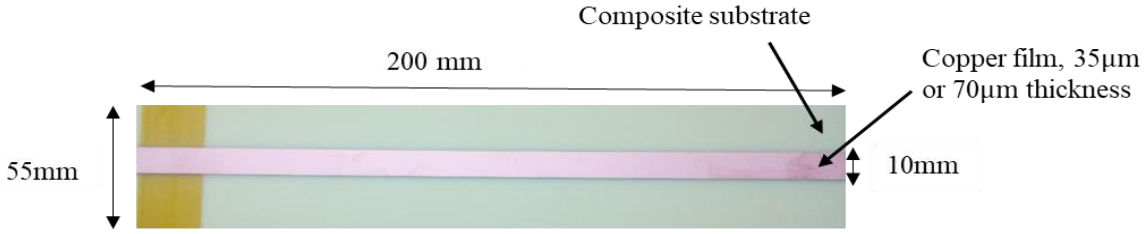

Figure 3.2: The shape and the dimension of the specimen used for peeling. The samples are prepared by CIMULEC company.

3.4 Uniaxial response copper thin film

A dedicated device (Instron E3000) is used to determine the mechanical response of the copper thin film. In LEM3, an Instron E3000 electrodynamic tensile machine equipped with a climatic chamber is available. The chamber enables to perform tests up to 300°C and can be cooled with liquid nitrogen at -60°C see Fig. 3.3.

Uniaxial tensile tests on copper film are performed at room temperature and with different orientations (Fig. 3.4) to validate the in-plane isotropy of the elastic-plastic response. Fig. 3.5 presents the true stress-true strain curve for a film of 35µm thickness. The corresponding curve for the film of 70µm thickness is given in chapter 5, see Fig. 5.11(a).

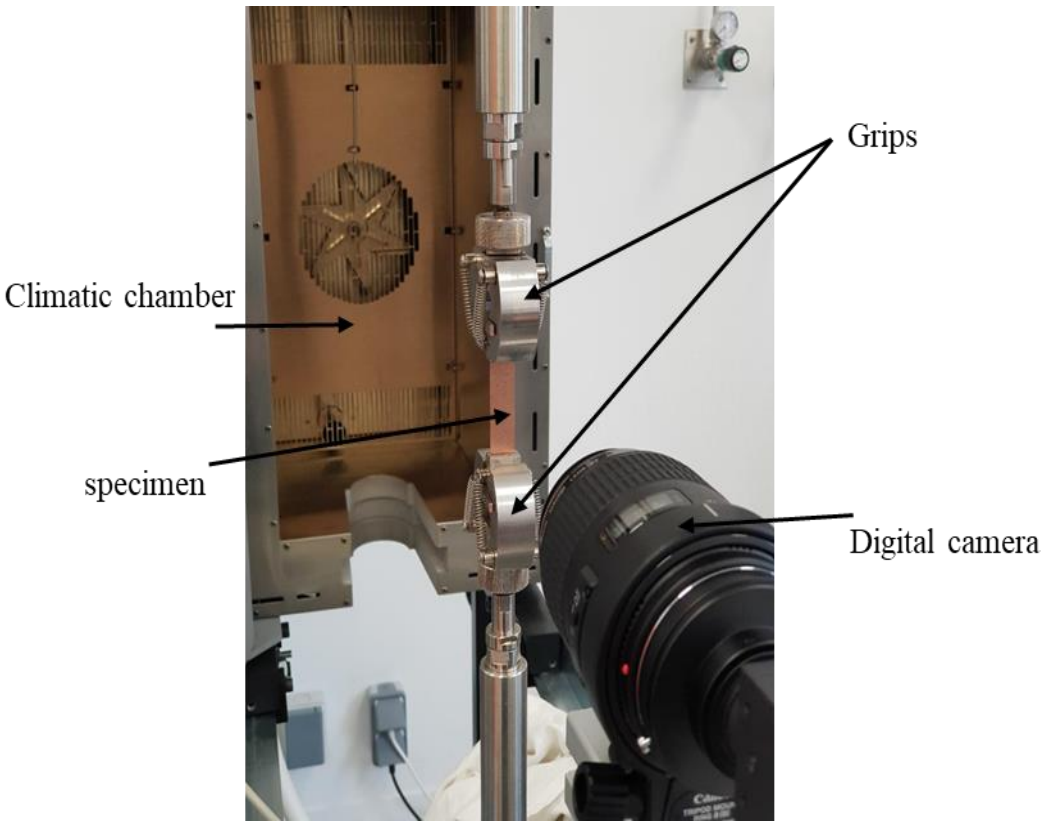

Figure 3.3: Tensile set-up used for determining the mechanical response of the material (copper or composite).

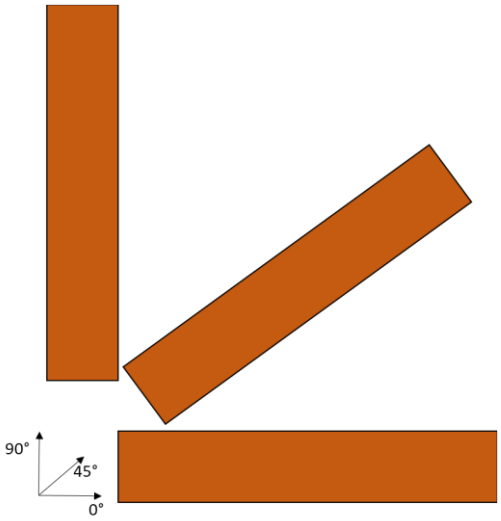

Figure 3.4: Copper specimen with different orientations for the tensile test.

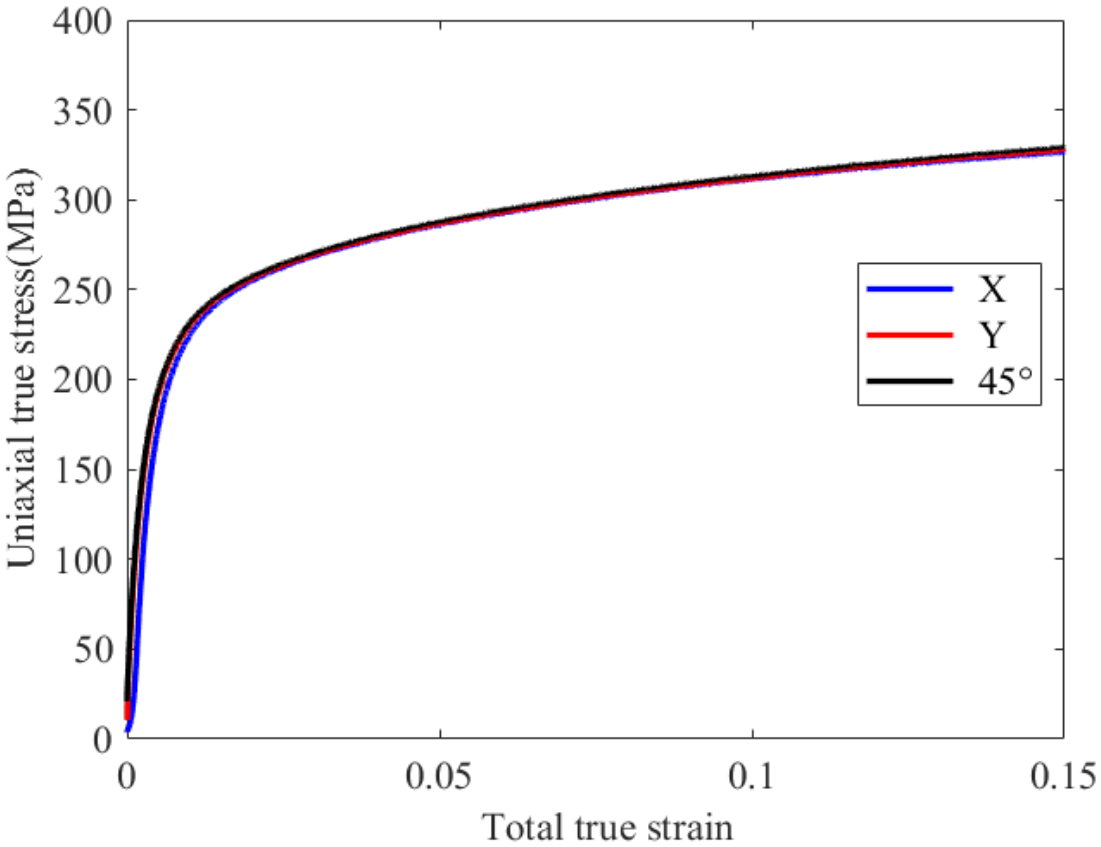

Figure 3.5: True stress versus true strain for 35 μm thick copper. Tests are carried out for three orientations**.**

The tests are conducted with a crosshead displacement rate of v = 0.5mm /s. Note that the same velocity will also be adopted for peel tests of the next section. The force is measured by a load cell with a maximum capacity of 1kN placed under the lower grip of the machine. At the same time, a computer recorded automatically the force. Strain measurements are performed by digital image correlation. For this purpose, the copper sample is covered with a speckle pattern made by black paint droplets, see Fig. 3.6. The pattern is tracked by the VIC 2D software from one image to the next one in order to calculate the deformation on the surface of the specimen. A mapping of the displacements and deformations on the surface of the specimen is then obtained. Fig 3.7 presents the measurements of horizontal and vertical displacements during the uniaxial tensile test.

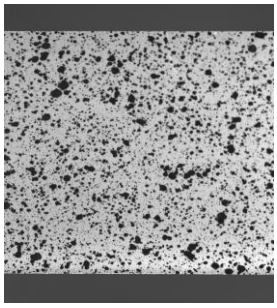

Figure 3.6: Copper sample covered with mouchetis made by spray of paint droplets.

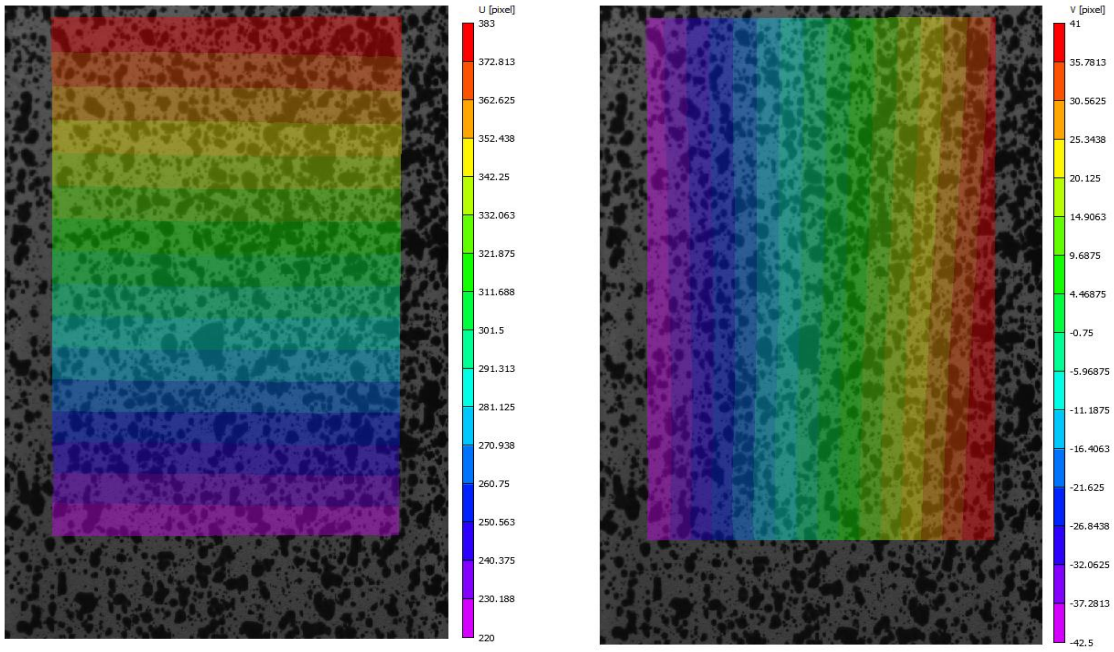

(a) Vertical displacement **(b)** Horizontal displacement

Figure 3.7: Digital image correlation during the tensile test of copper film.

It has checked that the strain field is almost uniform and is representative of uniaxial test in the gauge length. Average values of the ε_{xx} and ε_{yy} strain components are evaluated on the specimen surface. Therefore, the force, the longitudinal strain and transversal strain are recorded for each time t. Note that to evaluate precisely the Young's modulus of copper, unloadings have been carried out at different stages of the deformation process see Fig. 3.8(a). The true stress-strain and transversal strain as function of longitudinal strain curves are plotted in Fig. 3.8 (a) and (b). The Young's modulus for the 35 µm thick copper is E = 106 GPa and the Poisson's ratio is ν = 0.36 at room temperature.

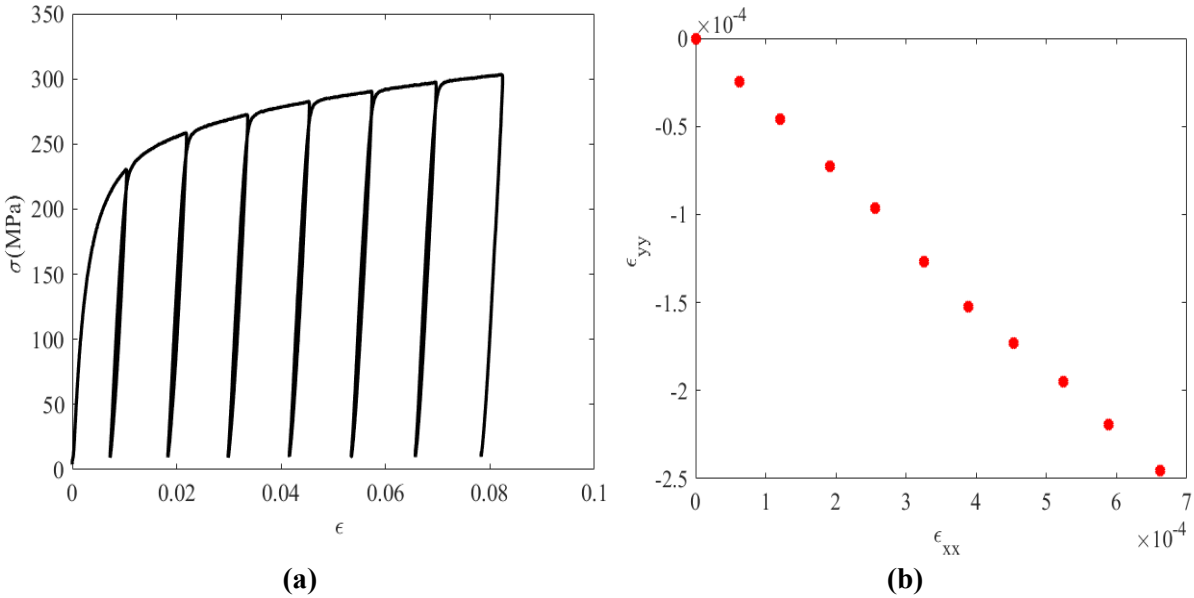

Figure 3.8: **(a)** Stress-strain curves during an uniaxial tensile test on a 35µm thick. Unloadings are performed to identify the Young's modulus **(b)** Transversal strain-longitudinal strain to identify the Poisson's ratio during unloading.

Owns to the small thickness the results are really sensitive to the film thickness. The thickness of the samples is measured using an optical microscope by observation of cross-sections, see Fig 3.9 (a). The real thickness is slightly different from data of the supplier. These thickness measurements must be made as accurately as possible because a difference of few micrometers has a significant influence on the calculation of the stress. We made several measurements of the thickness on three different specimens of copper film and the thickness value is obtained by doing an average of all measurements. Fig 3.9 (b) and (c) show the thickness measurement results for the two different thicknesses. In fact the

films have respectively a thickness of 35µm and 72µm. A comparison is made with the value proposed by the supplier, see Fig. 3.9 (b) and (c).

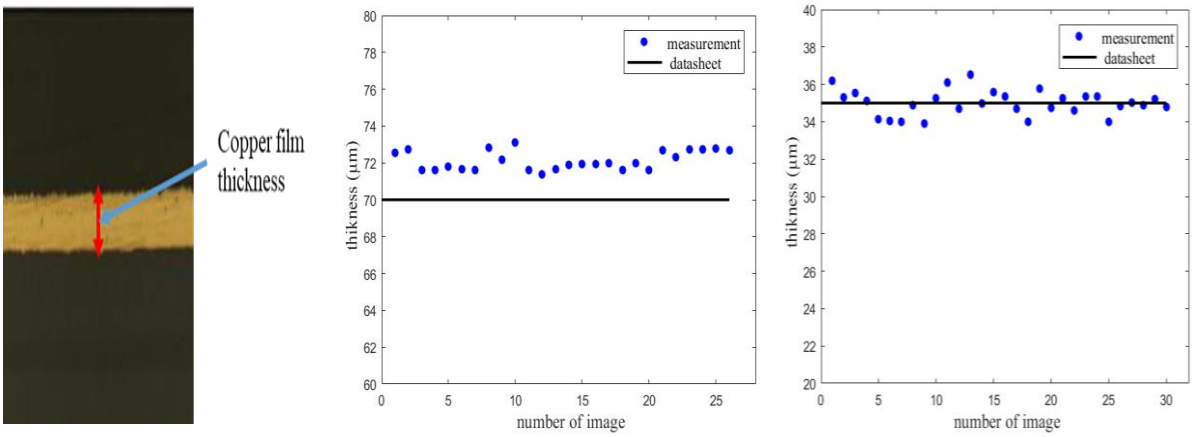

(a) **(b)** **(c)**

Figure 3.9: Measurement of the copper film thickness **(a)** Optical microscope image for measuring copper thickness, **(b)** Measurement on the 70μm thick film, **(c)** Measurement on the 35μm thick film

During the peel test experiment, plastic deformation occurs in the copper film. Therefore, it is essential to identify the plastic behavior. Uniaxial tensile tests are repeated several times for the HTE grade 3 copper film and for two different thicknesses: 35 µm and 70 µm. As expected, the elastic limit of pure copper thin film is relatively low. At small strain, it is observed that the yield stress increases rapidly with strain and after 1% strain, the hardening behavior is somehow quite linear. From the tensile tests, it is clear that the HTE grade 3 copper with 35 µm and 70 µm thicknesses have different elastic-plastic behaviors (see Fig. 5.11(b) for 70 µm). Note that the two copper foils have undergone the same heat treatment at CIMULEC (the copper film is laminated at 192°C during one hour). In the following, the real elastic-plastic behavior will be used in numerical simulations (Chapter 5). The plastic response of copper will be approximated by adopting a Voce law, the elastic response being assumed isotropic.

3.5 Elastic behavior of the substrate

The substrate is a composite with glass fibers and epoxy resin often used in the PCB industry. The elastic behavior of the woven composite substrate is orthotropic. The in-plane elastic moduli are measured by

tensile tests carried out at various angles (0°, 45°, 90°). The elastic behavior in the out-of-plane direction is difficult to evaluate experimentally. To obtain the out-of-plane behavior, numerical simulations are used at the level of the internal structure of the substrate. The in-plane Young's modulus is around 20.3 GPa, while the out-of-plane one is 16.4 GPa, the in-plane Poisson's ratio is 0.17 see Table 3.1. For a clear description of the different techniques used to determine the elastic behavior of the substrate (woven composite), the reader may find additional information in the PhD thesis of G. Girard [52] or in G. Girard et al [53].

E_1[MPa]	E_2[MPa]	E_3[MPa]	ν_{12}	ν_{13}	ν_{23}	G_{12}[MPa]	G_{13}[MPa]	G_{23}[MPa]
20270	20800	16338	0.17	0.453	0.45	4610	2442	2982

Table 3.1 : Elastic modulus of the woven composite used in printed circuit boards at room temperature. The method proposed in Girard et al [53] is used to capture all components.

3.6 Peel test experiments

In order to determine the interface strength between the copper thin film and the composite substrate, an experimental peeling device has been bought at the beginning of the PhD. This MTS machine is equipped with a rolling table to perform peel tests at different peel angles ranging from 0 ° to 180 °. The maximum displacement of the MTS machine is 1000mm, the maximum velocity of the machine is 50mm/s. The load cell capacity used for peel tests is 50N.

The specimen of Fig. 3.2 is screwed to the table of the machine and the unbounded part of the copper film is inserted in the top grip of the device, see Fig. 3.10. During the peel experiment, the velocities of the crosshead and of the table are identical (0.5 mm / s) since an inextensible cable links the table and the crosshead, see Fig. 3.10. Peel tests are conducted for a large range of angles (45°, 60°, 90°, 120° and 135°). The film is under zero force prior to peeling. Owing to the load cell of the MTS device, the peel force is recorded as a function of the displacement of the cross-head. Fig. 3.11 shows a typical plot of the peel force versus displacement for a 90° peel test at a velocity of 0.5mm/s. As the film is peeled, the peel force increases until a steady state is reached. We observe two regions on Fig. 3.11: the first region where the decohesion process is triggered followed by a second region where a constant force is recorded

during the experiment. Note that for each configuration, the steady state occurs after few millimeter (mm) displacement of the cross head. In all tests, a total crosshead displacement of 20 mm is imposed. Peel tests were performed at least three times for each peel angle to ensure the repeatability of the measurements. The peel force per unit width is calculated by dividing the average force during the steady state region by the width of the film. The initial and final stages of the specimen are presented in Fig. 3.12.

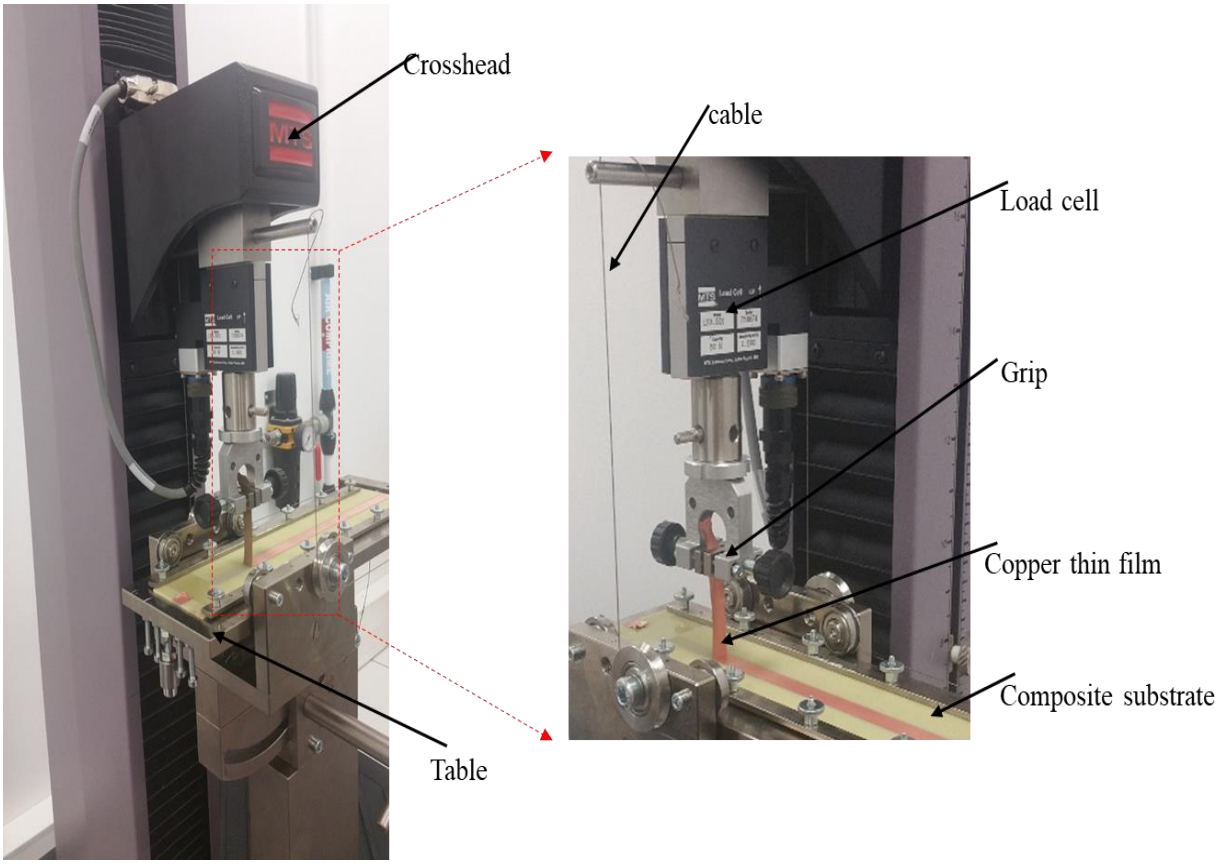

Figure 3.10: Experimental peeling configuration used in the PhD**.**

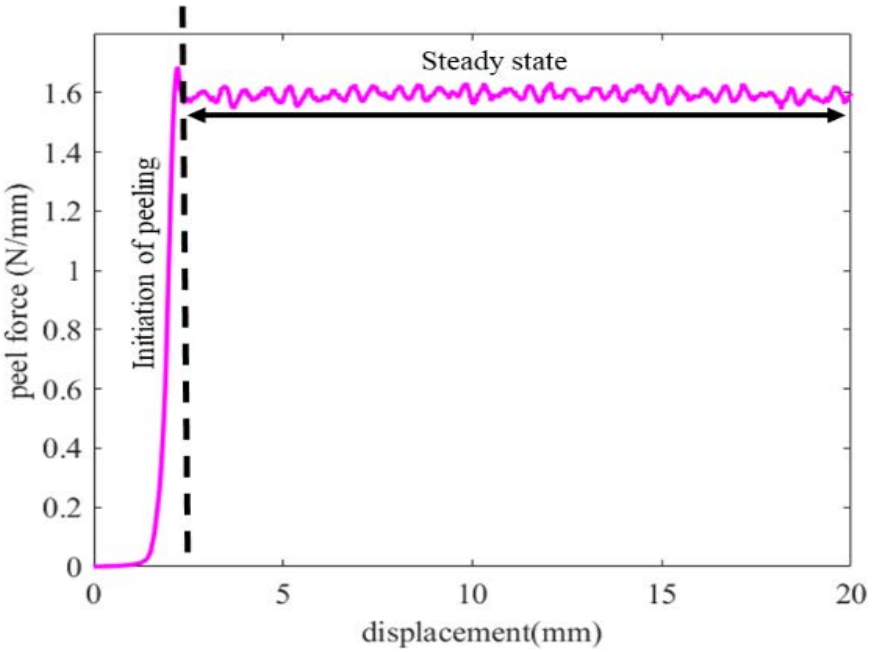

Figure 3.11: Force per unit width versus displacement obtained for a peel test at 90°. The peel force corresponds to the average value of the force during steady state. A 35 µm copper film is considered here**.**

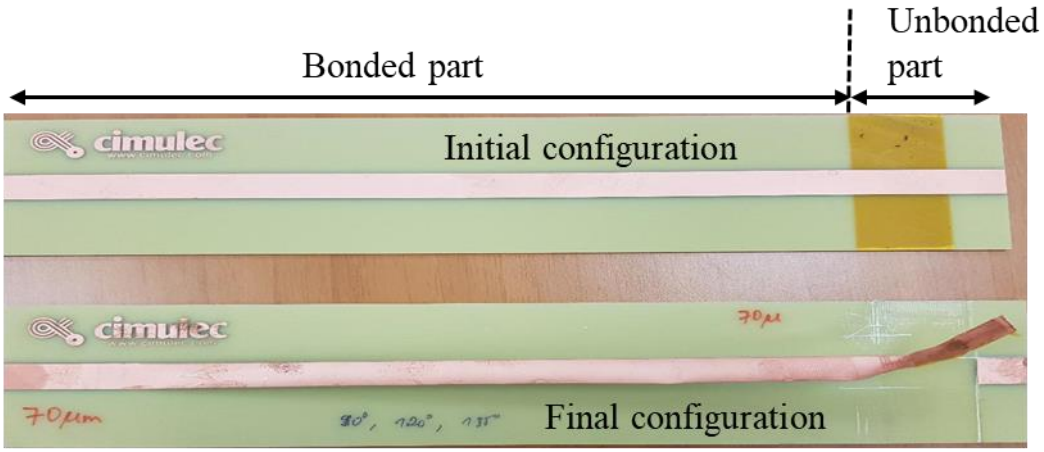

Figure 3.12: The initial and final configurations of the peel test specimen. Here the film thickness is 70 µm.

Figs. 3.13 (a-e) and Figs. 3.14 (a-e) show the variation of the peel force per unit width with the displacement for different angles (45°, 60°, 120° and 135°) and for the two copper films (35 µm and 70 µm thick). We can see on Figs. 3.13 (a-e) and Figs. 3.14 (a-e) that the initiation of peeling is not identical for all tests, since the unbonded film is attached to the grip manually in a different manner for each test. During steady state, the peel force is clearly identical for all tests made under the same conditions. We clearly observe from these figures the repeatability of our tests in the steady state region. Fig. 3.13 (f), and Fig. 3.14 (f) present the evolution of the peel force per unit width versus peel angle. As the peel angle increases, the peel force at steady-state decreases. This result agrees well with previous studies, see Molinari and Ravichandran [11], Kinloch et al [41]. It is also observed that as the thickness is increased, the peel force is larger. The difference between the two film thicknesses will be rationalized later after the theoretical section. Table 3.2 summarizes the corresponding results of Fig. 3.13(f) and Fig. 3.14(f).

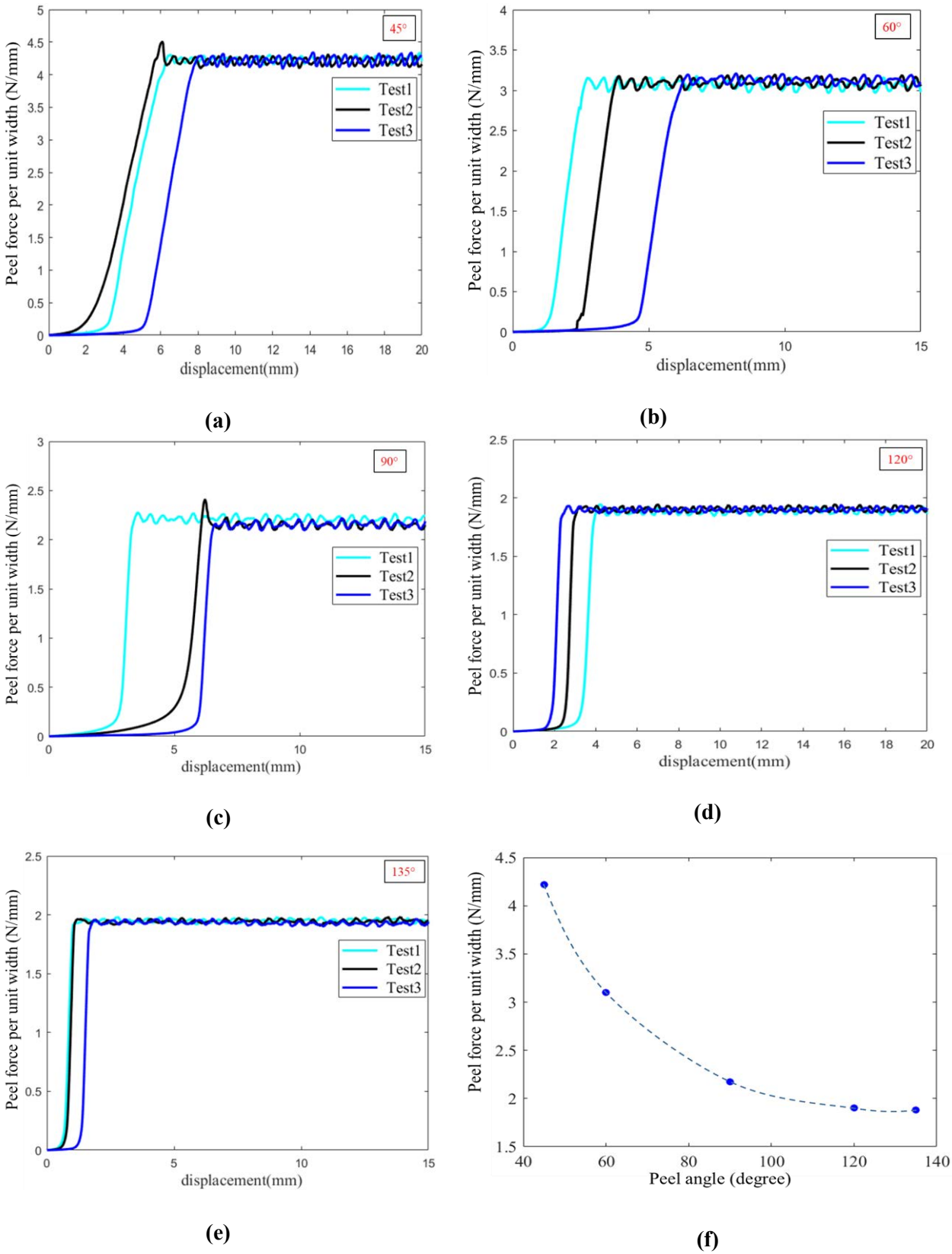

Figure 3.13: Evolution of the peel force per unit width as a function of the displacement for different angles: **(a)** 45°, **(b)** 60°, **(c)** 90°, **(d)** 120°, **(e)** 135°. **(f)** Variation of the peel force per unit width as a function of peel angle. Experimental results are obtained for the 70 µm thick copper film.

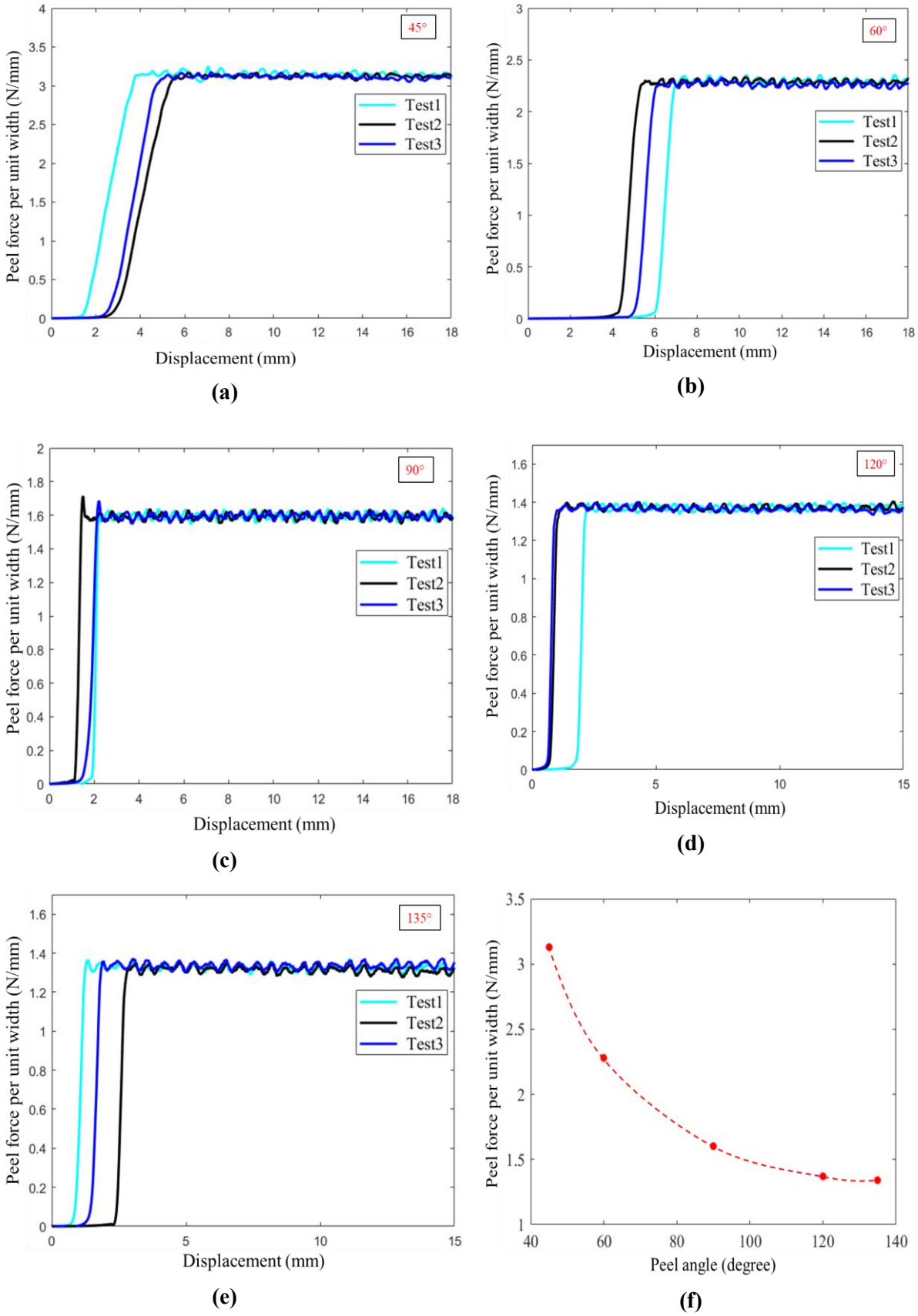

Figure 3.14: Evolution of the peel force per unit width as a function of the displacement for different angles: **(a)** 45°, **(b)** 60°, **(c)** 90°, **(d)** 120°, **(e)** 135°**. (f)** Variation of the peel force per unit width as a function of peel angle. Experimental results are obtained for the 35 µm thick copper film.

	Film thickness (35 µm)	Film thickness (70 µm)
Peel angle	Peel force per unit width (N/mm)	Peel force per unit width (N/mm)
45°	3,2	4,22
60°	2,2	3,1
90°	1,6	2,17
120°	1,38	1,91
135°	1,37	1,89

Table 3.2: Peel force per unit width measured during the steady state region, for the two thicknesses: 35µm and 70µm.

From the bibliography section, a second important feature from experimental tests is the curvature of the film. Indeed, as shown in Aravas et al [8], the plastic dissipation is strongly related to the curvature. During peel test, a high-resolution digital camera with macro lens records images of the specimen in the vicinity of the process zone, see Fig. 3.15 (a). This macro lens is designed to provide magnification of the critical area up to 5 times. Fig. 3.15 (b) shows a picture of the copper film curvature during steady state for a 90° peel test. The film thickness is here 70 µm.

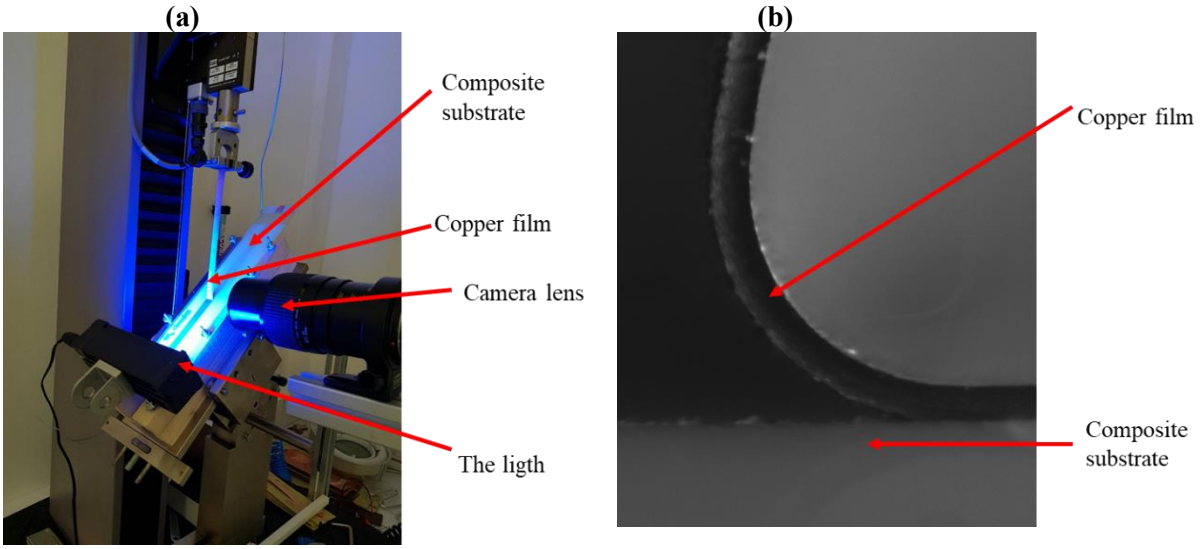

Figure 3.15 : Determination of the film curvature during peel test. **(a)** Peeling device equipped for the measurement of the film curvature. **(b)** Picture of the 70 µm thick copper film during peeling at 90°.

In order to determine the radius of the copper film for each peel angle during the stationary part of the peel test, ORIGINPro software has been used. For that purpose, we capture a reference image with a pattern usually adopted for stereo digital image correlation. By using the camera, one can define a pixel based scale. With this method, the curvature of the peel arm can be determined with good accuracy. In Fig. 3.16, the shape of film at the peel front is approximated with a circle where **R** is the radius of the top surface. This measurement is repeated three times on three different pictures recorded on three different tests. Fig. 3.16 shows the adopted circle to approximate as closely as possible the curvature of the upper surface of the film. The film thickness is 70 µm. The same strategy has been performed for the two thicknesses and for all peel angles, see Fig. 3.17 for results with h=70 µm only.

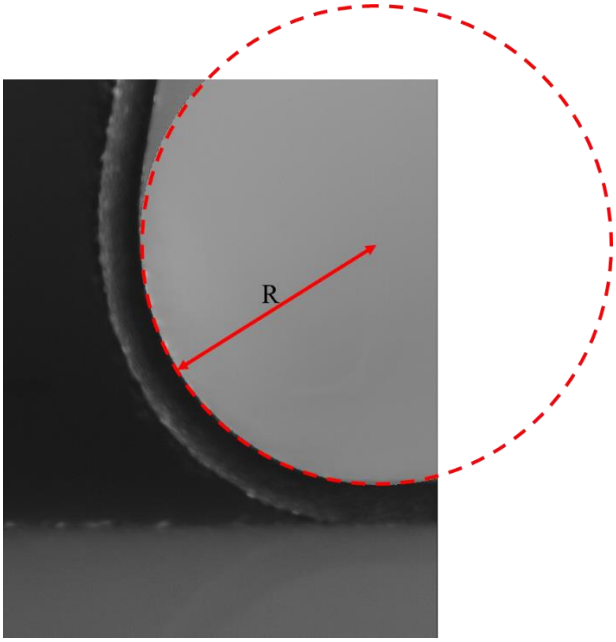

Figure 3.16: Picture of the circle approaching the curvature of the upper surface of the film. The peel angle is 90° and the film thickness is 70 µm.

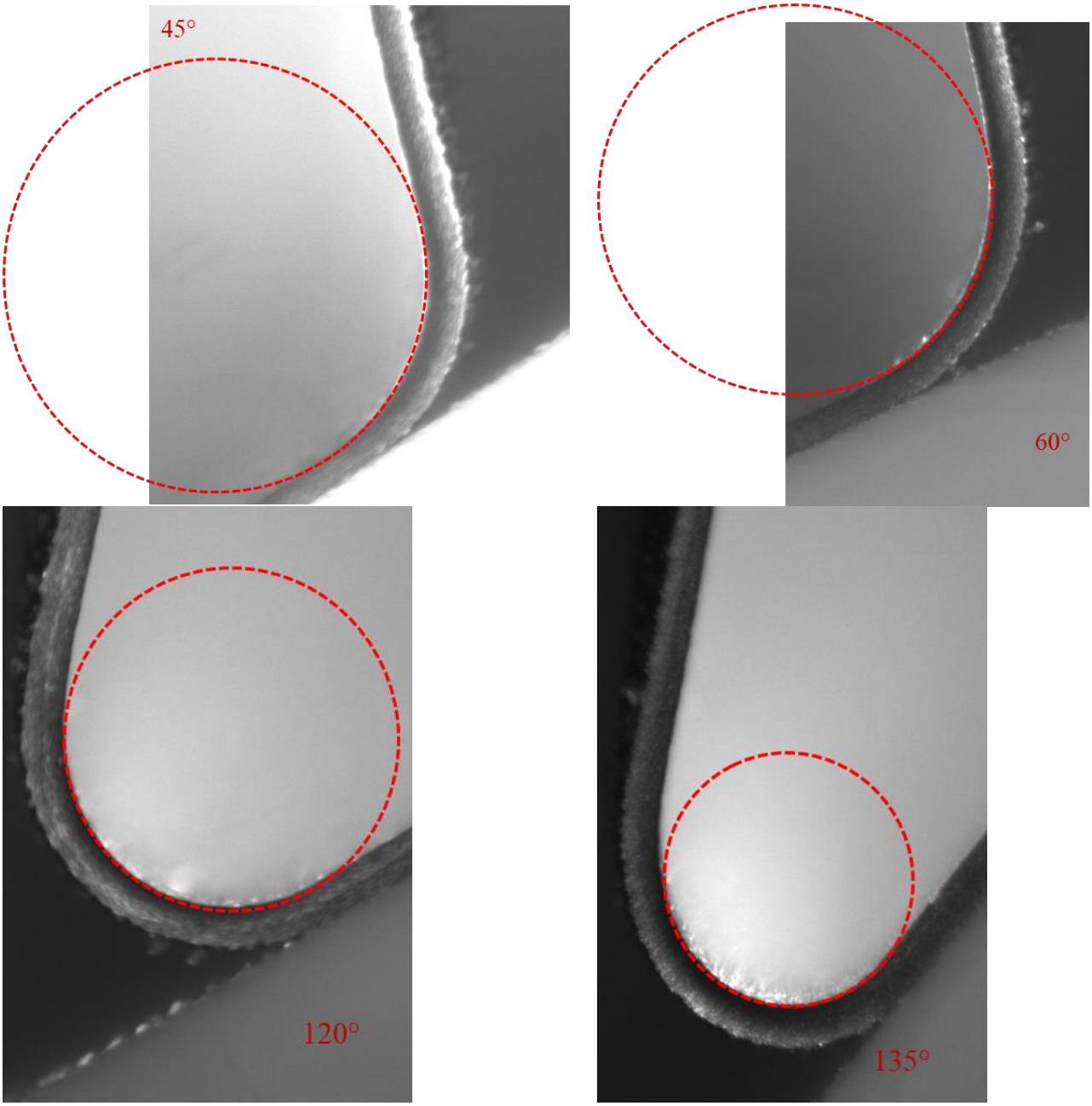

Figure 3.17: Evaluation of the curvature by the circle method. The peel angle is varying in the range 45° to 135°. The film thickness is 70 µm.

Table 3.3 (resp 3.4) shows the radius values of the circle measured for a 70µm thick (resp 35µm) copper film. Note that in this section, the radius R corresponds to the radius of the upper surface of the film, see Fig. 3.16. Clearly, the three measurements are consistent so that the average value will be adopted in the modeling part. One also observes in Table 3.3 and 3.4 that the radius of curvature decreases when the peel angle increases. The radius is also larger with larger film thickness since the bending stiffness of the thicker film is larger. In the analytical section, as presented in the work of Kawashita et al [26], half

of the thickness is added to the measured value to define the radius of the central surface. Note that the dispersion of the 45° peel test is larger when compared to other peel angles. Indeed, as seen in Fig 3.17 when the peel angle decreases, fitting the top surface by a circle is more questionable.

Peel angle (70 µm)	**Measure 1 R (µm)**	**Measure 2 R (µm)**	**Measure 3 R (µm)**	**Average (µm) value of R+h/2**
45°	645,6	653,0	656,5	**651,3+35=686,3**
60°	539,3	540,0	540,5	**540,0+35=575,0**
90°	384,6	385,4	385,5	**385,2+35=420,2**
120°	280,1	279,5	281,4	**280,3+35=315,3**
135°	244,0	245,8	247,8	**245,9+35=280,9**

Table 3.3: Value of the radius of upper surface of the film (three measurements) and the corresponding value of the radius of the central surface. The copper film thickness is **h=70µm**.

Peel angle (35 µm)	**Measure 1 R (µm)**	**Measure 2 R (µm)**	**Measure 3 R (µm)**	**Average (µm) value of R+h/2**
45°	195,6	195,8	195,9	**195,8+17,5=213.3**
60°	170	168,4	169,6	**169,3+17,5=186,8**
90°	124	124,5	124,2	**124,2+17,5=141,7**
120°	95,5	95,8	96,0	**95,7+17,5=113.2**
135°	70,1	70,3	70	**70,1+17,5=87,6**

Table 3.4: Value of the radius of upper surface of the film (three measurements) and the corresponding value of the radius of the central surface. The copper film thickness is **h=35 *µ*m**.

3.7 Conclusion

In this chapter, we have developed experimental tests to determine the elastic-plastic properties of the copper film. The elastic-plastic behavior obtained is this chapter will be used in the next chapters for modeling and numerical simulations. Peel tests have been also performed to measure the peel force per unit width. Peel tests at 5 different angles (45°, 60°, 90°, 120°, and 135°) are carried out. Two film thicknesses are adopted (**70 μm** and **35 μm**). Results show that the value of the peel force during the steady state is reliable. As observed in the literature, the peel force decreases when the peel angle increases. An experimental method based on high resolution digital camera enables to measure the curvature of the copper film. It is shown that as the peel angle increases, the film radius decreases. When the thickness is larger, the radius is strongly enlarged. These trends were already reported in the literature. Nevertheless, with the present work, we have defined all necessary quantities (peel force, radius, behavior of copper) which are necessary to define precisely the interface fracture energy. Usually in the literature, some of the information are not available.

4 ELASTIC-PLASTIC ANALYSIS OF THE PEEL TEST FOR DUCTILE THIN FILM WITH SATURATION OF THE YIELD STRESS

4.1 Introduction

In this chapter, we propose a contribution to the precise definition of the dissipated energy (more precisely work done by bending plasticity) due to plasticity during bending-reverse bending for a particular class of material responses. Indeed, as shown in Song and Yu [29], the yield stress of copper saturates rapidly. As a consequence, instead of adopting an elastic-perfectly plastic response as proposed in Song and Yu [29], we propose to adopt a Voce type law to mimic such saturation like behavior. It is also interesting to mention that depending on the material parameters, a linear hardening stage can also be modeled (for moderate strain) by adopting a Voce hardening law. This chapter is organized as follows. First the geometrical configuration and the material response are presented. In a second part, a semi-analytical expression for the bending-reverse bending of metallic material with a Voce law is proposed. Therefore, the plastic dissipation can be derived. Closed form expression is provided in some specific cases. Finally, the proposed expressions are compared to the Aravas et al. [8] approach and validated based on finite element simulations of peeling (see chapter 5). The development in this chapter is published in International Journal of Fracture (Simlissi et al [54]).

4.2 Configuration

A two-layer woven composite/Cu sample is considered in this theoretical work. This configuration is representative of the one often present in Printed Circuit Boards (PCB). More generally, a system with

a thick elastic substrate and a thin ductile film can also be investigated through the proposed approach. As shown in Fig. 4.1, the metallic film thickness h is usually small compared to the one of the substrate (between 17.5µm and 70µm). Song and Yu [29] characterized electroplated Cu layer under uniaxial tension. The measured uniaxial stress was saturating at early stage of the deformation. Based on this observation, they analyzed T-peel test by adopting the elastic-perfectly plastic analysis proposed by Aravas et al. [8] and Kinloch et al. [41]. Instead of considering the material as an elastic-perfectly plastic one, we propose to model its plastic response by adopting a Voce law [55]. In that case, the elastic-plastic mechanical response is written as:

$$\bar{\sigma} = E\bar{\varepsilon} \quad \text{for} \quad \bar{\sigma} \leq \sigma_0 \tag{4.1}$$

$$\bar{\sigma} = \sigma_0 + Q(1 - \exp(-\gamma(\bar{\varepsilon} - \varepsilon_0))) \quad \text{for} \quad \bar{\sigma} \geq \sigma_0 \tag{4.2}$$

where E is the Young's modulus, $\bar{\sigma}$ the equivalent von Mises stress, $\bar{\varepsilon}$ the accumulated strain and $\varepsilon_0 = \frac{\sigma_0}{E}$. The material is assumed incompressible. In the following of this chapter, when plastic yielding is triggered, the flow stress (4.2) is written in a different way:

$$\bar{\sigma} = \alpha - \beta\exp(-\gamma\bar{\varepsilon}) \tag{4.3}$$

With $\alpha = \sigma_0 + Q$ and $\beta = Qexp(\gamma\varepsilon_0)$.

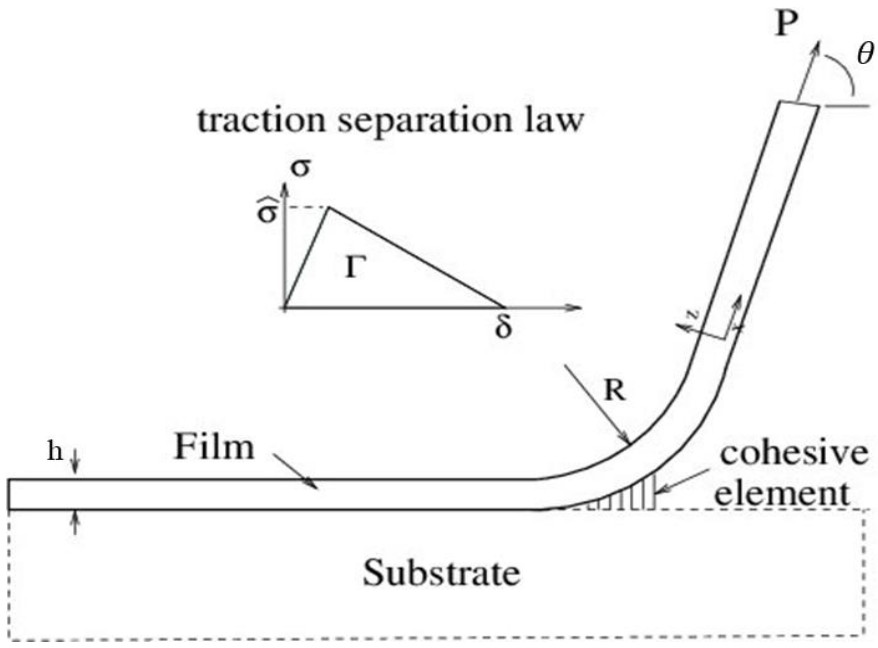

Figure 4.1: Peel test configuration. The film thickness is h. The peel angle is θ and the force per unit width is P. The traction separation law is also presented where $\hat{\sigma}$ represents the peak stress and Γ the interface fracture energy. A local coordinate system is adopted so that the position z = 0 corresponds to the middle plane of the film. During peeling, the film is facing bending. Let us note R the radius of curvature of the top surface $z = \frac{h}{2}$.

With the present modeling, the initial yield stress is σ_0 and the saturation value of the yield stress is α, see Fig. 4.3 for an illustration of the adopted response. The present work can be viewed as an application of the bending approach proposed by Kim and Aravas [6] for a specific material response with a saturation of the flow stress. The moment curvature relationship during peel test is analyzed assuming that 2D plane strain prevails, following the work of Kim and Aravas [6], Aravas et al. [8], Kinloch et al. [41] or more recently Wei [56]. The main equations of the analysis are recalled below with emphasis of the novelty in the moment curvature relationship induced by considering the Voce law for plastic yielding. During the steady state phase of the test, any material point will experience a bending/reverse bending path, see Fig. 4.2. So the stress and strain tensors are (neglecting shear components):

$$\sigma = \begin{bmatrix} \sigma_{11} & 0 & 0 \\ 0 & \frac{\sigma_{11}}{2} & 0 \\ 0 & 0 & 0 \end{bmatrix} \qquad \varepsilon = \begin{bmatrix} \varepsilon_{11} & 0 & 0 \\ 0 & 0 & 0 \\ 0 & 0 & -\varepsilon_{11} \end{bmatrix} \tag{4.4}$$

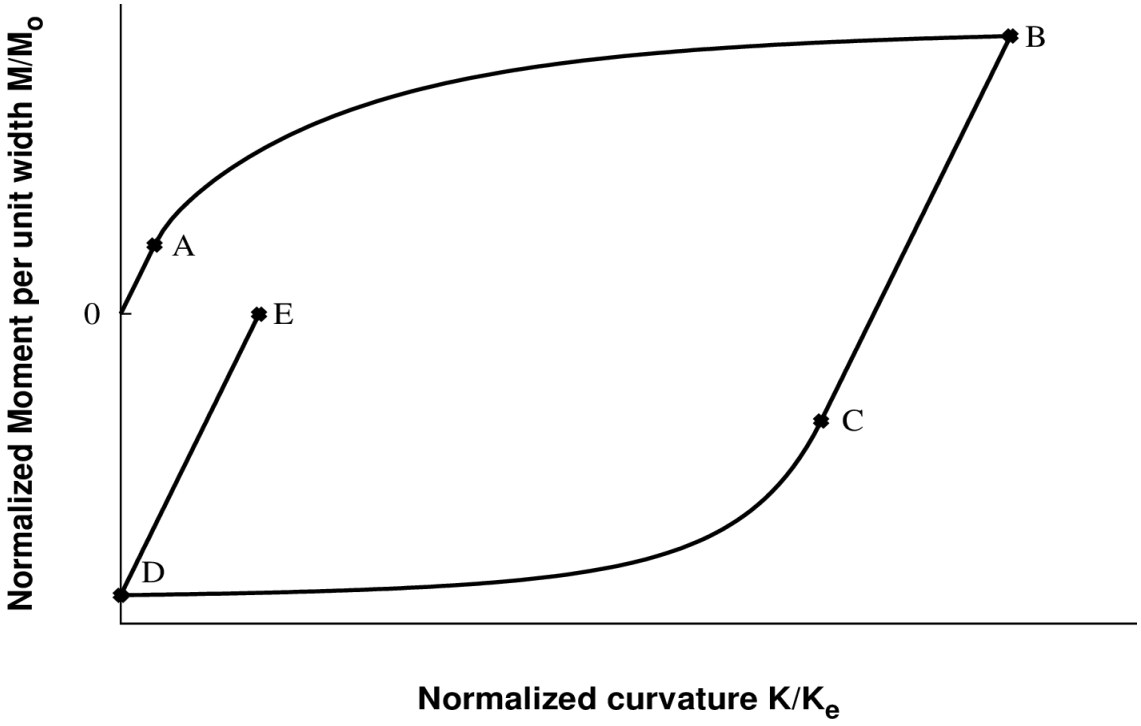

Figure 4.2: Schematic normalized moment versus normalized curvature under plane strain. Letters correspond to specific loading phases during peeling. The present results are obtained for the curvature $K_B = 4000m^{-1}$ $(\frac{K_B}{K_e} = 52)$. Material parameters are those of Table 4.1.

In the elastic domain, path (OA), from the Hooke's law and owing to incompressibility, one has $\sigma_{11} = \frac{4E}{3}\varepsilon_{11}$. During plastic loading, one obtains $|\sigma_{11}| = \frac{2}{\sqrt{3}}\bar{\sigma}$. Pure bending is supposed to prevail so as in Kim and Aravas [6], the axial strain is related to the position of the material within the cross section by $\varepsilon_{11} = -Kz$ where K is the curvature of the central surface ($z = 0$) and z is varying in the range $\left[-\frac{h}{2}, \frac{h}{2}\right]$. In Section 4.3, it will be shown that for a certain range of material parameters, even if the pure bending approach is not fully justified, the work done by bending plasticity is still estimated accurately. This aspect was already mentioned in Kim and Kim [19].

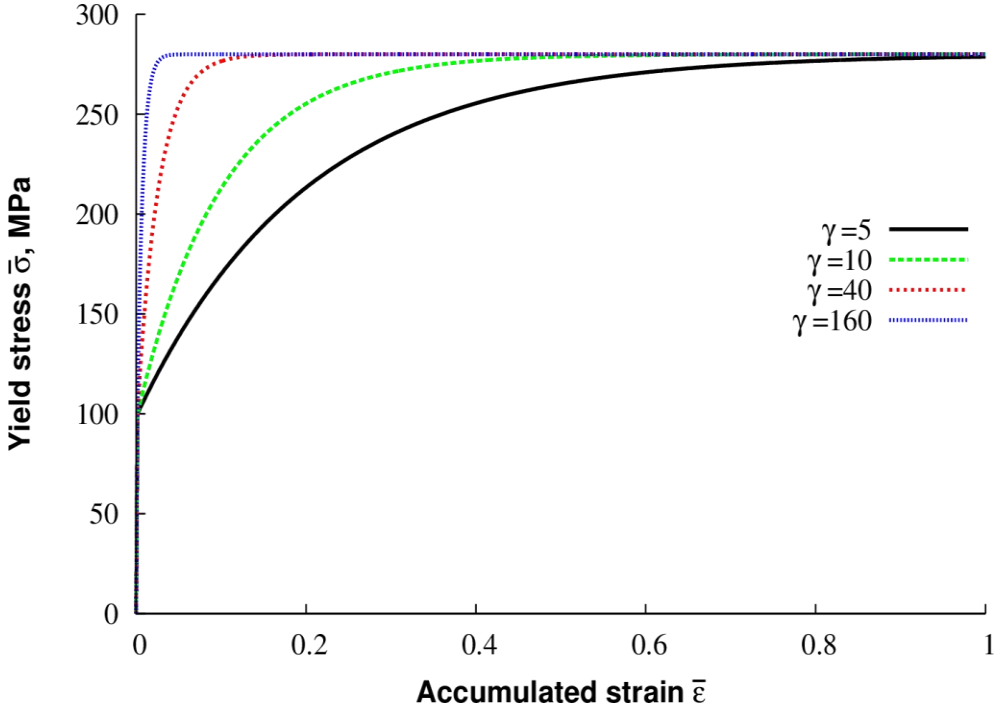

Figure 4.3: Elastic-plastic behavior of the metallic film. A Voce type behavior Eq. (4.2) is considered. Depending on the value of γ, the saturation state is approached for different strains.

The bending moment per unit width of the metallic film is classically given by

$$M = -\int_{-\frac{h}{2}}^{\frac{h}{2}} \sigma_{11} z dz = -2\int_{0}^{\frac{h}{2}} \sigma_{11} z dz \tag{4.5}$$

In the elastic phase of peeling (Path OA in Fig. 4.2), the moment curvature relationship is:

$$M = \frac{EKh^3}{9} \qquad 0 \leq K \leq K_e \tag{4.6}$$

with the elastic limit curvature $K_e = \frac{\sqrt{3}\sigma_0}{Eh}$.

For a ductile thin metallic film, the maximum curvature in point B of Fig. 4.2, K_B, is larger than K_e so plasticity plays an important role and a precise calculation of the dissipation is needed to extract from the measurement of the peel force, the true (or objective as named in Kim and Kim [19]) interface fracture energy Γ. The moment curvature relationship during plastic loading (path AB) is:

$$M = -2\int_0^t \sigma_{11} z dz - 2\int_t^{\frac{h}{2}} \sigma_{11} z dz \tag{4.7}$$

where $t = \frac{\sigma_0\sqrt{3}}{2EK}$ corresponds to the position of the elastic-plastic transition surface when the curvature K is between K_e and K_B. Note that during the plastic loading and due to 2D plane strain, the accumulated strain is $\bar{\varepsilon} = \frac{2}{\sqrt{3}} Kz$. Owing to the behavior (4.2) of the ductile film, the expression (4.7) of the moment becomes:

$$M = \frac{8EKt^3}{9} + \frac{4}{\sqrt{3}}\int_t^{\frac{h}{2}} \left(\alpha - \beta \exp\left(-\frac{2\gamma K z}{\sqrt{3}}\right)\right) z dz \tag{4.8}$$

By integration by parts, the integral term on the right hand side of Eq. (4.8) can be evaluated since:

$$\int_{z_1}^{z_2} z exp(\delta z) dz = F(\delta, z_2) - F(\delta, z_1) \tag{4.9}$$

with the function F defined as $F(\delta, z) = \exp(\delta z)\left(\frac{z}{\delta} - \frac{1}{\delta^2}\right)$. As a consequence, an explicit expression for Eq. (4.8) is found:

$$M = \frac{\alpha h^2}{2\sqrt{3}} + \frac{\sigma_0^2}{E^2K^2}\left(\frac{\sigma_0}{\sqrt{3}} - \frac{\sqrt{3}\alpha}{2}\right) - \frac{4\beta}{\sqrt{3}}\left[F\left(-\frac{2\gamma K}{\sqrt{3}}, \frac{h}{2}\right) - F\left(-\frac{2\gamma K}{\sqrt{3}}, t\right)\right] \tag{4.10}$$

From Eq. (4.2) when the material is elastic-perfectly plastic with $Q = 0$ (i.e. $\alpha = \sigma_0$ and $\beta = 0$), the relationship provided by Aravas et al. [8] and Kim and Kim [19] is recovered.

During the unloading phase, corresponding to path (BC) on Fig. 3.2, $(K_B - K_B^* \leq K \leq K_B)$, the moment is linked to the curvature, as in Kim and Kim [19]:

$$M = M_B + \frac{E}{9}(K - K_B)h^3 \tag{4.11}$$

where $M_B = M(K = K_B)$ given in Eq. (4.10). In the following, we denote $t_B = \frac{\sigma_0\sqrt{3}}{2EK_B}$ the position of the elastic-plastic transition surface when the curvature is maximum, equal to K_B. The unloading phase stops in C when reverse plasticity develops at the outer surface of the film $z = \frac{h}{2}$. Let us denote $K_C = K_B - K_B^* \leq K_B$ the curvature leading to this condition. While in B, the outer surface $z = \frac{h}{2}$ was in

compression, in C the plasticity occurs when the surface is under tension. Following Kim and Aravas [6] or Kinloch et al. [41], the curvature K_C is defined as follows:

$$\frac{2\bar{\sigma}}{\sqrt{3}} = -\frac{2\bar{\sigma}}{\sqrt{3}} + \frac{4E}{3}(K_B - K_C)\frac{h}{2} \tag{4.12}$$

where $\bar{\sigma}$ stands for the yield stress prevailing at $z = \frac{h}{2}$ at the end of plastic bending phase (for $K = K_B$):

$$\bar{\sigma} = \alpha - \beta \exp\left(-\frac{\gamma K_B h}{\sqrt{3}}\right) \tag{4.13}$$

As consequence, $K_C = K_B - K_B^*$ with $K_B^* = \frac{2\sqrt{3}}{Eh}\left(\alpha - \beta \exp\left(-\frac{\gamma K_B h}{\sqrt{3}}\right)\right)$.

For the peel test, the reverse plastic loading, path (CD) on Fig. 4.2, exists since the free arm is pulled into straight plane with a final curvature of K_D close to 0. Let us denote $t'(K)$ the position of the elastic-plastic transition surface during the reverse plastic loading. By construction, t' is larger than t_B, meaning that a material point with $z > t'$ has already faced plasticity during the bending phase up to the curvature K_B. Similarly to Eq. (4.12), an implicit relationship for t' is found:

$$\alpha - \beta \exp\left(-\frac{2\gamma K_B t'}{\sqrt{3}}\right) = \frac{E}{\sqrt{3}}(K_B - K)t' \tag{4.14}$$

In the theory, as discussed by Aravas et al. [8], the reverse plastic loading can continue for negative curvature. During peel test, according to Fig 4.2, such possibility is not considered here. For a given curvature $K_B - K_B^* \geq K \geq 0$, the mechanical state of a material point in the film varies depending on its position. For $0 \leq z \leq t_B$, the material is elastic. For $t_B \leq z \leq t'$, the material is also in the elastic regime but has cumulated some plasticity during the bending stage (AB). Finally, in the third part $t' \leq z \leq \frac{h}{2}$ the material point cumulates reverse plasticity. For the latter part of the film, the accumulated strain is, as given in Kim and Aravas [6] and Kinloch et al. [41]:

$$\bar{\varepsilon} = \frac{2}{\sqrt{3}}\left[(2K_B - K)z - \frac{\sqrt{3}}{E}\left(\alpha - \beta \exp\left(-\frac{2\gamma K_B z}{\sqrt{3}}\right)\right)\right] \tag{4.15}$$

After some calculations, by considering the three strain histories above, the moment can be evaluated in a semi-analytical manner:

$$M = \frac{8EK_B t_B^3}{9} - \frac{8E}{9}(K_B - K)(t')^3 + \frac{2\alpha}{\sqrt{3}}\left(2(t')^2 - t_B^2 - \frac{h^2}{4}\right)$$

$$- \frac{4\beta}{\sqrt{3}}\left[F\left(-\frac{2\gamma K_B}{\sqrt{3}}, t'\right) - F\left(-\frac{2\gamma K_B}{\sqrt{3}}, t_B\right)\right] + \frac{4\beta}{\sqrt{3}}\int_{t'}^{\frac{h}{2}} z exp(-\gamma\bar{\varepsilon}) dz \qquad (4.16)$$

with t' defined in Eq. (4.14) and $\bar{\varepsilon}$ in Eq. (4.15). Note that when the curvature K_B and the parameter γ are large and the ratio $\frac{\sigma_0+Q}{E}$ is small (situation which is observed in peeling of copper film on an elastic substrate), the accumulated strain can be approximated by:

$$\bar{\varepsilon} = \frac{2}{\sqrt{3}}(2K_B - K)z \qquad (4.17)$$

In that case, a closed form expression for M defined in Eq. (4.16) is available. Indeed, the integral term of the right hand side of Eq. (4.16) becomes:

$$\int_{t'}^{\frac{h}{2}} z exp(-\gamma\bar{\varepsilon}) dz = F\left(-\frac{2\gamma(2K_B - K)}{\sqrt{3}}, \frac{h}{2}\right) - F\left(-\frac{2\gamma(2K_B - K)}{\sqrt{3}}, t'\right) \qquad (4.18)$$

The domain of validity of this approximate solution will be discussed in Section 4.3.

Eqs (4.6), (4.10), (4.11) and (4.16) provide the moment curvature expressions for a Voce hardening law. Two limiting cases have been explored in the literature because of the possibility to derive analytical expressions for the moment curvature relation and therefore for the work done by bending plasticity. First, when the material is elastic-perfectly plastic with Q=0 in Eq. (4.2) (i.e $\alpha = \sigma_0$ and $\beta = 0$), the corresponding relationships provided by Aravas et al. [8] and Kim and Kim [19] are recovered. Second, when the parameter γ is small, the Voce hardening law can be replaced by its first order Taylor expansion:

$$\bar{\sigma} = \sigma_0 + Q\gamma(\bar{\varepsilon} - \bar{\varepsilon_0}) \qquad (4.19)$$

After some calculations, it can be shown that the moment curvature expressions derived by Kinloch et al. [41] for bilinear material are also obtained.

As proposed by Kendall [57], Aravas et al. [8] or Wei and Hutchinson [7] among others of the literature, the energy balance provides a link between the peel force per unit width P (see Fig. 4.1), the interface fracture energy Γ and the work done by bending plasticity Ψ:

$$P(1-cos\theta) = \Gamma + \Psi \implies \Gamma = P(1-cos\theta) - \Psi \tag{4.20}$$

Eq. (4.20) is obtained assuming that the change of elastic strain energy due to the extension of the film under the peel force P is negligible. The term Ψ contains the plastic dissipation and the residual strain energy contribution during plastic bending, see Kim and Aravas [6] , Kim et al. [39] or Martiny et al. [9]. As mentioned by Kim and Aravas [6], the work done by bending plasticity Ψ per unit crack advance is $\Psi = \int_L MdK$ where L is the loading path (OABCD) in the moment curvature of Fig. 4.2 :

$$\Psi = \int_0^{K_e} MdK + \int_{K_e}^{K_B} MdK + \int_{K_B}^{K_B - K_B^*} MdK + \int_{K_B - K_B^*}^{0} MdK \tag{4.21}$$

Interestingly, the moment curvature relationship is known for the whole path (OABCD). Owing to the explicit expression on the path (OABC), the first three terms on the right hand side of Eq. (4.21) can be evaluated analytically. More details can be found in Appendix A. Finally, we obtained:

$$\begin{aligned}\Psi = {} & \frac{\sigma_0^2 h}{6E} + \frac{\alpha h^2}{2\sqrt{3}}(K_B - K_e) + \left(\frac{\sigma_0}{\sqrt{3}} - \frac{\alpha\sqrt{3}}{2}\right)\frac{\sigma_0^2}{E^2}\left(\frac{1}{K_e} - \frac{1}{K_B}\right) \\ & - \frac{\beta\sqrt{3}}{\gamma^2}\left[G\left(-\frac{\gamma h}{\sqrt{3}}, K_B\right) - G\left(-\frac{\gamma h}{\sqrt{3}}, K_e\right)\right] \\ & + \frac{\beta\sqrt{3}}{\gamma}\exp\left(-\frac{\gamma\sigma_0}{E}\right)\left(\frac{\sigma_0}{E} + \frac{1}{\gamma}\right)\left(\frac{1}{K_B} - \frac{1}{K_e}\right) - M_B K_B^* + \frac{Eh^3}{18}(K_B^*)^2 \\ & + \left[\frac{8EK_B t_B^3}{9} - \frac{2\alpha}{\sqrt{3}}\left(t_B^2 + \frac{h^2}{4}\right) + \frac{4\beta}{\sqrt{3}}F\left(-\frac{2\gamma K_B}{\sqrt{3}}, t_B\right)\right](K_B^* - K_B) + I\end{aligned} \tag{4.22}$$

where the function $G(x,y)$ is defined as $G(x,y) = \frac{\exp(xy)}{y}$ and I given by:

$$I = \int_{K_B - K_B^*}^{0}\left[\frac{8E}{9}(K - K_B)(t')^3 + \frac{4\alpha}{\sqrt{3}}(t')^2 - \frac{4\beta}{\sqrt{3}}F\left(-\frac{2\gamma K_B}{\sqrt{3}}, t'\right) + \frac{4\beta}{\sqrt{3}}\int_{t'}^{\frac{h}{2}} z exp(-\gamma\bar{\varepsilon})dz\right]dK \tag{4.23}$$

The expression (4.22) is semi-analytical. Based on the present derivation, the work done by bending plasticity has almost a closed form expression except for the last term. Indeed, t' , defined by the implicit relationship (4.14) is function of the current curvature K. Nevertheless, when the radius of curvature is small (K_B large) and the parameter γ has an important value, the expression for the accumulated strain

(4.15) is given by Eq. (4.17). In addition we propose to define t' of Eq. (4.14) by $t' = \frac{\alpha\sqrt{3}}{E(K_B - K)}$. Based on these two assumptions, the last integral term I can be evaluated in closed form:

$$I^{approx} = \frac{4\alpha^3}{E^2\sqrt{3}}\left(\frac{1}{K_B} - \frac{1}{K_B^*}\right) - \frac{\beta\sqrt{3}}{\gamma^2}\left(G\left(-\frac{\gamma h}{\sqrt{3}}, 2K_B\right) - G\left(-\frac{\gamma h}{\sqrt{3}}, K_B + K_B^*\right)\right) + \frac{\beta\sqrt{3}}{K_B\gamma^2}\left(G\left(-\frac{2\gamma\alpha}{E}, \frac{K_B}{K_B^*}\right) - G\left(-\frac{2\gamma\alpha}{E}, 1\right) + G\left(-\frac{2\gamma\alpha}{E}, \frac{K_B + K_B^*}{K_B^*}\right) - G\left(-\frac{2\gamma\alpha}{E}, 2\right)\right) \tag{4.24}$$

The present approach leading to the dissipation contains by construction the elastic-perfectly plastic case. Indeed, when the parameter Q of Eq. (4.2) is set to zero, the material is obviously elastic-perfectly plastic. In that case, since $\alpha = \sigma_0$, one obtains $K_B^* = 2K_e$, $t_B = \frac{\sigma_0\sqrt{3}}{2EK_B}$. It is easily shown that the expression of Ψ is identical to the expression provided by Aravas et al. [8] or Kim and Kim [19] for an elastic-perfectly plastic material:

$$\Psi^{PP} = M_0 K_e\left(2\frac{K_B}{K_e} - 5 + \frac{10}{3}\frac{K_e}{K_B}\right) \quad \text{when } K_B \geq 2K_e \tag{4.25}$$

where $M_0 = \frac{1}{2\sqrt{3}}\sigma_0 h^2$ is the fully plastic moment. As discussed previously, the present approach also contains the bilinear response for an elastic-plastic material proposed by Kinloch et al. [41] or Moidu et al. [58] when the parameter γ is small.

When γ is large, the saturation of the yield stress occurs at small strain. Therefore, it can be argued that the material is almost elastic-perfectly plastic with the yield stress being equal to the saturation stress $Q + \sigma_0$ (this hypothesis was adopted by Song and Yu (2002) [29]). This case will be discussed in Section 4.3. One can also mention that the extension of the present approach to a constitutive behavior containing a finite number of Voce law:

$$\bar{\sigma} = \sigma_0 + \sum_{i=1}^{N} Q_i\left(1 - \exp\left(-\gamma_i(\bar{\varepsilon} - \varepsilon_0)\right)\right) \tag{4.26}$$

is straightforward. This can be done by imposing $\alpha = \sigma_0 + \sum_{i=1}^{N} Q_i$, and replacing β by $\beta_i = Q_i \exp(\gamma_i \varepsilon_0)$ and γ by γ_i.

4.3 Results

This section is devoted to the evaluation of the moment curvature response of a thin film under bending/reverse bending. The difference between the present development based on a Voce law with the one of Kim and Kim [19] for elastic-perfectly plastic response is illustrated.

The effect of the parameter γ of Eq. (4.2) on the elastic-plastic response of the metallic film is first investigated in Fig. 4.3. The reference parameters for the elastic plastic behavior of the film are listed in Table 4.1. The parameter γ influences the deformation level for which the flow stress approaches the plateau $\sigma_0 + Q$. Indeed for a small value of γ (here γ = 5), a large strain is needed to reach the saturation regime (around $\bar{\varepsilon} = 1$), while for large value of γ (here γ = 160), a small strain is suffisant for the yield stress to reach the plateau (around $\bar{\varepsilon} = 0.03$). The initial plastic hardening modulus $\frac{\partial \bar{\sigma}}{\partial \bar{\varepsilon}}(\bar{\varepsilon} = \varepsilon_0)$ is highly affected by the value of γ. For a metal, it must be smaller than the elastic Young's modulus, leading to the condition for γ: $\gamma \leq \frac{E}{Q}$. With the present material parameters of Table 4.1, one obtains: $\gamma_{lim} = 361$.

h μm	E GPa	ν	σ_0 MPa	Q MPa	γ
35	65	0.26	100	180	$[5, 160]$

Table 4.1 : Reference parameters for the elastic-plastic behavior of the metallic film and for the cohesive law.

It is also interesting to observe the difference between the moment curvature evolution predicted by adopting a Voce hardening law and by assuming that the material is elastic-perfectly plastic. For illustration, in Fig. 4.4, the curvature for the metallic film is $K_B = 4000m^{-1}$, leading to a corresponding radius close to 0.25mm. The film thickness is $h = 35\mu m$. Two elastic-perfectly plastic cases are considered. The first one assumes that the yield stress of the material is $\bar{\sigma} = \sigma_0$ while in the second case

$\bar{\sigma} = \sigma_0 + Q$. As expected, the response based on the Voce law is located between the two curves corresponding to elastic-perfectly plastic materials. Since the work done by bending plasticity Ψ is the area formed by the curve along the path (OABCD), it is clear that assuming an elastic-perfectly plastic behavior for the material is only valid for very large values of γ. It is interesting to notice that due to strain hardening, the moment curvature response during the reverse bending (path CD of Fig. 4.2) for $\gamma = 160$ corresponds to the response of an elastic-perfectly plastic material with $\bar{\sigma} = \sigma_0 + Q$. Nevertheless, during the bending (path AB of Fig. 4.2), some difference exists which affects the work Ψ. On the contrary, for $\gamma = 40$, the work done by bending plasticity is strongly overestimated by assuming an elastic-perfectly plastic response $\bar{\sigma} = \sigma_0 + Q$. Fig. 4.5 displays the evolution of Ψ as γ is enlarged, keeping $K_B = 4000m^{-1}$. It is observed that Ψ is increasing rapidly for small values of γ. Indeed as γ becomes larger, the response of the material becomes close to an elastic-perfectly plastic response, see Fig 4.3. As a consequence, the value of Ψ saturates, reaching the value Ψ^{PP}, predicted by the elastic-perfectly plastic approach of Aravas et al. [8], or Kim and Kim [19]. These trends are confirmed for two values of Q: $Q = 90$ or 180 MPa.

For material parameters of Table 4.1 and two values of γ : 40 and 160, the work done by bending plasticity evaluated based on Eqs. (4.22) and (4.23) is presented in Fig. 4.6 for a curvature K in the range $1000m^{-1}$ to $10000m^{-1}$ leading to a radius of the film varying from 100μm to 1mm. As expected, Ψ is larger when the normalized curvature is increased. For large value of the normalized curvature, the response is seen to be almost linear for both values of γ. This could have been anticipated. Indeed, Fig. 4.4 has shown that for large γ, the moment versus curvature response is quite similar to the one estimated based on an elastic-perfectly plastic approach. Therefore, in that case, the work Ψ for a Voce law or an elastic-perfectly plastic material (with $\bar{\sigma} = \sigma_0 + Q$) must be quite similar. From Eq. (4.25) the increment of work $\Delta\Psi$ produced by an increment of the normalized curvature $\frac{\Delta K}{K_e}$ is expressed as follows, when $\frac{K}{K_e}$ is large:

$$\Delta\Psi = 2M_0\Delta K \tag{4.27}$$

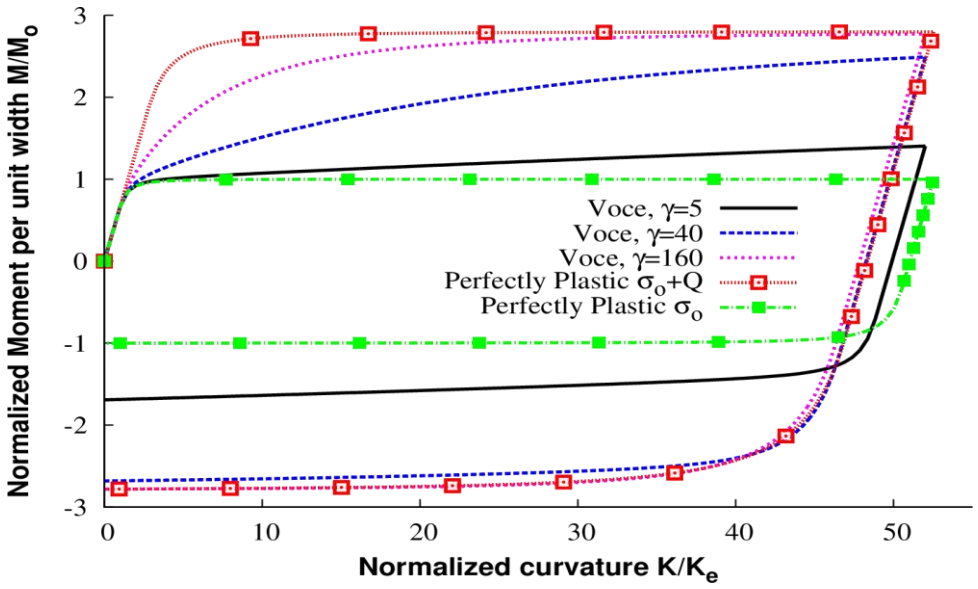

Figure 4.4: Estimated moment curvature relationship for an elastic-perfectly plastic material and a material with a Voce yield stress. Effect of the parameter γ controlling the deformation for which the flow stress saturates, see Eq. (4.2). The reference material parameters are listed in Table 4.1. M_0 is the fully plastic moment. K_e is the elastic limit curvature.

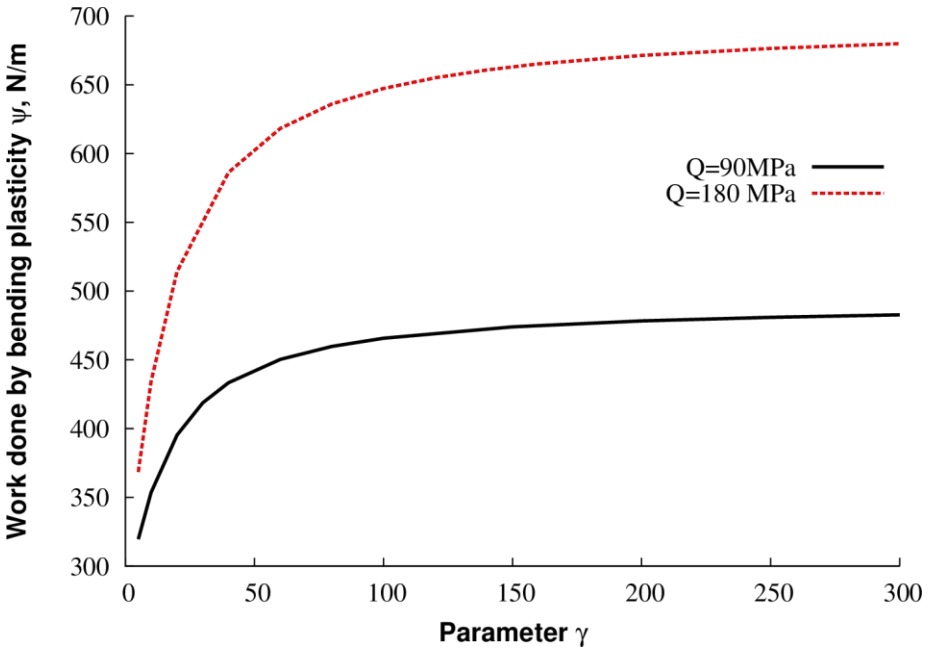

Figure 4.5: Work done by bending plasticity as a function of γ for two values of Q: $Q = 90$ MPa and $Q = 180$ MPa. The reference material parameters are listed in Table 4.1.

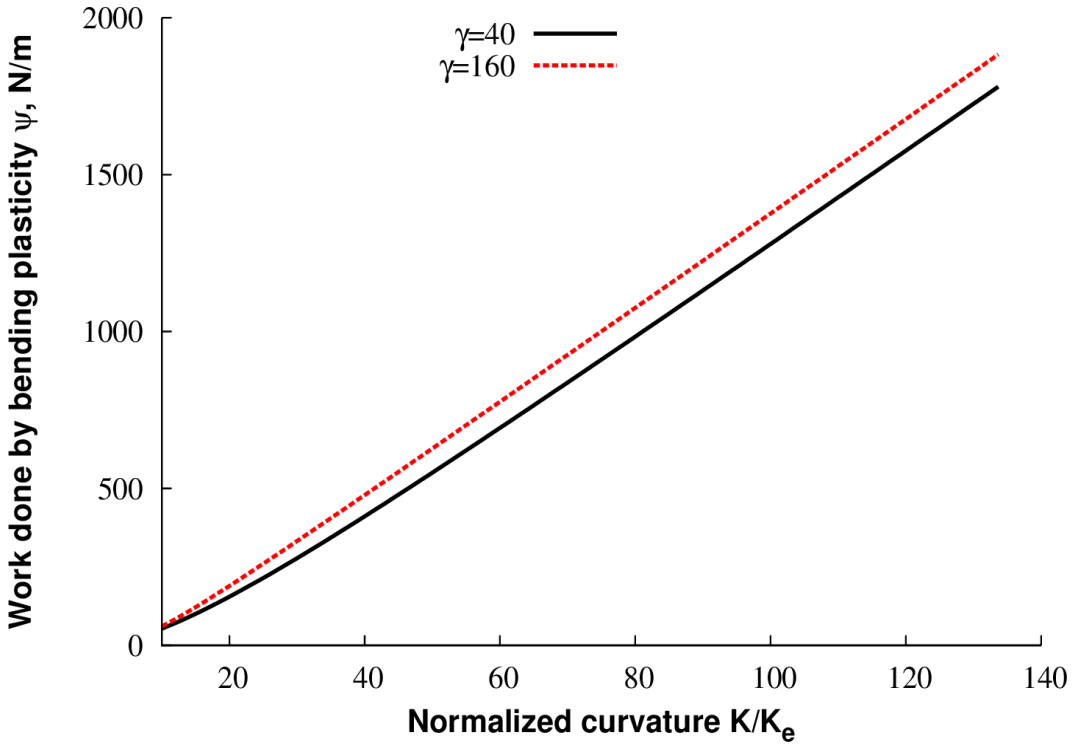

Figure 4.6: Work done by bending plasticity Ψ versus normalized curvature $\frac{K}{K_e}$ during bending and reverse bending for two values of γ : $\gamma = 40$ and $\gamma = 160$.

With the parameters of Table 4.1, we find that $\Delta\Psi \approx 15\frac{\Delta K}{K_e}$. This is consistent with the observation of Fig. 4.6. In addition, for the two values $\gamma = 40$ and $\gamma = 160$, we have seen that the approximate work done by bending plasticity Ψ based on Eq. (4.24) almost coincides with the one obtained with Eq. (4.22) (results not presented here).

Next, a more precise comparison between the predicted work done by bending plasticity Ψ evaluated using the Voce law or an elastic-perfectly plastic response (Ψ^{PP} with $\bar{\sigma} = \sigma_0 + Q$) is presented in Fig. 4.7. For the value $\gamma = 40$, the normalized ratio $\frac{\Psi}{\Psi^{PP}}$ is still below 0.9 when the normalized curvature $\frac{K}{K_e}$ is equal to 88 ($K = 6676m^{-1}$ or a radius around 149μm). Adopting an elastic-perfectly plastic approximation for this material when analyzing results of peel tests will lead to a 10% difference in the interface fracture energy Γ, see the energy balance Eq. (4.20) for a test at $\theta = 90°$. When $\gamma = 160$, we clearly observe that for $\frac{K}{K_e}$= 88, less than 3% difference remains. Note that Fig. 4.4 is constructed with a

value of the curvature of $K_B = 4000m^{-1}$ ($\frac{K_B}{K_e} = 52$). In that case, a difference of 15% exists between Ψ based on expression (4.22) and Ψ^{PP} for $\gamma = 40$ while for $\gamma = 160$, the difference reduces to 4%.

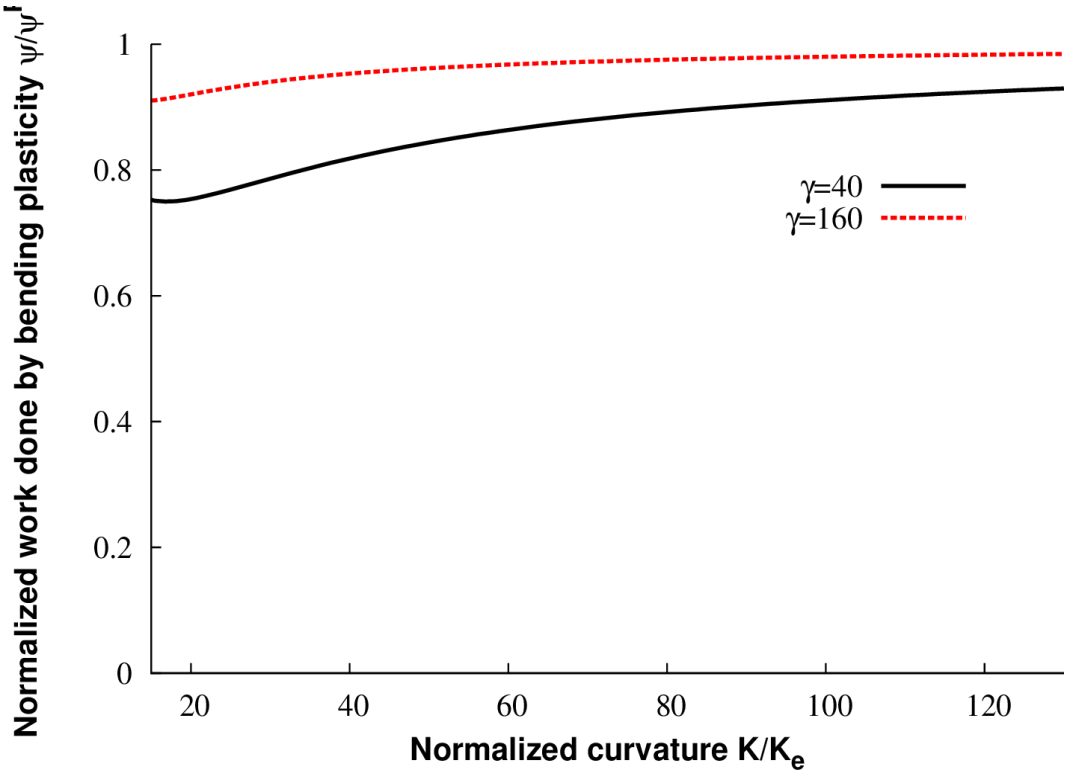

Figure 4.7 Ratio $\frac{\Psi}{\Psi^{PP}}$ between the work done by bending plasticity Ψ evaluated based on a Voce flow stress and an elastic-perfectly plastic response. Material parameters for the Voce law are given in Table 4.1.

4.4 Conclusion

The estimation of the work done by bending plasticity during bending/reverse bending for a Voce type behavior is the main goal of the present chapter. A semi-analytical expression for the work done by bending plasticity is derived for a material presenting a Voce hardening law. The proposed expression contains two situations addressed in the literature where the film has an elastic-perfectly plastic behavior, Kim and Kim [19] or a bilinear response, Kinloch et al. [41]. The work done by bending plasticity is highly sensitive to the film curvature. As proposed previously in the literature for other

material constitutive laws, the knowledge of this work enables to extract the interface fracture energy from the peel force measurement. It is also observed that depending on the material parameters, the elastic-perfectly plastic approach proposed by Kim and Kim [19], Aravas et al. [8] can also be justified even for a Voce type material when the saturation of the flow stress is observed for limited strain. In the next section, by comparison with finite element calculations performed for various angles in the range [45°, 135°], it will be found that the present theory is accurate to analyze peel test for $\theta = 90°$ and provide a satisfactory estimate for other peel angles (see chapter 5).

5 NUMERICAL MODELING OF PEELING

5.1 Introduction

Numerical analysis using finite element analysis software (ABAQUS/standard) has been carried out to simulate peeling of copper film on composite substrate. A two-dimensional model is built. The entire assembly consists of two parts: the elastic composite substrate and an elastic-plastic deformable copper film. Cohesive elements are implemented at the interface between the copper and the composite substrate, to reproduce interfacial failure. The goal of the finite element simulations is to provide values of the peel force and the curvature, in close agreement with experimental works. Therefore, the parameters of the cohesive response will be identified and the interface fracture energy captured.

In this chapter first, the geometry of the peeling model and the behavior of the cohesive elements are defined. Next, we perform a parametric study on a reference configuration. These simulations will help to understand how model parameters (material parameters, cohesive law parameters) influence both the peel force and the associated curvature. Finally, a comparison between the experimental and numerical results is presented**.**

5.2 Geometric configuration of peel test and cohesive elements

5.2.1 Position of the problem

A two-dimensional plane strain model of peeling is developed for various peel angles θ in the range [45°- 135°]. The geometry and boundary conditions of the numerical model are shown in Fig. 5.1. To describe the delamination behavior of the interface, cohesive zone model is used. The interface between the copper film and the composite substrate is modeled by cohesive elements (COH2D4 in ABAQUS 6.14) with a small thickness (0.005 mm). The behavior of cohesive elements is characterized by a traction-separation law. Tie constraints are used to connect the cohesive elements to the copper film and composite substrate. The element types used in all models are 4-node elements with linear interpolation.

Plane strain elements (CPE4R) are adopted to mesh the film thickness with 9 elements in the thickness for $\theta < 90°$. In this case, the element size is 12*4 microns (when h=35µm). For $\theta > 90°$, 18 elements in the film thickness are considered since the curvature is smaller (sometimes around 100µm for θ = 135°). Thus, the element size is 6*2 microns. A mesh sensitivity study has been carried out by considering larger mesh density. By increasing the number of elements, and therefore by reducing the element size, the predictions in terms of peel force and curvature are preserved. The cohesive element size in the 1 direction (see Fig. 5.1) is five times smaller than the element size in the film. In all calculations, the magnitude of the velocity for the peel arm is V = 0.5mm/s. To ensure that the peel angle θ remains constant during the FE simulation, the substrate is moving in the horizontal direction with the same velocity V = 0.5mm/s. The length of the model is 100 mm long. It has been checked that this length is sufficient so that a stationary process prevails after a short period of time.

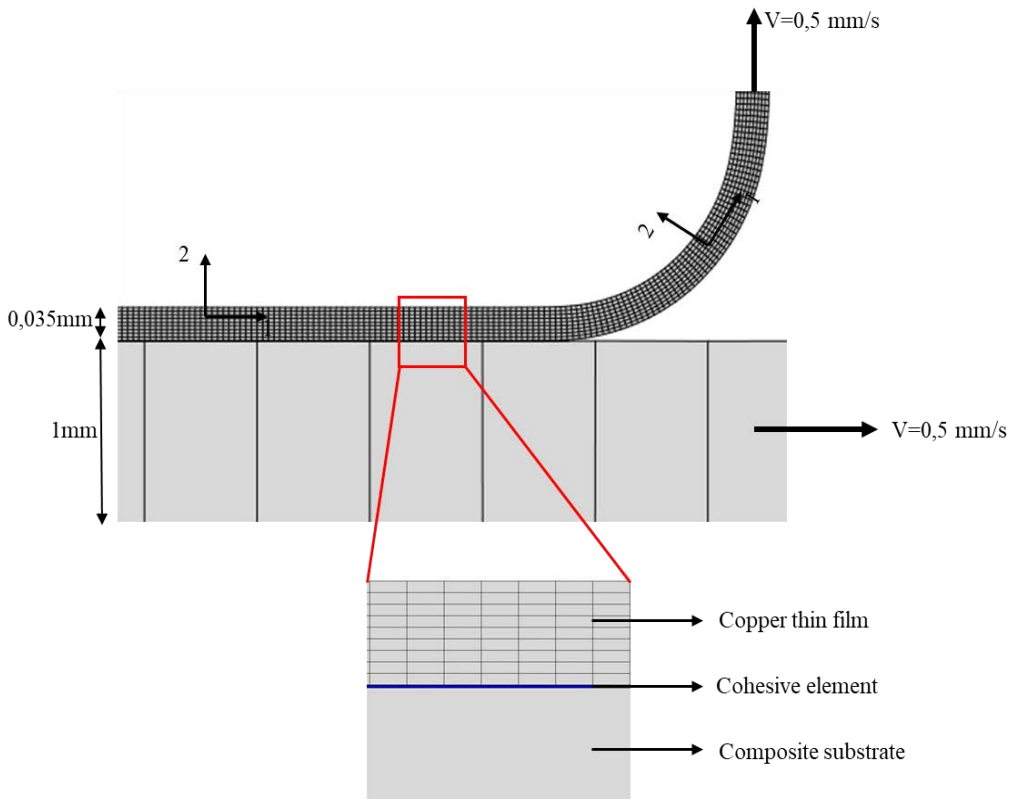

Figure 5.1: The geometry and the boundary conditions of the finite element model used for the simulation of the peel test.

5.2.2 Cohesive behavior

An accurate definition of the interface mechanical properties between the film and the substrate is important for the prediction of the peel test response. To model the interface between two materials in numerical simulations, cohesive elements are used. In Abaqus standard, modeling of progressive damage and failure in a cohesive layer is possible via the definition of a traction separation law, see Camanho and Davila [59]. Three ingredients are needed: a damage initiation criterion, a damage evolution law and failure criterion. Fig. 5.2 shows a typical bilinear traction-separation response in pure mode I. When the critical stress is overcome ($\sigma_n > \sigma_{n,c}$), the stiffness of the element is reduced. The damage evolution law describes the rate at which the material stiffness is degraded once the corresponding initiation criterion is reached. Owing to Camanho and Davila [59], the damage parameter in Mode I is:

$$d = \frac{\delta_{n,f}(\delta_n^{max} - \delta_{n,c})}{\delta_n^{max}(\delta_{n,f} - \delta_{n,c})} \tag{5.1}$$

Unloading could occur therefore according to the dashed line. Two parameters are important for the definition of the evolution of damage. The first one is the displacement at complete failure, $\delta_{n,f}$ while the second is the displacement at the initiation of damage, $\delta_{n,c}$ see Fig. 5.2. The fracture energy is equal to the area under the traction-separation curve (see Fig. 5.2). Element deletion occurs when $d = 1$, i.e in Mode I, when $\delta_n^{max} = \delta_{n,f}$.

This above description is valid for pure Mode I. In mixed mode, a coupling between the traction and shear is needed. The nominal traction vector (or stresses) is related to the nominal displacement (or strain). In mixed mode (2D FE model) the nominal traction vector, t, consists of two components: the normal stress σ_n and the shear stress σ_t. The corresponding displacements are denoted by: δ_n and δ_t in a two-dimensional problem. The nominal strains can be defined by the following relation:

$$\varepsilon_n = \frac{\delta_n}{t_0} \tag{5.2}$$

$$\varepsilon_t = \frac{\delta_t}{t_0} \tag{5.3}$$

where t_0 is the initial thickness of the cohesive element.

Before damage initiation, a linear response is proposed:

$$\begin{Bmatrix} \sigma_n \\ \sigma_t \end{Bmatrix} = \begin{bmatrix} K_{nn} & 0 \\ 0 & K_{tt} \end{bmatrix} \begin{Bmatrix} \delta_n \\ \delta_t \end{Bmatrix} \tag{5.4}$$

where K_{nn}, K_{tt} being penalty stiffnesses**.**

Damage initiation criterion controls the onset of the delamination process at a material point. We adopt a quadratic nominal stress criterion (QUADS in Abaqus):

$$\left(\frac{< \sigma_n >}{\sigma_{n,c}}\right)^2 + \left(\frac{\sigma_t}{\sigma_{t,c}}\right)^2 = 1 \tag{5.5}$$

Where $<.>$ is the Macaulay bracket. Concerning the fracture damage criterion, we states that failure under mixed-mode condition is governed by a power law interaction of the energies required to cause failure for the individual (normal and shear) modes. It is given by:

$$\left(\frac{G_n}{\Gamma_I}\right)^\beta + \left(\frac{G_t}{\Gamma_{II}}\right)^\beta = 1 \tag{5.6}$$

Where $G_n = \int \sigma_n d\delta_n$ and $G_t = \int \sigma_t d\delta_t$ are respectively the dissipation energy under normal and shear mode. Γ_I (resp. Γ_{II}) is the mode I toughness (resp Mode II toughness). In our approach we adopt $\beta = 1$.

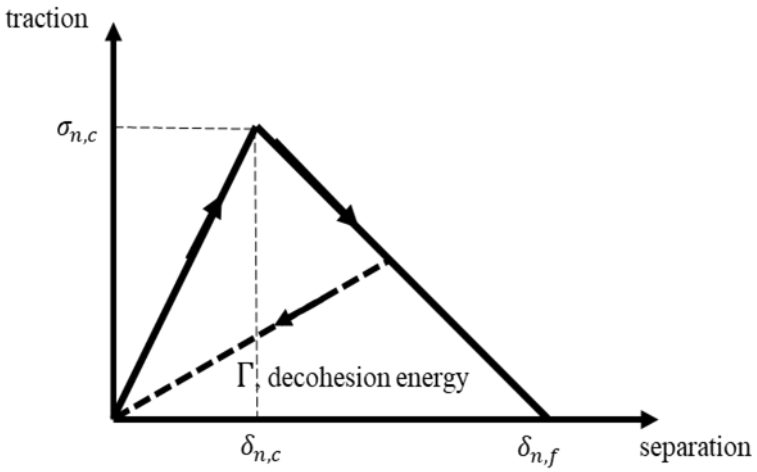

Figure 5.2: Bilinear traction separation law for pure traction mode.

To calibrate the behavior of the cohesive interface, ten parameters are needed: K_{nn}, K_{tt}, $\delta_{n,c}$, $\delta_{t,c}$, $\sigma_{n,c}$, $\sigma_{t,c}$, $\delta_{n,f}$, $\delta_{t,f}$, Γ_I, Γ_{II}. Nevertheless owing to links between some above quantities ($\sigma_{n,c} = K_{nn}\delta_{n,c}$, $\sigma_{t,c} = K_{tt}\delta_{t,c}$, $\Gamma_I = \frac{1}{2}\sigma_{n,c}\delta_{n,f}$, $\Gamma_{II} = \frac{1}{2}\sigma_{t,c}\delta_{t,f}$). Six (6) parameters are independent. From the literature review, it has been shown that in most situations, the penalty stiffness, maximum stress and fracture energy for both normal and shear modes are prescribed to be equal: $\Gamma_I = \Gamma_{II} = \Gamma$, $\sigma_{n,c} = \sigma_{t,c} = \hat{\sigma}$. In our work the penalty stiffness is chosen large. We adopt $K_{nn} = K_{tt} = K = 10^6 N/mm^3$. With the present model, the fracture energy is $G_n + G_t = \Gamma$.

As seen in most of the papers of the literature, only two parameters are kept for the definition of the cohesive law: $\boldsymbol{\Gamma}$ and $\hat{\boldsymbol{\sigma}}$.

The elastic behavior of the composite substrate is orthotropic (see chapter 3) (it is assumed that the composite substrate will deform in the elastic range). The elastic behavior of copper is isotropic and a J_2 flow law for the plastic response is adopted. Next in section 5.3 a Voce isotropic hardening law (4.2) will be considered while in section 5.4, the plastic behavior of copper identified based on an uniaxial tensile test will be adopted**.**

5.3 Material response based on a Voce hardening law

In this part, the substrate is representative of laminate (glass fibers with epoxy resin) used in PCB industry. The orthotropic behavior has been identified based on the work of Girard et al [53]. The elastic

moduli are given in Table 3.1 of chapter 3. For metallic film (representative of copper), the thickness is 35µm and the elastic behavior is assumed isotropic with E=65 GPa and $\nu = 0.26$ (value taken from the literature). It is assumed that the copper presents a hardening behavior which can be modeled by a Voce law, Eq. (4.2). The reference material parameters for the Voce law are:

$\sigma_0 = 100MPa$, Q= *90 MPa*, *180 MPa* and γ in the range $[5; 160]$. Note that material parameters are adopted for illustration purpose, real data will be adopted in section 5.4.

First we present a comparison of the model capability based on a peel test with θ = 90°. This working condition is the most often used in the literature and for practical applications. For instance, a peel test at θ = 90° is recommended for the printed circuit board industry to evaluate the interface strength, see the IPC-TM-650 2.4.8 standard. The fracture energy is set to Γ = 1055N/m (or J/m^2) with $\hat{\sigma} = 10$MPa. The force versus time is presented in Fig. 5.3 for three values of γ: 5; 40 and 160 and for two values of Q: 90 and 180MPa. A stationary process for the peel force is established after 3s. We clearly observe that for the same interface fracture energy Γ = 1055N/m (or J/m^2), the force is larger when γ increases. Indeed, for Q = 180MPa, the level of the force is evolving from 1531N/m with γ = 5 to 1707N/m for γ = 160. As Q is larger, meaning that the plateau value for the yield stress is larger, the peel force is also enhanced significantly for large values of γ. Remember that as γ is large, the saturation stress is reached for lower strain, see Fig. 4.3. From the energy balance Eq. (4.21) and since Γ is fixed, the enhancement of the force means that the work done by bending plasticity is larger. A key factor controlling the work done by bending plasticity Ψ is the maximum curvature K_B, existing at the end of the loading path (AB), see Fig. 4.2. During the stationary process in the FE simulations, the radius of curvature R of the top surface $Z = h/2$ can be measured, see Fig. 5.4 where a zoom of the area where the thin film is detached from the substrate is presented. It is observed in this figure, that in the case of a peel test with an angle of θ = 90°, the film is curved with a radius R, which is assumed to be representative of the curvature at point B of Fig. 4.2. To be consistent with the beam bending model where the curvature is measured from the central surface of the film, the curvature K_B is related to R by $K_B = \frac{1}{R+h/2}$.

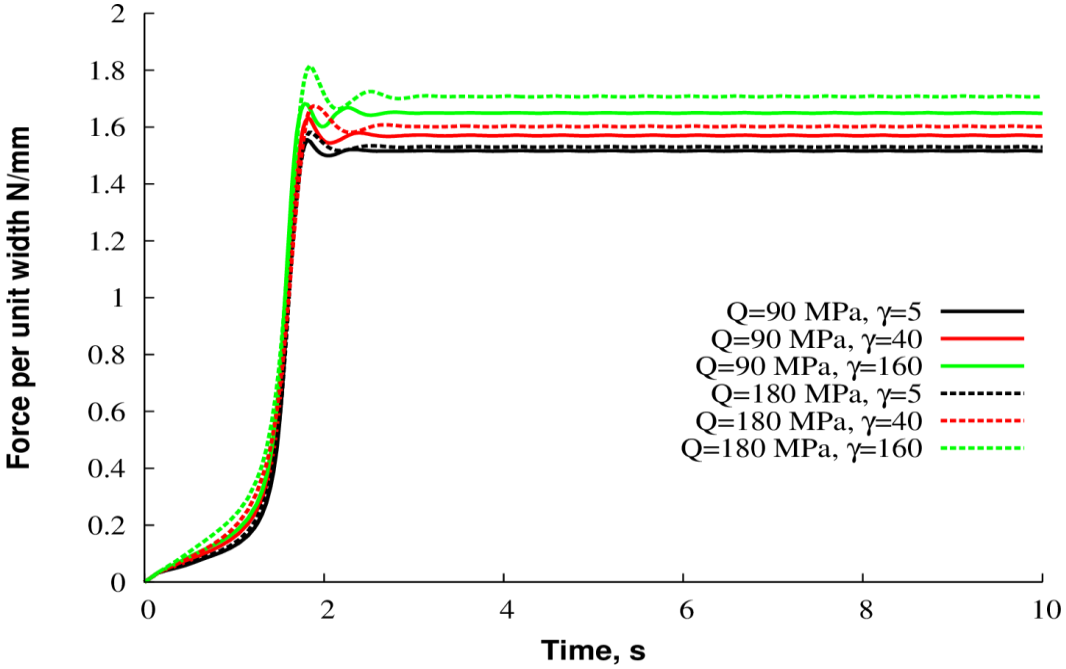

Figure 5.3: Peel force per unit width versus time for different values of material parameters Q and γ. The peel angle is 90°. Other material parameters are presented in Table 4.1.

Fig. 5.5 presents the corresponding evolution of the curvature versus γ for the two different values of Q. The evolution of the curvature versus γ is not monotonic. For moderature values of γ, K_B is first decreasing. Then K_B reaches a minimum value and then subsequently increases slightly as γ becomes larger. Note also that depending on the respective value of Q which is scaling the saturation of the flow stress, the minimum of the curve is reached for larger γ value as Q is larger. The non-monotonic trend can be understood as follows. On the one hand, from Fig. 5.3, it is seen that when γ is increasing from 5 to 40, the level of the force is slightly increased. From the energy balance, the larger force level is linked to an increase in work done by bending plasticity. Nevertheless, in Fig. 4.5 it has been shown that, when γ is increasing from 5 to 40, the work done by bending plasticity is enhanced, for a fixed curvature. As a consequence, to preserve the energy balance and the slight increase of the force, the curvature is reduced so as to propose a moderate increase in plastic dissipation. On the other hand, when γ is large, the work done by bending plasticity saturates when assuming that the curvature remains constant, see Fig. 4.5. Therefore, the larger peel force observed for γ=160 when compared to γ = 40 originates from the increase of the curvature, which produces larger dissipation.

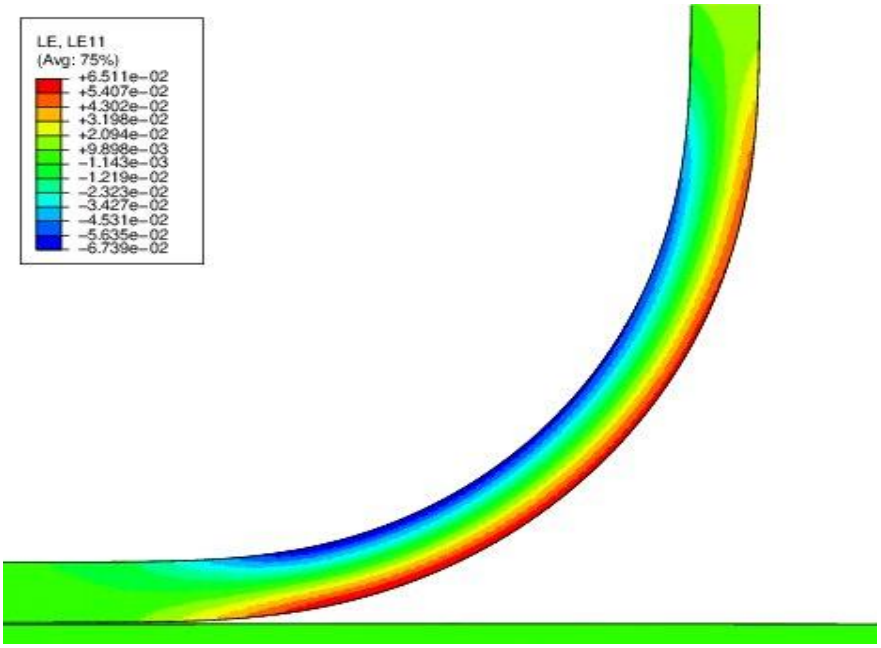

Figure 5.4: View of the film curvature during the bending/reverse bending process. The cohesive elements are removed for presentation purpose. The longitudinal strain ε_{11} is displayed. A local orientation is adopted. Thus, the direction 1 is always parallel to the central surface, as presented in Fig. 5.1.

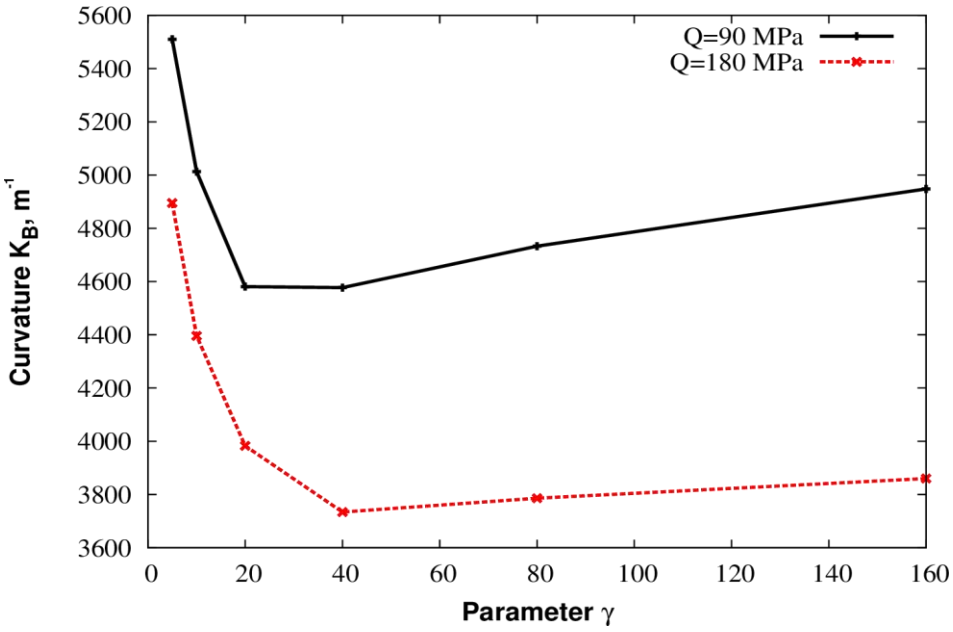

Figure 5.5: Effect of the γ parameter of Eq. (4.2) on the curvature K_B of the film during a peel test at θ = 90°. The ductile film behavior is elastic-plastic with a yield stress described by a Voce law Eq. (4.2).

The prediction of the work done by bending plasticity can be obtained via Eq. (4.22) based on the curvature K_B captured by the finite element calculation (Fig. 5.5). In addition, from the numerical measurement of the peel force, and from Eq. (4.20), the interface fracture energy is estimated. The result of the dialog between the present model and the finite element calculation is illustrated in Table 5.1. We collect in this table three predictions for Γ based, first on the estimate of Ψ provided by the current approach Eq. (4.22), second, based on Eq. (4.24) and third one, based on the elastic-perfectly plastic assumption for the film behavior, Eq. (4.25). The obtained values are compared to Γ = 1055N/m, which is the prescribed value in the finite element simulations. All the results concern a peel test at an angle θ = 90°. Our present approach is able to predict the Γ value with less than 1.5% in the whole range of γ for the two considered cases Q = 90MPa and Q = 180MPa, see Table 5.1. As expected, adopting the formula (4.25) proposed by Aravas et al. [8] is only valid when γ is larger than 40. In that case, the stress-strain response in tension is quite similar to the one expected when the material is elastic-perfectly plastic, see Fig. 4.3. Note also that estimation of the interface fracture energy based on the approximate solution Eq. (4.24) is also accurate for the values of the γ parameter considered in the present section. This observation confirms a previous finding where very limited difference is observed between predictions of the interface fracture energy based on Eqs (4.22) and (4.24), see results of Figs. 4.6 and 4.7.

Fig. 5.6 presents the time evolution for the axial strain component ε_{11} for material points located on the upper part (z = 16.6, 14.6 and 12.6μm) and on the lower part (z = −16.6, −14.6 and −12.6μm) of the film cross-section. As expected, the points located at the lower (resp. upper) part of the film z < 0 (resp. z > 0) experience positive (resp. negative) axial strain ε_{11}. The maximum strain is reached when the curvature is maximum, loading condition B of Fig. 4.2. During the unloading stage (BC) see Fig. 4.2, the strain is slightly decreasing while in the reverse bending phase (CD), the strain magnitude is strongly reduced. Nevertheless, due to plasticity development and the presence of the peel force, a residual strain still exists in the peel arm. The residual strain is homogeneous in the thickness, meaning that the curvature is close to K_D = 0 (straight arm at the end). It is also interesting to mention that for the condition presented here (θ = 90°), the strain profile in the thickness is almost skew-symmetric. This is in close agreement with the bending theory of the beam which is based on the assumption that any material point

entering into the process zone will experience pure bending /reverse bending $\varepsilon_{11} = -Kz$. Fig. 5.7 presents the strain development inside the film thickness at the exact end of the bending process. Since K_B can be evaluated from the finite element simulations, the theoretical predictions of the strain $\varepsilon_{11} = -K_B z$ is also added to the FE strains. We observe that for a peel angle of θ = 90° where K_B = 3759m^{-1} (R = 248μm), a very good agreement exists between the theory and the FE results. A similar comparison is made for two other angles: θ = 60° and θ = 135°. For θ = 135°, it is seen that the strain distribution is nonlinear, with a larger absolute value of the strain at the bottom surface when compared to the top surface. In that configuration, the curvature is K_B = 6468m^{-1} corresponding to a radius of R = 137μm. It will be shown next that the limited correlation of the present theory in reproducing the expected value of the interface fracture energy is partially due to the observed small radius. This conclusion was already drawn in Aravas et al. [8]. Indeed, the plane strain bending approach is considered by Hill [60] as a good approximation assuming that the minimum radius is larger than four to five times the film thickness. With h = 35μm and θ = 135°, R is smaller than 4h. For θ = 60°, the measured value of curvature obtained by FE simulations is K_B = 2434m^{-1} (R = 393μm). It is observed in Fig. 5.7, that the axial strain ε_{11} vanishes for z = 5μm in the FE calculation while in the theory of pure bending, the condition is fulfilled for the central surface (z = 0). This FE result ($\varepsilon_{11} = 0$ for $z \neq 0$) observed mostly for $\theta < 90°$ is due to the fact that instead of pure bending, a more complex loading path prevails with bending and extension. For $\theta < 90°$, the peel force is significantly larger than for $\theta > 90°$, see Rivlin [3] or Williams and Kauzlarich [10].

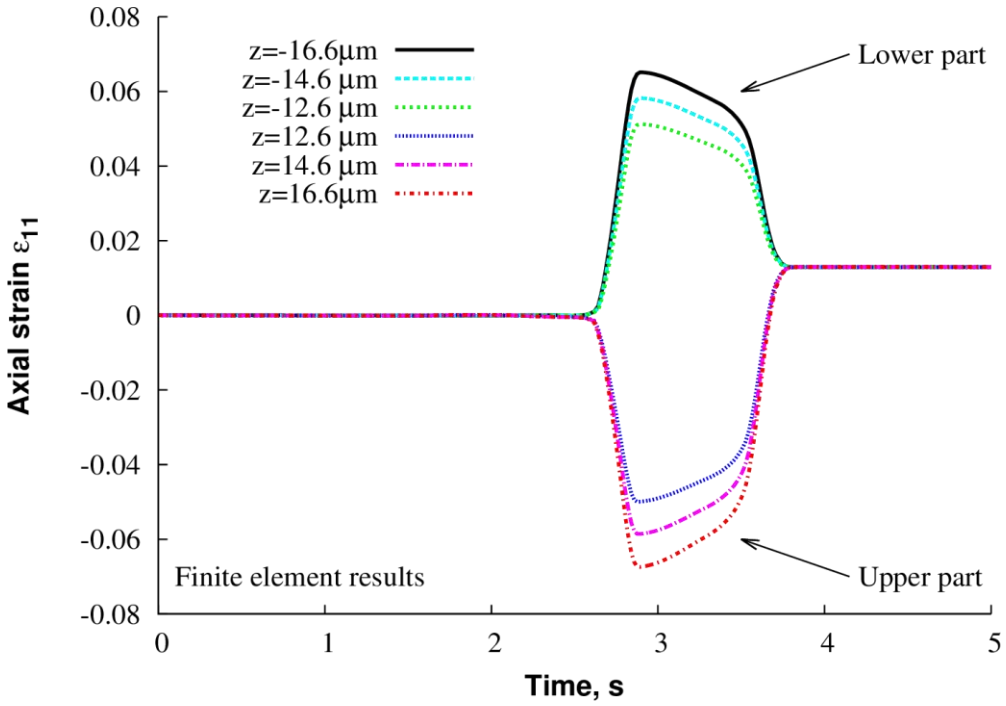

Figure 5.6: Time evolution of ε_{11} within the film thickness for the peel angle θ = 90°.

Estimated Γ (N/m) for Q= 90MPa

γ	5	10	20	40	80	160
Γ from Eq. 4.22	1056	1053	1050	1054	1046	1044
Γ from Eq. 4.24	1051	1050	1048	1053	1045	1043
Γ^{PP} Eq. 4.25	831	891	946	995	1014	1028

Estimated Γ (N/m) for Q= 180MPa

γ	5	10	20	40	80	160
Γ from Eq. 4.22	1052	1047	1050	1058	1069	1066
Γ from Eq. 4.24	1031	1035	1044	1055	1060	1066
Γ^{PP} Eq. 4.25	662	769	873	956	1007	1041

Table 5.1: Predicted interface fracture energy. From the force and curvature measured owing to finite element simulations (here Γ = 1055N/m, θ = 90°), the work done by bending plasticity is evaluated based on the present approach (4.22), the approximate solution (4.24) and the elastic-perfectly plastic approach of Aravas et al. (1989) Eq. (4.25). From the energy conservation (4.20), the interface fracture energy is estimated.

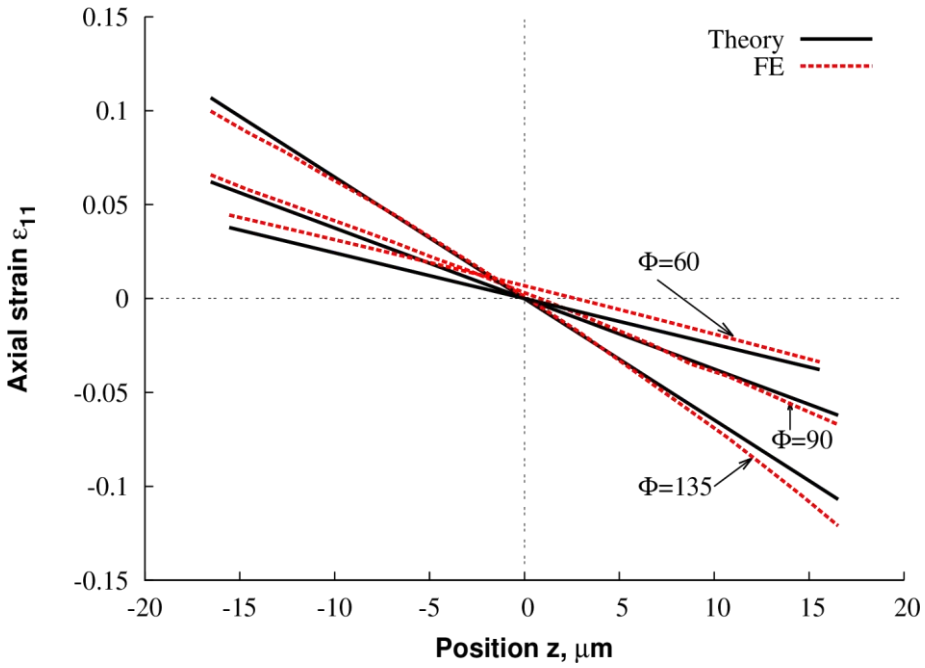

Figure 5.7: Maximum through thickness longitudinal strain captured by the finite element calculations. Comparison with the bending approach for three peel angles: 60°, 90° and 135°. Material parameters are those of Table 4.1 with γ = 40.

Fig. 5.8 presents the stress-strain loading path faced by six material points defined in Fig. 5.6 during the peeling process and for two angles: θ = 90° and θ = 135°. The loading stages (OABCD) of Fig. 4.2 are also added in Fig. 5.8 (a). Material parameters are listed in Table 4.1 with γ = 40. Fig. 5.8 (a), shows that for θ = 90°, the assumption of pure bending/reserve bending is mostly satisfied. During the loading path (OAB), the trajectory of all points in the stress-strain plane is identical up to a maximum strain $\varepsilon_{11}^{max} = -K_B z$. For material points located close to the external surface of the film, the accumulated strain $\bar{\varepsilon}$ up to B is large enough so that the yield stress is close to its saturation value $\sigma_0 + Q$. Therefore, during the reverse bending process (CD), the stress level remains almost constant. In that stage, the material behavior can be approximated by an elastic-perfectly plastic response. For θ = 135° (see Fig. 5.8 (b)), the same conclusions hold except for the maximum strain. Indeed, we observe that the maximum axial strain at the top surface is 20% larger in absolute value than the strain experienced at the bottom surface. From the knowledge of the curvature K_B, the theoretical prediction of the stress σ_{11} versus strain ε_{11} response is also added to Figs 5.8 (a) and (b) for two material points located at z = ±16.6μm (see dotted lines with squares or circles). It is clearly observed that some discrepancies exist

between the theory and the finite element response. Of course, in the theory, a skew-symmetric distribution of strain is assumed, which is not clearly the case in the finite element simulations. The pure bending assumption is better fulfilled for $\theta = 90°$ than for $\theta = 135°$.

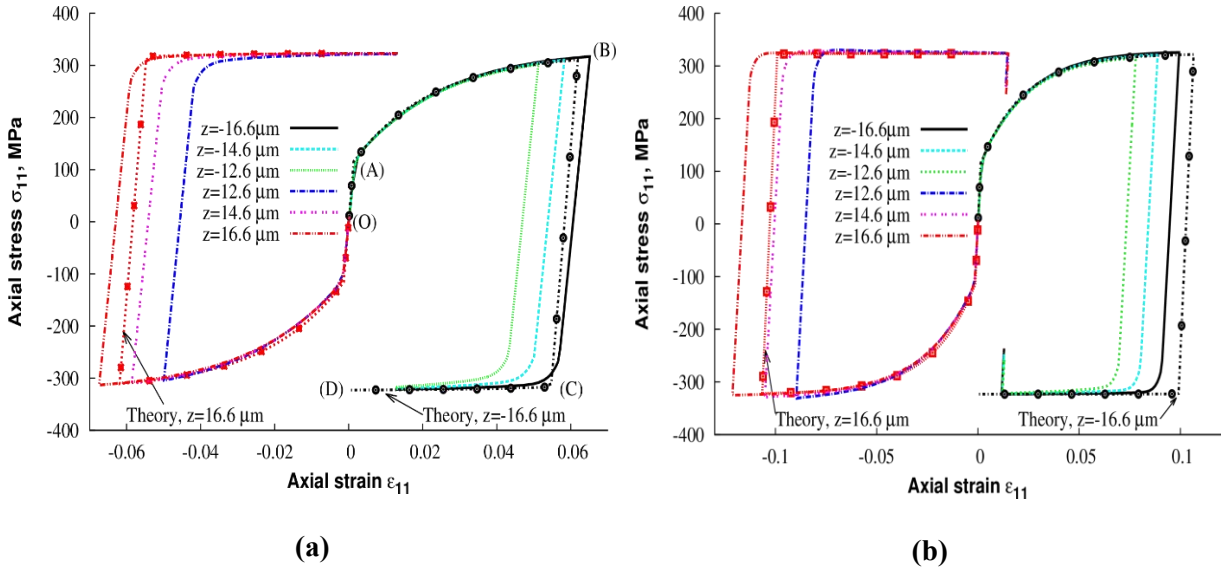

Figure 5.8: Loading path faced by material points along the thickness during the peeling process. **(a)** Peel angle of 90° **(b)** Peel angle of 135°. A local orientation is adopted in the finite element simulations. The reference parameters are those of Table 4.1 of chapter 4 with $\gamma = 40$.

At least for the parameters adopted as reference in Table 4.1, the proposed expression Eq. (4.22) for the work done by bending plasticity enables to recover precisely the interface fracture energy inserted in the numerical calculations when the peel angle is $\theta = 90°$, as presented in Table 5.1. Peel tests with an angle θ in the range [+45°, +135°] are also simulated. The reference parameters of Table 4.1 are still adopted with $\gamma = 40$. Fig. 5.9 displays the estimated value of the fracture energy Γ assuming that the force per unit width P and the maximum curvature K_B are known quantities (obtained from FE simulations). As already mentioned, the pure bending theory predicts a consistent interface fracture energy using Eqs (4.20) and (4.22) when $\theta = 90°$. It is observed that for $\theta = 120°$, 135°, the proposed model based on the expression of Ψ leads to an estimate for Γ of 1160N/m, instead of 1055N/m. Clearly, the film radius is too small when compared to the film thickness for the bending theory to be accurate, see Hill [60]. For $\theta = 60°$, 45°, the strain map in the film thickness is neither fully consistent with a pure bending approach, see Fig. 5.7. Indeed, for $\theta < 90°$, the stretching of the film is more intense, and the tensile contribution is noticeable. It is observed that for $\theta = 60°$, the estimate of Γ is still accurate (less than 5% difference,

Γ(60) = 990N/m). The situation is different for θ = 45° with more than 10% difference (Γ(45) = 909N/m). The prediction of Γ based on the elastic-perfectly plastic approach Eq. (4.25) is also superimposed to Fig. 5.9. The prediction of Γ based on the approximate relation (4.24) is not presented since it coincides almost with the one given by Eq. (4.22). The elastic-perfectly approach is underestimating Γ for the considered material parameters, except for the large angle condition with θ = 135° or θ = 120°. So from Fig. 5.9, it can be mentioned that the estimation of the interface fracture energy can be reasonably captured by the present work, from the knowledge of the experimental force and curvature for tests with peel angle around θ = 90°. Interestingly, it is seen that the closed form expression derived from Eq. (4.24) provides also consistent estimate and can be used instead of Eq. (4.22), at least for the material parameters considered here.

From previous works of the literature (Wei and Hutchinson [7] , Kim and Kim [19], Wei [56], Martiny et al [9] or Thouless and Yang [61]), it is known that the results of finite element simulations of peel tests for an elastic-plastic film are highly influenced by the properties of the interface, i. e. the parameters of the cohesive law (here the interface fracture energy Γ and the peak stress $\hat{\sigma}$). Next, we propose to investigate their relative influence on the force and curvature during a peel test. The material behavior is still described by a Voce law with parameters listed in Table 4.1 and γ = 40. We assume that for a given angle θ = 90°, the force P is known. For different values of Γ, the peak stress $\hat{\sigma}$ is adjusted so that the force P at θ = 90° is unchanged, see Martiny et al. [9]. Fig. 5.10 displays the evolution of the peel force P and the curvature K_B for 6 sets of parameters (Γ, $\hat{\sigma}$) defined in Table 5.2. As Γ is reduced, the peak stress has larger value leading to a larger curvature (small radius R). Therefore, the work done by bending plasticity is enlarged. For Γ = 1055N/m and $\hat{\sigma}$ = 10MPa, finite element simulation of the peel test at θ = 90° has provided a curvature of K_B = 3759m^{-1} (a radius R = 248μm) while for Γ = 527.5N/m and $\hat{\sigma}$ = 72MPa, the curvature is K_B = 6042m^{-1} corresponding to a radius of R = 148μm. After this calibration, the force P is evaluated for four other angles θ = 45°, 60°, 120° and 135°. Fig. 5.10 shows that the force is quite insensitive to the 6 sets (Γ, $\hat{\sigma}$) for θ > 90° while it varies significantly when θ < 90°. This effect is larger for θ = 45° than for θ = 60°. For instance, with θ = 45°, one has P = 3777N/m

for Γ = 1055N/m and only P = 3300N/m when the interface fracture energy is reduced by a factor of two Γ = 527.5N/m. Remember that $\hat{\sigma}$ is adjusted so as to preserve the force level at θ = 90°. Fig. 5.10 indicates also that the curvature is the most sensitive feature to any variation of (Γ, $\hat{\sigma}$), see also Thouless and Yang [61] for the role of the peak stress on the plasticity development at the onset of the crack propagation. Therefore, to identify the interface fracture energy Γ, a peel test at θ = 90° where the force and curvature are recorded, may be sufficient. Nevertheless, it seems also important to validate this estimate by confirming the prediction of the force by performing another test; a peel test at angle θ = 45° seems to be a good candidate. Indeed, the force P for small angle θ is quite sensitive to value of the interface fracture energy. Of course, all the present results are valid for the specific cohesive law (5.5) and (5.6) and for the given material behavior.

Γ (N/m)	1055	949.5	844	738.5	633	527.5
$\hat{\sigma}$ (MPa)	10	15	21	31	46	72

Table 5.2 : Couples (Γ, $\hat{\sigma}$) leading to the same force per unit width for the peel angle θ = 90°.

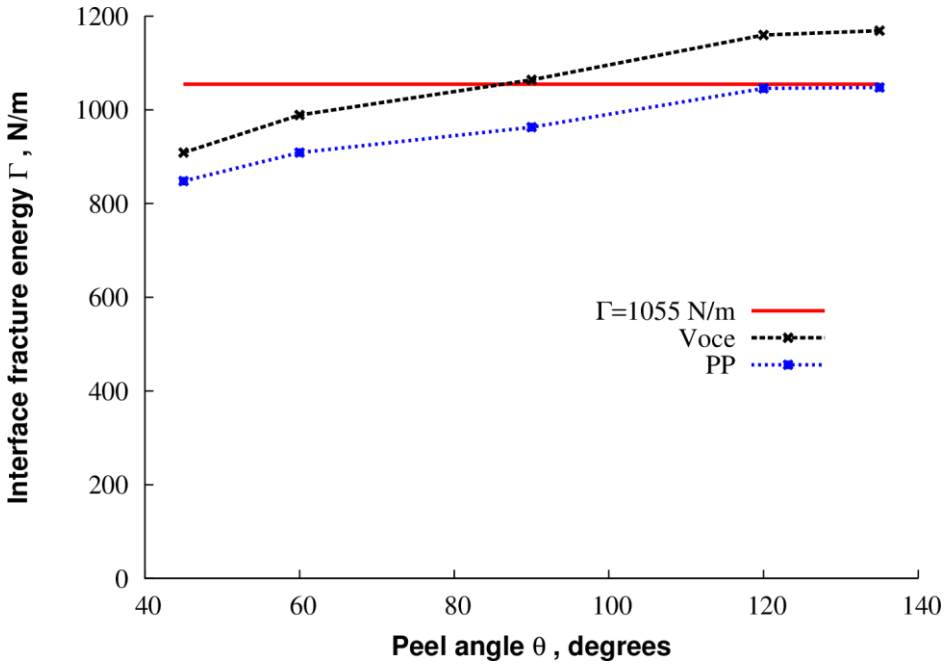

Figure 5.9: Effect of the peel angle on the estimated interface fracture energy. The predictions based on the present work Eq. (4.22) and on Eq. (4.25) derived for an elastic-perfectly plastic material are compared. The material parameters are listed in Table 4.1 with γ = 40.

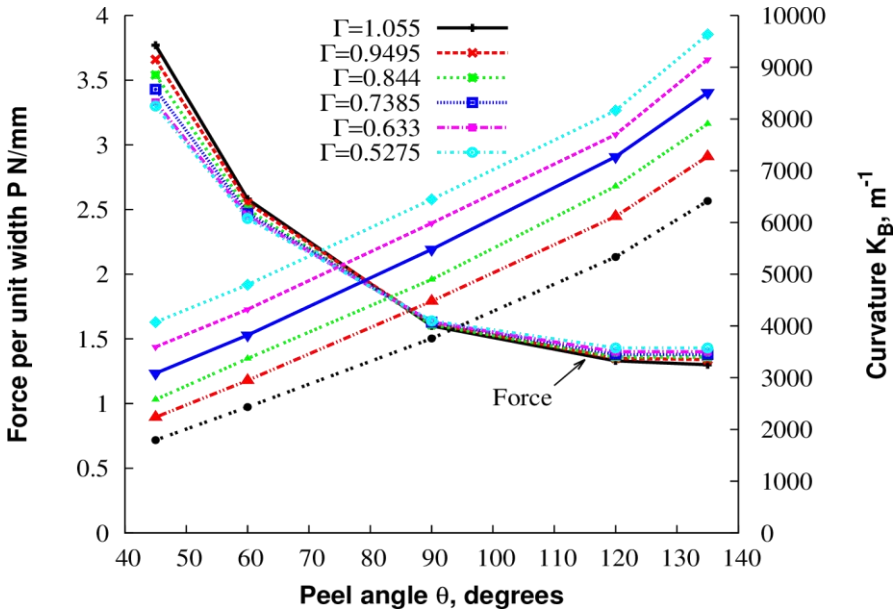

Figure 5.10: Force per unit width and curvature for various peel angles θ. Note that the cohesive law parameters listed in Table 5.2 are adjusted so that the peel force P(θ = 90°) is preserved.

5.4 Application to copper used in the PCB industry

5.4.1 Elastic-plastic behavior

Fig 5.11 presents the uniaxial stress-strain response derived from a tensile test, performed on copper foil (35 µm and 70 µm). Digital image correlation has been used to measure the strain (ε_{xx} and ε_{yy}) in the central part of the specimen during the test. Assuming that the elastic response is isotropic, the Young's modulus and the Poisson's ratio are E=106GPa and $\nu = 0.36$, (rep. E=120GPa and $\nu = 0.36$) for the 35 µm thickness (resp. 70 µm) copper film. Note that elastic properties of the two copper types are different since they are produced by different companies.

Fig. 5.12 displays the plastic strain versus true stress. The hardening is important at early deformation stage. For larger plastic strain, the hardening behavior is quite linear. The response is fitted by adopting four Voce laws:

$$\bar{\sigma} = \sigma_0 + \sum_{i=1}^{N} Q_i(1 - \exp(-\gamma_i \varepsilon^P)) \tag{5.7}$$

where $\bar{\sigma}$ and ε^P are the equivalent stress and accumulated plastic strain.

Material parameters for copper films with 35 µm and 70 µm thickness (named Cu_{35} and Cu_{70} later in the text) are presented in Table 5.3. The yield stress at moderate to large plastic strain for the 35 µm film is larger than the Cu_{70} one. Therefore, for a fixed plastic strain, the plastic dissipation is larger for Cu_{35} than Cu_{70}. The expression (5.7) is needed since in the FE simulation, it has been shown that the plastic strain is larger than 0.07 when the radius is small. Thus, even if from experiments, the plastic behavior is identified in the range of [0, 0.08] (see Fig. 5.12), the use of Eq. (5.7) enables to extrapolate the measured response to the necessary domain observed in peel tests.

As proposed in section 5.3, a peel test at 90° has been carried out to identify the interface fracture energy Γ. For Cu_{35}, the curvature and peel force per unit width are: $K = 7142.85\ m^{-1}$, $P = 1600 N/m$. For Cu_{70}, one has: $K = 2596.1\ m^{-1}$, $P = 2170\ N/m$. From the theory proposed in chapter 4 (using Eqs (4.22), (4.23), (4.20)) adopting the plastic behavior modeled by four Voce components, the interface fracture energies are derived: $\Gamma_{35} = 202\ J/m^2$ and $\Gamma_{70} = 526\ J/m^2$. Note that only the material behavior, the peel force and the curvature are needed to obtain the interface fracture energy Γ.

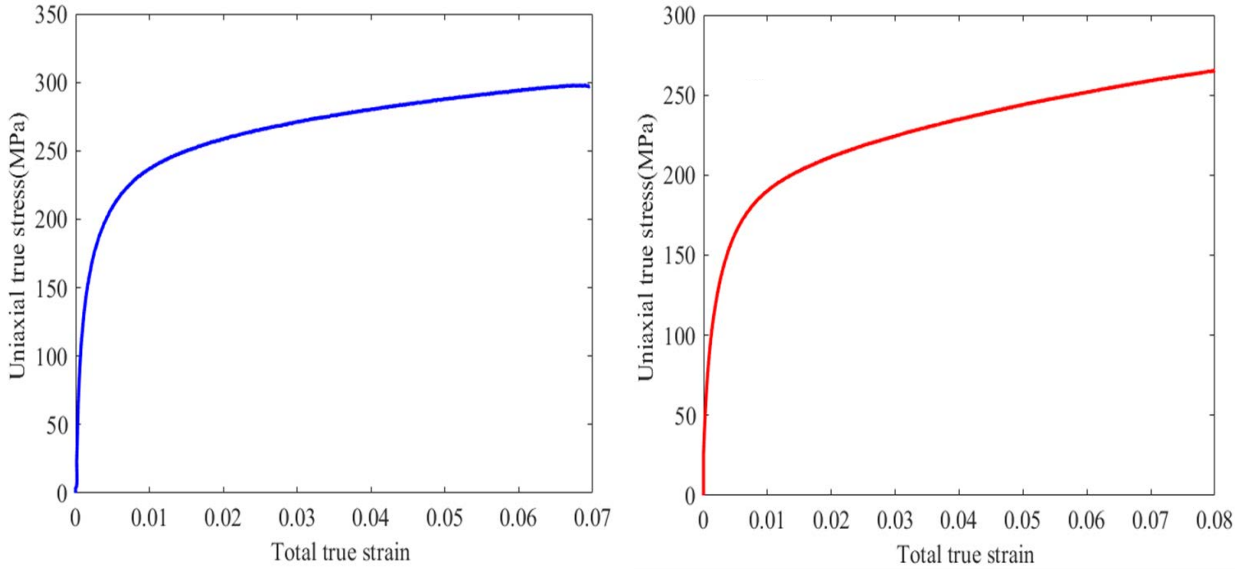

(a) **(b)**

Figure 5.11: True stress versus true strain for copper, obtained by performing a tensile test on copper foil: **(a)** 35 µm thick and **(b)** 70 µm thick.

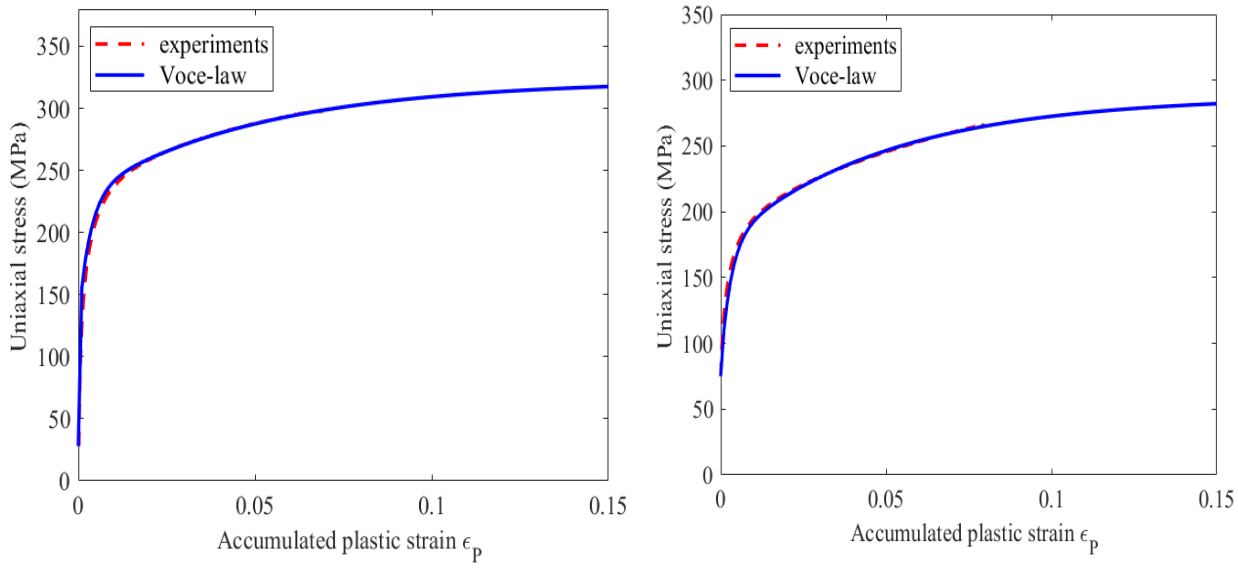

(a) **(b)**

Figure 5.12: Plastic response of copper foil fitted by four Voce laws: **(a)** 35 µm thick and **(b)** 70 µm thick.

To calibrate the critical stress $\hat{\sigma}$, a parametric study is done on a 90° peel test. The critical stress is chosen such that the numerical peel force is equal to the experimental one.

	σ_0[MPa]	Q_1[MPa]	γ_1	Q_2[MPa]	γ_2	Q_3[MPa]	γ_3	Q_4[MPa]	γ_4
$\mathbf{Cu_{35}}$	28	100	4296	101	305	91.75	20	5	2
$\mathbf{Cu_{70}}$	75	3.75	8000	3.33	6000	93.6	330	112	20

Table 5.3: Material parameters used to model the plastic response of the copper film for 35 µm and 70 µm thickness**.**

Results in Fig. 5.13 show that the peel force increases with the critical stress $\hat{\sigma}$. As $\hat{\sigma}$ increases, the radius R_C of the film decreases, see Fig. 5.14. Notes that R_C is the radius of the top surface obtained from numerical calculations. These observations were already represented in the literature, see Mohammed et al [62] and Tantideeravit et al [63]**.**

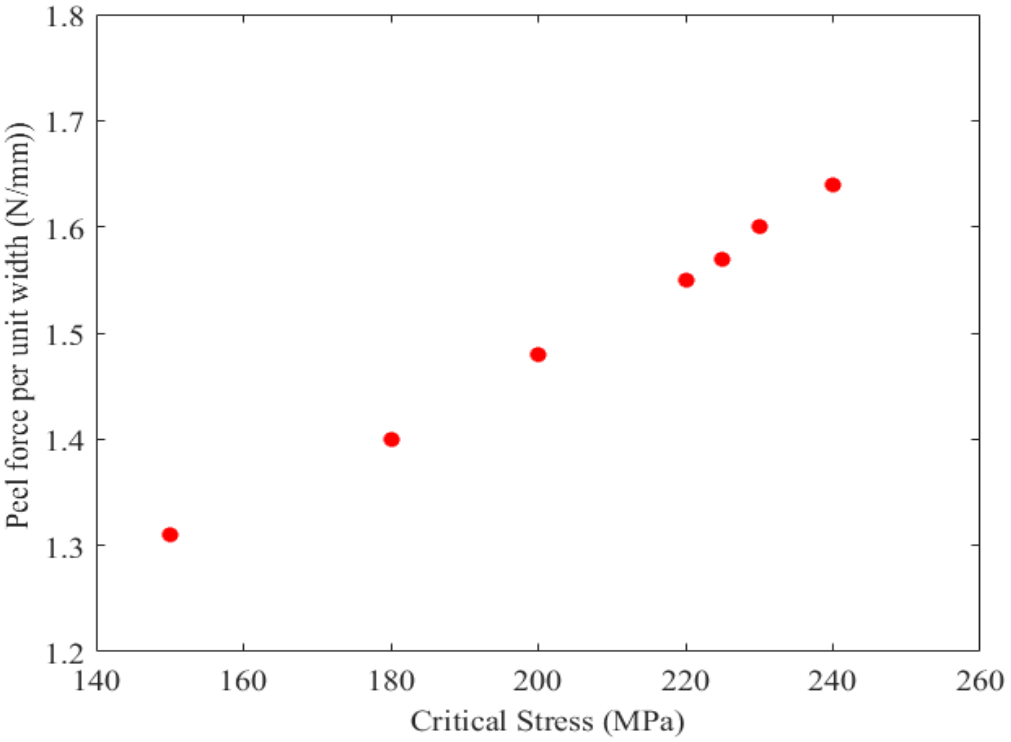

Figure 5.13: Influence of the critical stress $\hat{\sigma}$ on the predicted peel force per unit width. A peel angle of 90° is adopted for the numerical model with a Γ value of $202\mathrm{J/m^2}$ for $\mathrm{Cu_{35}}$.

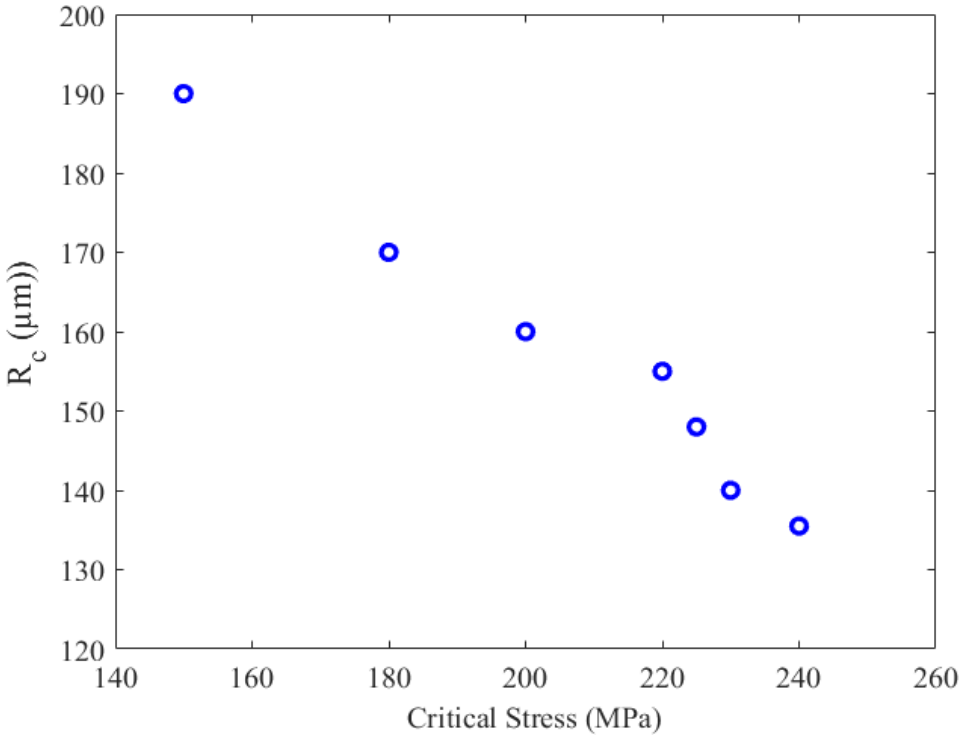

Figure 5.14: Influence of the critical stress $\hat{\sigma}$ on the predicted radius R_C. A peel angle of 90° is adopted for the numerical model with a Γ value of $202 J/m^2$ for Cu_{35} .

The results in Fig. 5.13 and Fig. 5.14 show that not only the value of Γ is important to obtain an accurate cohesive zone modeling simulation but the value of $\hat{\sigma}$ has also a major influence on the predicted peel force and the curvature of the film. This funding was already mentioned in the work of Blackman et al. [64] who emphasized that the outcome of the finite element modeling is typically dependent upon the values of both the cohesive element parameters. The work of Wei and Hutchinson [7] also showed that the primary parameters characterizing the traction separation relation are the work of adhesion Γ and the peak separation stress $\hat{\sigma}$.

5.4.2 Effect of the peel angle

From a peel test at 90°, the two parameters of the cohesive zone are defined. We propose next to compare the prediction of the FE model to experimental data obtained by varying the peel angle. Simulations are carried out for a peel angle of 45°, 60°, 90°, 120° and 135°. The variation of the peel force registered at steady-state versus peel angle for the 35 µm copper film is shown in Fig. 5.15 (a). We observe on this

figure that the peel force at steady-state decreases when the peel angle increases. These conclusions agree well with the literature. In Fig. 5.15 (b) the corresponding radius R_C is also decreasing when the peel angle increases. It can be seen that for large peel angle, the radius is very small, of the order of 100 µm. Remember that from the energy balance, a simple link between Γ, P and Ψ exists. From Fig. 5.15 (a), we clearly see that for Cu_{35}, P is larger than Γ so the work done by bending plasticity Ψ is predominant.

Fig. 5.16 presents the maps of von Mises stress inside the copper film during a peel test. One clearly observes a first active plastic zone where the plastic strain is accumulated (path AB of Fig. 4.2) and a second plastic zone which generally occurs at some distance from the cohesive zone in the detached film (Kim and Aravas [6]; Kinlock et al. [41], Wei and Hutchinson, [7]).

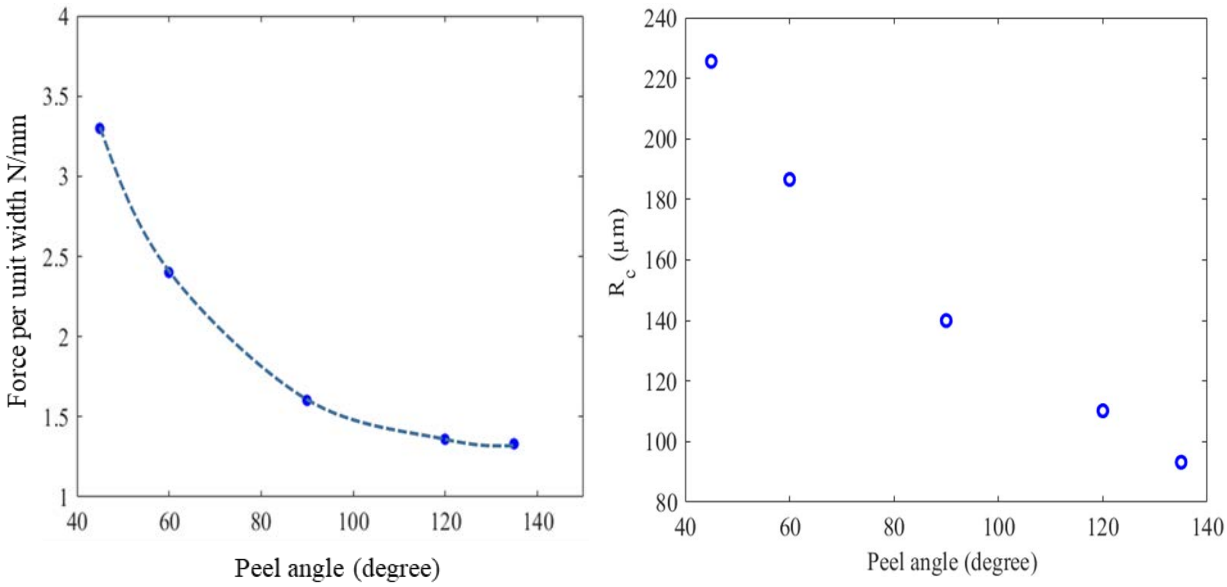

(a) **(b)**

Figure 5.15: **(a)** Variation of the peel force at the steady-state versus peel angle **(b)** Variation of the copper film radius at the steady-state versus peel angle. Cu_{35} film is considered. The parameters of the cohesive elements are: Γ=202 J/m^2, $\hat{\sigma}$=230 MPa.

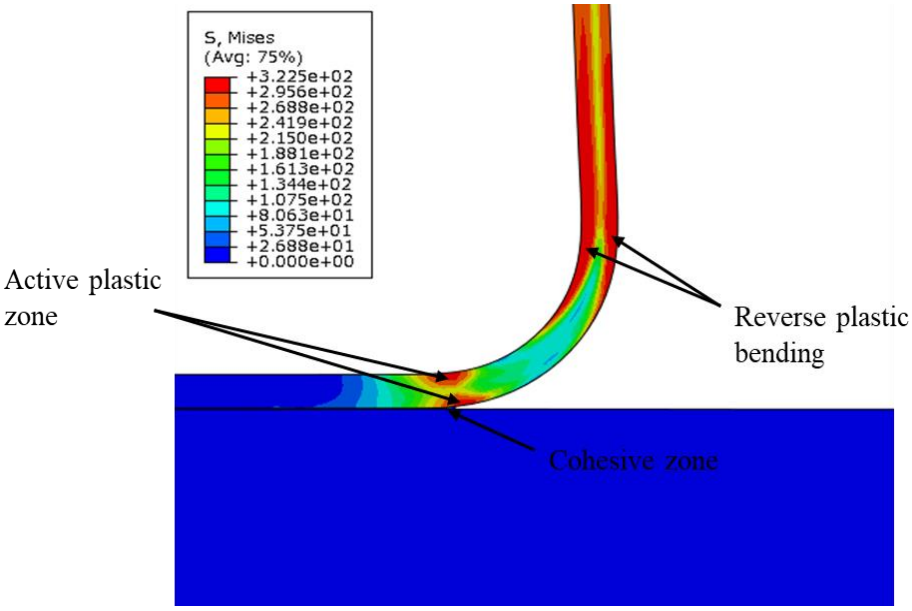

Figure 5.16: F.E Peel test at 90°. Two zones of large von Mises stress are present, which correspond to the area where the material develops plasticity during bending and reverse bending. The simulation is performed for Cu_{35} film with Γ=202J/m^2, $\hat{\sigma}$=230MPa.

5.4.3 Effect of the film thickness on the peel force and on the film radius

In order to show the effect of the film thickness, we develop finite element calculations for the two film thicknesses (35µm and 70µm) and for various angles: 45°, 60°, 90°, 120° and 135°. Note that both films are commercial electrodeposited copper (HTE grade 3) manufactured by two different companies. As observed in Fig. 5.12 their plastic responses are different. Their respective interface fracture energies are quite different also: $\Gamma_{Cu_{35}} = 202\ \mathrm{J/m^2}$ and $\Gamma_{Cu_{70}} = 526\ \mathrm{J/m^2}$. The variation of steady-state peel force versus the peel angle is shown in Fig. 5.17. We can see from Fig. 5.17 that when the copper film thickness increases, the steady-state peel force increases. This is in agreement with the literature, see Zhao and Wei [22]. The variation of the copper film radius versus the peel angle is presented in Fig. 5.18. In this chapter R_c represents the radius of the curvature of the top surface. As the film thickness increases, the radius of curvature increases. When the film thickness is varying from 35µm to 70µm, the radius is multiplied by three. Therefore, the level of the plastic strain ($\varepsilon_{11} \cong -Kz$) accumulated in the thick film is reduced. Nevertheless, as the volume of film which has faced plasticity is enlarged, then in total, the plastic dissipation in the thick film is larger. Thus the peel force is also increased. For instance, if we consider the peel test at $\theta = 90°$, the peel force per unit width for Cu_{35} is P=1.6 N/mm

while for Cu_{70}, P is 2.17 N/mm. The difference is around 0.6 N/mm. Part of the difference is due to a larger interface fracture energy $\approx 0.3\ \mathrm{mJ/mm^2}$. Half of the increase ($\approx 0.3\ \mathrm{mJ/mm^2}$) is due to an enhancement of the plastic dissipation. Note that when the film thickness is very large, no plasticity will develop anymore and the measure of the peel force will provide a direct estimate of the interface fracture energy, see Wei [40] and Thouless and Yang [61].

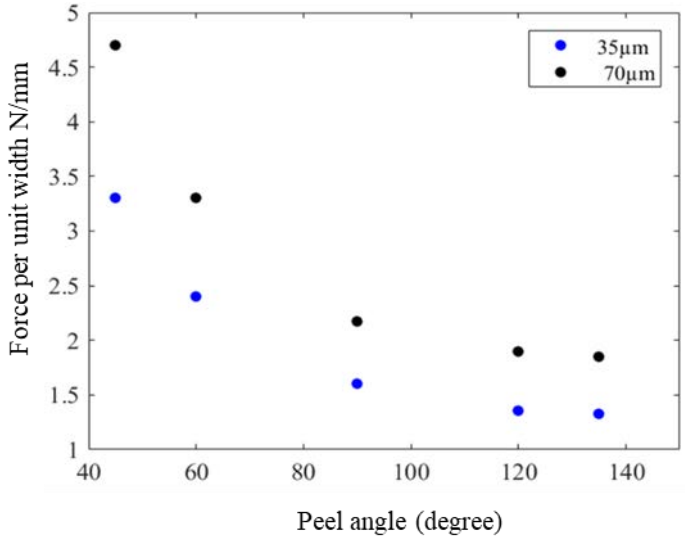

Figure 5.17: Steady-state peel force as a function of the peel angle for two thicknesses of the copper film. Finite element simulations are performed adopting the identified elastic-plastic behavior of copper and the parameters identified based on a 90° peel test.

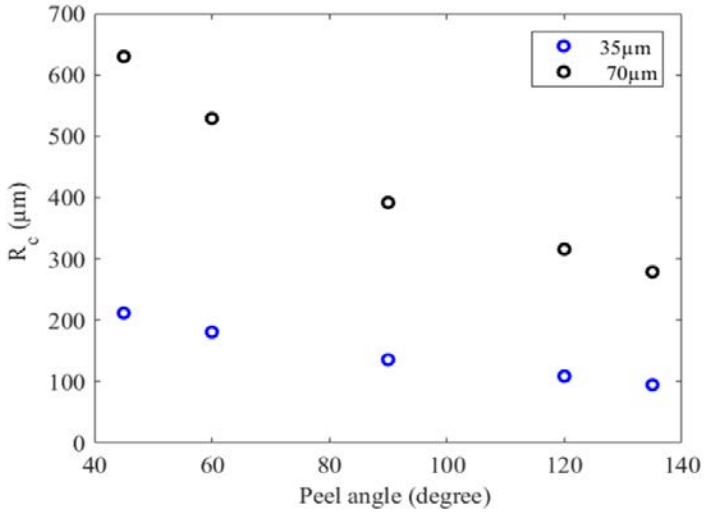

Figure 5.18: Film radius as a function of the peel angle for two thicknesses of the film. Finite element simulations are performed adopting the identified elastic-plastic behavior of copper and the parameters identified based on a 90° peel test.

5.4.4 Energy balance based on the numerical peel model

The rate of external work of the peel force, of work done by bending plasticity, of elastic energy are evaluated in Fig. 5.19. It is seen that for all angular conditions, the rate of elastic energy (in the film and the substrate) is negligible during steady state. This result validates the energy balance Eq. (4.20), where the rate of external work is the sum of two contributions: work done by bending plasticity and work rate to create the interface. In steady state, the rate of external work $\mathscr{P}^{ext}$ is given by:

$$\mathscr{P}^{ext} = \mathrm{PV}(1 - \cos\theta) \tag{5.8}$$

Note that the velocity V is fixed V=0.5mm/s. Therefore, the value of the external work rate presented in Fig. 5.19 is retrieved from Eq. (5.8) adopting the peel force value of Fig. 5.17. The difference between the rate of the external work and the dissipation rate is simply ΓV. For the present configuration, plasticity plays an important role in the energy balance and the peel force cannot be used directly to provide an estimate of the interface fracture energy. In the PCB industry, a peel test at 90° is required and according to the standard IPC-TM-650-2.4.8, the interface energy is estimated by $\Gamma = \mathrm{P}$. This is not fully consistent.

5.4.5 Evolution of the plastic strain in copper film

Fig. 5.20 presents the evolution of the accumulated plastic strain for two elements are located at the top and the bottom of the copper film. The peel angle is varied in the range [45°, 135°]. One can observe that the plastic strain presents a first stage with fast evolution. This corresponds to stage AB of Fig. 4.2. Then a plateau is observed, corresponding to stage BC. A second increase of the plastic strain is seen during the reverse bending phase (stage CD). Subsequently, the peel arm is not facing plasticity anymore and the plastic strain is frozen. It is seen that for all angles considered here, the plastic strain accumulated at the top surface is larger than at the bottom surface. Note that as the radius is small, the thickness of the film is not negligible when compared to the radius, so it can be argued that the local radius is significantly smaller at the top surface. This is particularly true for large peel angles. At 135°, the difference in plastic strain is equal to 0.1 between the top and the bottom surface. It is also observed that for $\theta < 90°$, the plasticity development is higher at the bottom surface during the first bending stage

AB. This may be due to the additional effect observed at the crack tip which differs from plasticity due to pure bending. Shear contribution also may be part of the explanation. Note that results are not presented here for Cu_{70} since trends and conclusions are similar.

5.4.6 Mixed mode evaluation

The present cohesive zone model combines mode I and mode II. The mode I and mode II components of the energy release rate are defined as:

$$G_I = \int_0^{\delta_n} \sigma_n d\delta_n \quad \text{and} \quad G_{II} = \int_0^{\delta_t} \sigma_t d\delta_t$$

From the numerical simulation, these two quantities can be evaluated up to failure. Fig. 5.21 presents the normal and shear stress-strain response of the cohesive element during the peeling process. Note that the normal and the shear strain, defined in Eq. (5.2) and Eq. (5.3) provide a measure of the displacement δ_n and δ_t since in our F.E simulation t_0 has a fixed value: $t_0 = 0.001mm$. As a steady state prevails, the results are valid for any cohesive elements of the model. We clearly observe that the response of each mode is bilinear. From Fig. 5.21, the contributions G_I and G_{II} up to failure are evaluated and summarized in Table 5.4. The contribution due to Mode II (shear) is smaller than the contribution due to mode I for each peel angle. Nevertheless, the shear contribution is not negligible.

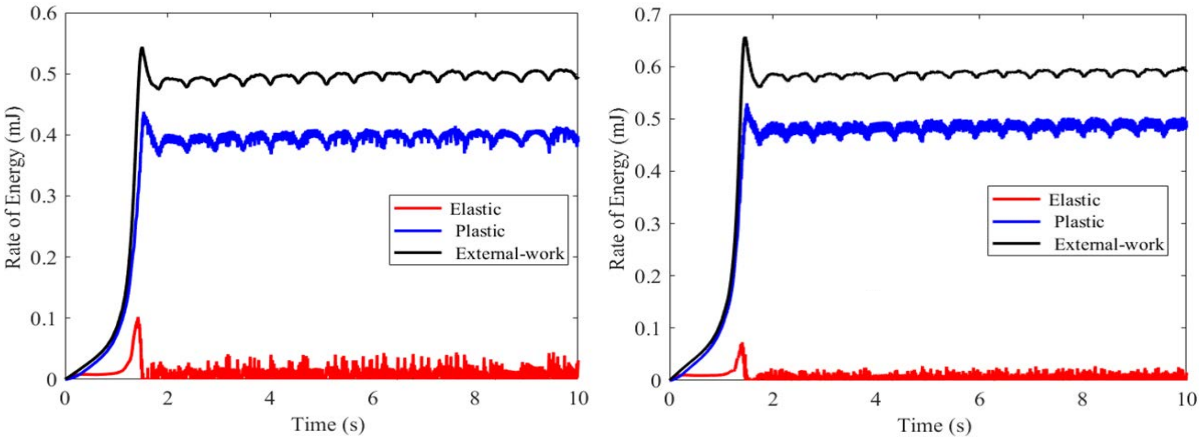

(a) **(b)**

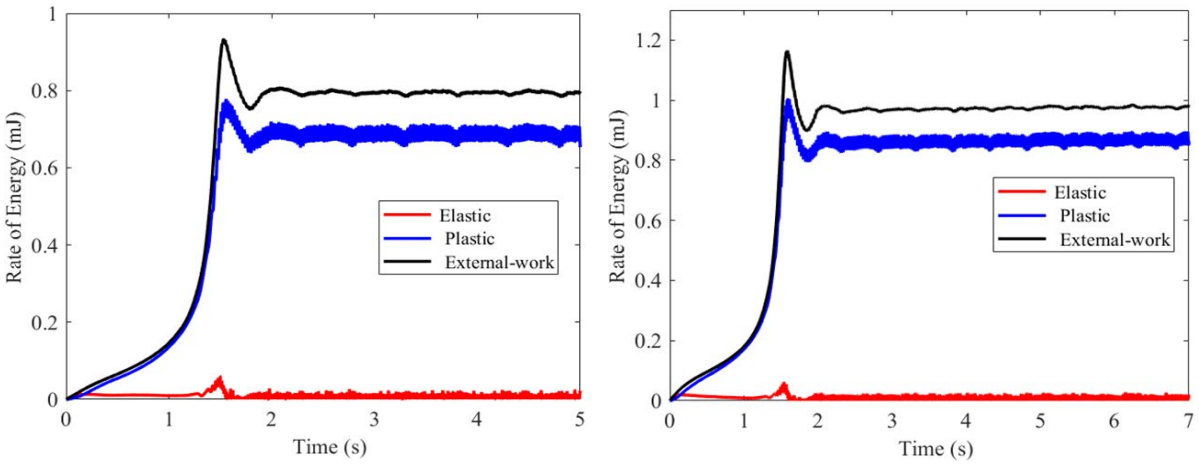

(c) **(d)**

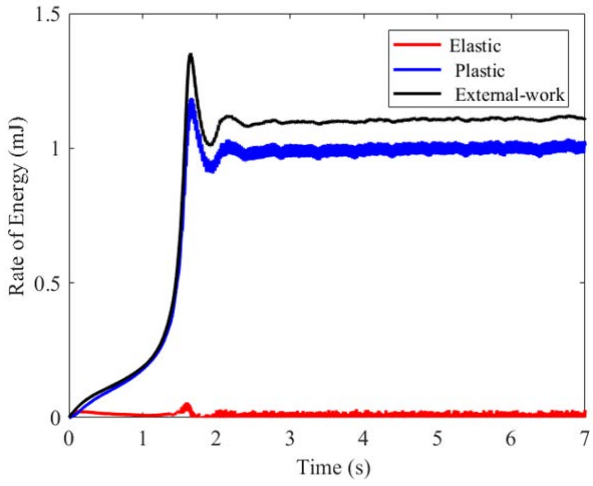

(e)

Figure 5.19: Rate of energies collected for the whole model for various angles: **(a)** 45°, **(b)** 60°, **(c)** 90°, **(d)** 120°, **(e)** 135°. Results are obtained by finite element calculations considering only Cu_{35} copper.

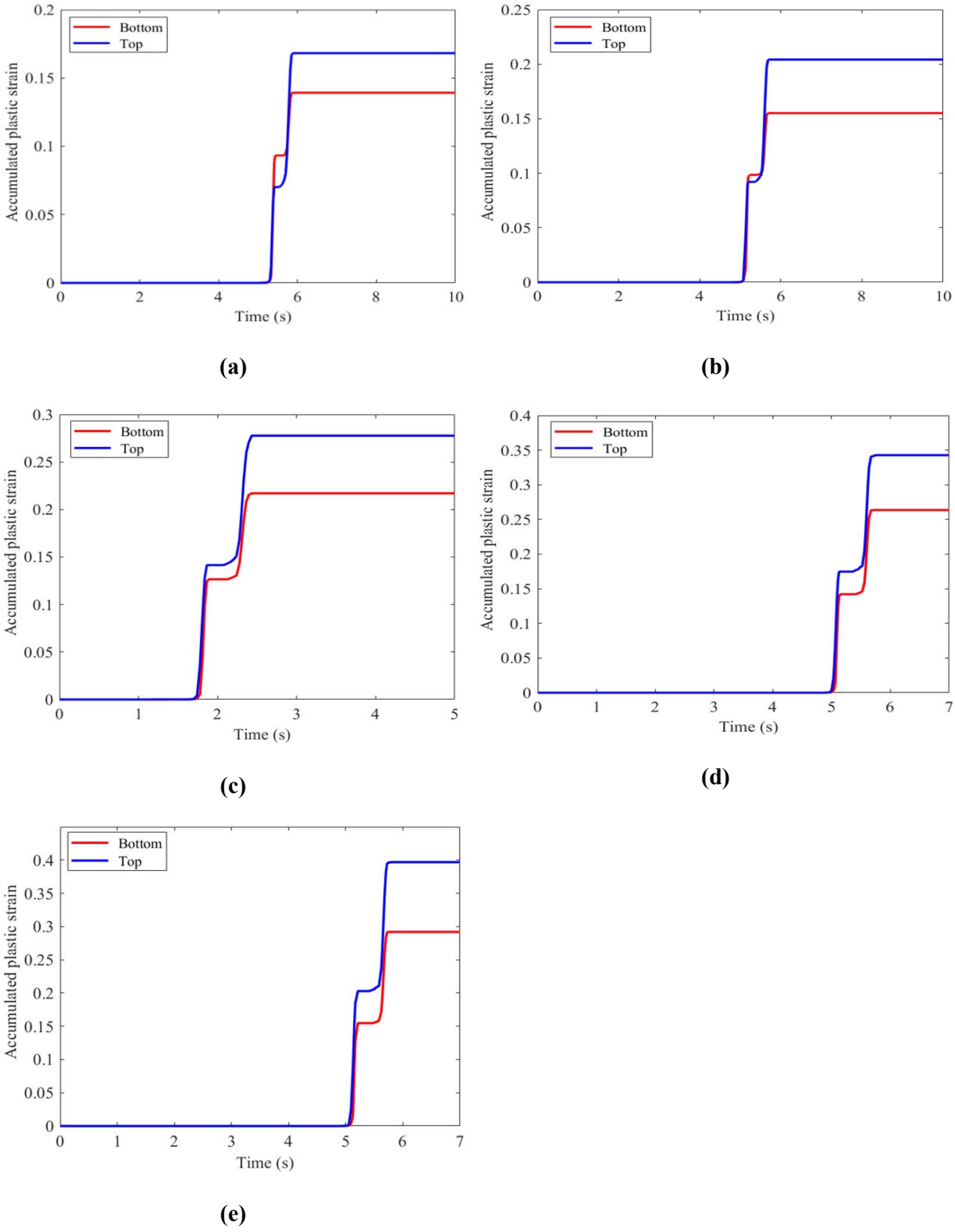

Figure 5.20: Accumulated plastic strain evolution for two elements located at the top and bottom of the film. **(a)** 45°, **(b)** 60°, **(c)** 90°, **(d)** 120°, **(e)** 135°. Results are obtained by finite element calculation considering only Cu_{35} copper.

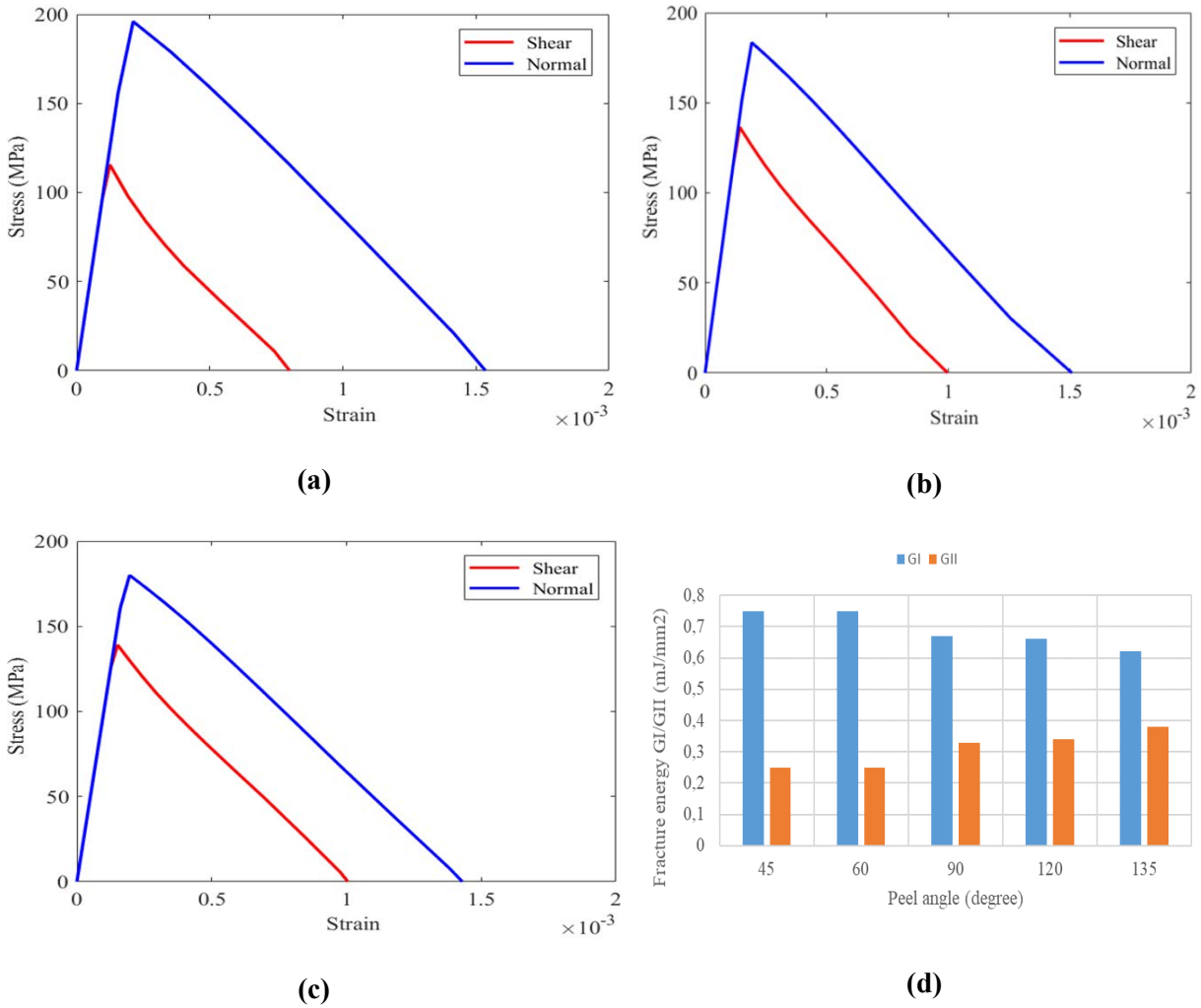

Figure 5.21: Normal and shear traction-separation laws for **(a)** 60°, **(b)** 90°, **(c)** 135° and **(d)** predicted mixed-mode contribution for different peel angles. Cu_{35} copper is considered here.

θ	45°	60°	90°	120°	135°
$G_I^{fracture}$ (N/mm)	0.153	0.15	0.14	0.14	0.13
$G_{II}^{fracture}$ (N/mm)	0.052	0.05	0.064	0.066	0.07
$\frac{G_{II}^{fracture}}{G_I^{fracture}}$	0.34	0.33	0.46	0.47	0.54
$\tan^{-1}\sqrt{\frac{G_{II}}{G_I}}$	30	30	34	34	36

Table 5.4 : The contribution of G_I and G_{II} for Cu_{35} copper.

One easily checked that $G_I^{fracture} + G_{II}^{fracture} = \Gamma$ (as expected). The ratio $\frac{G_{II}^{fracture}}{G_I^{fracture}}$ is increasing when θ is larger. The phase angle ($\tan^{-1}\sqrt{\frac{G_{II}}{G_I}}$) remains almost constant. This result is consistent with

Thouless and Yang [61] where it was seen that for a small peel strain ($\frac{P}{Eh}$), the phase angle was almost constant. Its value was 37° in Thouless and Yang [61] while here for Cu_{35}, the phase angle is varying in the range of [30°- 36°].

5.5 Comparison between experiments and simulation

In this new section, we propose to compare experimental data to FE results. For that purpose, simulations are performed with the following cohesive parameters: $\Gamma=202J/m^2$, $\hat{\sigma}$=230MPa for Cu_{35} and $\Gamma=526J/m^2$, $\hat{\sigma}$=55MPa for Cu_{70}. A good agreement between the numerical and experimental values of the peel force for both copper films (Cu_{35} and Cu_{70}) is seen in Fig. 5.22.

We also observe a good agreement between the experimental and numerical results for the film radius for both thicknesses (Cu_{35} and Cu_{70}), see Fig. 5.23. The experimental and simulated peel force and radius are reported in Table 5.5 for Cu_{35}. For the 35 µm film thickness, the agreement is less accurate. This may be explained by the fact that the interface fracture energy is evaluated based on the bending theory. Since in that configuration, the radius is small (see Table 5.3), then the proposed theory may be less salient.

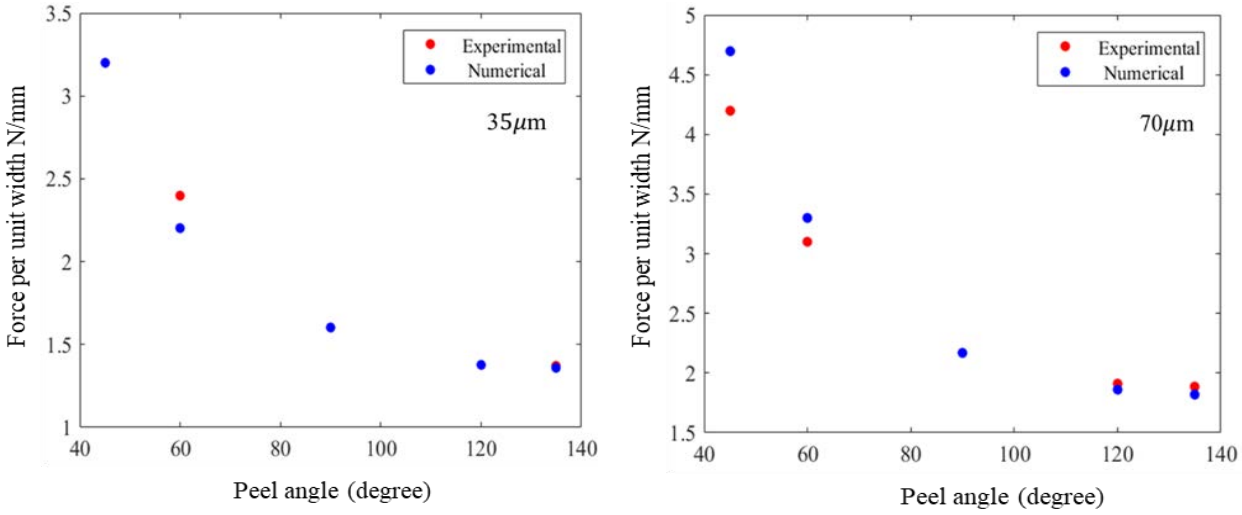

(a) **(b)**

Figure 5.22: Peel force at steady-state as a function of the peel angle for a copper film with thickness: **(a)** h=35 μm and **(b)** h=70 μm.

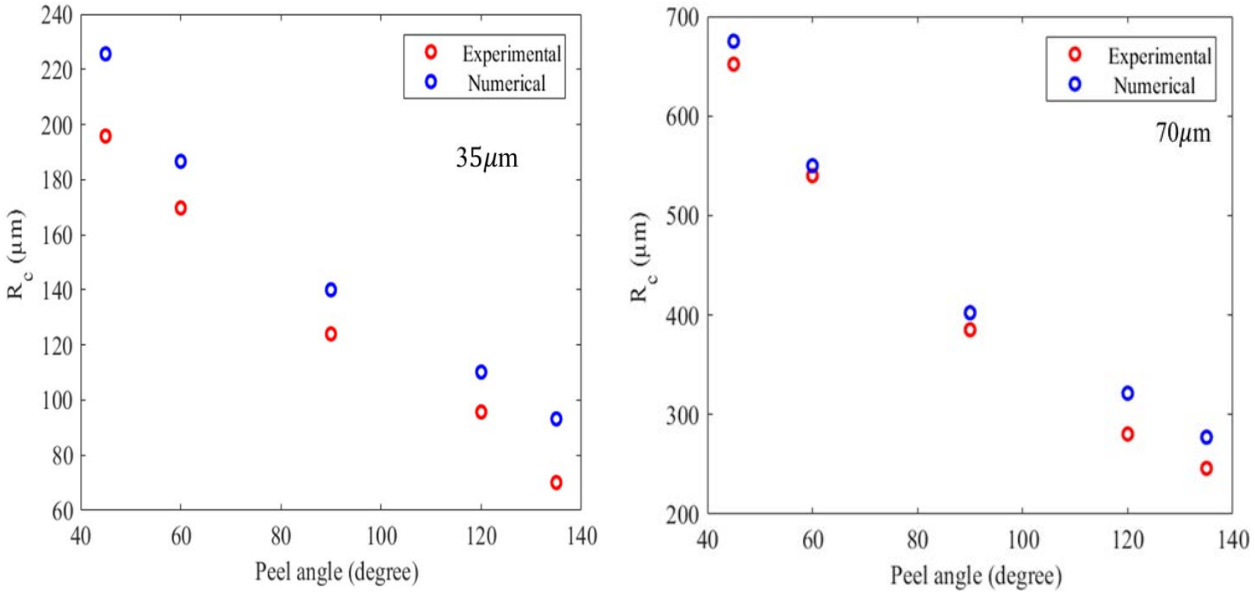

(a) **(b)**

Figure 5.23: Film radius at steady-state as a function of the peel angle for a copper film with thickness: **(a)** h=35 μm and **(b)** h=70 μm.

Peel angle (degree)	Experimental Peel Force (N/mm)	Numerical Peel Force (N/mm)	Experimental Rc (µm)	Numerical Rc (µm)
45	3.2	3.2	195.8	225.6
60	2.4	2.2	169.7	186.6
90	1.6	1.6	124	140
120	1.38	1.38	95.7	110.2
135	1.37	1.36	70.12	93.2

Table 5.5: Experimental and numerical peel force and copper film radius at different peel angles for Cu_{35} copper.

5.6 Conclusion

Finite element simulation of peeling process is carried out using a cohesive zone model. A comparison between finite element calculations and the analytical model is performed for various angles in the range [45°, 135°]. It is found that the present theory is accurate to analyze peel test for $\theta = 90°$ and provides a satisfactory estimate of the interface fracture energy for other peel angles. For $\theta = 90°$, at least for the material parameters adopted in section 5.3, the assumption of pure bending in the process zone is quite satisfactory. It is also observed that depending on the material parameters, the elastic-perfectly plastic approach proposed by Kim and Kim [19], Aravas et al. [8] can also be justified for a Voce type material when the saturation of the flow stress is observed for limited strain. The cohesive law parameters (interface fracture energy and peak stress) can be estimated by an inverse method, assuming that the force and curvature have been identified with recourse to finite element simulations or experiments. The identification of the cohesive law parameters could benefit from a further validation based on peel tests carried out mostly for small peel angle $\theta < 90$.

Failure due to delamination in Cu/woven composites can be also predicted using the cohesive zone model with necessary properties determined using peel tests and the new model developed in chapter 4. The elastic-plastic behavior of the film has been evaluated from an uniaxial test. The plastic dissipation during bending/reverse bending for a Voce type behavior is calculated using the identified copper film behavior and the experimental curvature measured for a test at 90° peel angle. This enables to provide an estimate of the interface fracture energy. This energy is adopted next in FE calculations. The critical stress $\hat{\sigma}$ is calibrated numerically based on a 90° peel test. Thus, the adopted set of values (Γ and $\hat{\sigma}$) is used for other peel angles (45°, 60°, 120° and 135°). It can be concluded that the proposed method used to evaluate the adhesive properties, which is based on a peel test and our derived estimate of the plastic dissipation, is appropriate for modeling the Cu/woven composite interface.

As an important result, the peel force and the radius at steady-state using finite element analysis with cohesive elements agree well with experimental results. A better agreement is nevertheless observed for thicker film where the film curvature is smaller (larger radius).

6 General conclusion and future work

We summarize here the main results obtained during this study and present some future works.

This thesis funded by the European program ITN H2020 (European Union's Horizon2020 Program, Excellent Science, Marie-Sklodowska-Curie Actions) is a collaborative work between LEM3 and CIMULEC. This joint work has started several years ago. During three years, we have also received the support from ANR (Agence Nationale de la Recherche) for the creation of the common laboratory called LEMCI**.**

The goal of this thesis is to determine the interface strength in printed circuit boards. To reach this goal, we have examined the delamination between copper and woven composite by developing peel test experiments, theoretical analysis of peeling and finite element simulations. The aim is to define a strategy to describe the interface properties in peel tests of elastic-plastic film.

In chapter 3, experimental peel test configuration has been developed for five different peel angles (45°, 60°, 90°, 120° and 135°) and for two different thicknesses of copper film: 35 µm and 70 µm. In experiments, the peel force was recorded and the copper film radius was measured during steady state. Tensile tests were carried out on copper film and we identified the elastic-plastic behavior of copper foil for 35 µm and 70 µm thickness. Chapter 4 provided an analytical expression of the work done by bending plasticity (plastic dissipation) during bending/reverse bending for a Voce type behavior. It has been seen that the plastic dissipation is highly sensitive to the curvature. The elastic-perfectly plastic approach proposed by Kim and Kim [19], Aravas et al. [8] can also be justified even for a Voce type material when the saturation of the yield stress is observed for limited strain.

Chapter 5 was dedicated to finite element simulations. In this chapter we have developed a numerical model for peeling. The copper was modeled by an elastic-plastic behavior, the interface between copper and the woven composite was modeled by cohesive elements with bilinear traction separation law. It was concluded that failure due to delamination in copper/woven composite can be predicted using cohesive elements with necessary properties determined using experimental data (elastic-plastic

response of copper) and the analytical expression for the plastic dissipation. Indeed, we proposed to use the analytical model developed for a certain class of hardening behavior (here Voce type) and the curvature of the film (peel test at 90°) to determine the interface fracture energy between film and the substrate. A parametric study was further conducted to determine the critical stress $\hat{\sigma}$. Thus the set (Γ and $\hat{\sigma}$) was used for other peel angles (45°, 60°, 120° and 135°). The effect of the film thickness on the peel force and on the film radius was investigated in this work.

Finally, a comparison between finite element calculations and experimental data was performed for all angles. The peel forces and the radius of the film obtained from finite element analysis agreed well with experimental results.

In the PCB industry, the interface fracture energy is evaluated based on a 90° peel test by dividing the peel force by the film width. So the plastic dissipation is not taken into account. In this work we have clearly shown that the plastic dissipation has an important effect on the interpretation of the peel test measurement.

Future works

As the film thickness in a PCB can be smaller than 35 µm, it is interesting to develop experimental peel tests for 17 µm thick copper film at room temperature. For such conditions, the radius is supposed to be very small. It could be also interesting to develop also experiments with thicker film so that plasticity could be negligible. DCB (double cantilever beam) test could be also of interest.

Experimental peel tests in this work are realized at the room temperature. We have started the development of peel tests at elevated temperature (up to +150°C) with a dedicated heating system for a 35 µm thick copper film. It has been observed from experiments that the peel force decreases when the temperature increases. So for the future, as the collaboration between CIMULEC and LEM3 will continue, experimental peel tests and numerical models at elevated temperature (up to +150°C) and low temperature (up to -50°C) have to be performed for different peel angles and different thicknesses of the copper film.

The analytical model developed within this PhD is based on the assumption that the copper film has an elastic-plastic behavior with isotropic hardening. It could be interesting to understand the role of kinematic hardening and its consequence on the definition of the interface fracture energy. For that, one needs to revisit the model by considering a Chaboche model, for instance. Concerning the finite element model, it could be also of interest to use different cohesive laws to evaluate whether the predictions are affected by such a choice. Finally, the critical stress $\hat{\sigma}$ was fitted by performing a parametric study. It could be of interest to develop pull out test experiments to provide a better estimate of $\hat{\sigma}$. In addition, in the finite element calculations, the curvature is closely related to the parameters of the cohesive law. From experiments, we have captured the shape of the film during steady state. But the boundary conditions at the bottom surface of the film, in the vicinity of the crack tip are not identified. They are prescribed using cohesive elements in our approach. It could be interesting to identify the shape and the parameters of the cohesive zone from measurements by applying for instance fading regularization with the MFS algorithm developed in Caillé et al [65].

From the PhD work, we have seen that the adhesion between laminates and copper can be investigated via peel tests. It is more problematic to develop similar experiments for testing the interface between electroless and electrodeposited copper. Therefore, an idea could be to develop ab initio simulation, see Jung et al [66] and Hallil et al [67]. In that case, the role of impurities could be anticipated.

Acknowledgments:

The research leading to these results has received funding from the European Union's Horizon 2020 research and innovation program (excellent Science, Marie Sklodowska-Curie Action) under REA grant agreement 675602 (OUTCOME project).

Appendix A: Derivation of the expression for the work done by bending plasticity Ψ**.**

The present appendix provides some details concerning the derivation for the expression of Ψ along the loading path (OABCD). For the elastic response of the film along path (OA), as depicted in Fig. 4.2, one obtains from Eq. (4.6):

$$\int_0^{K_e} MdK = \frac{\sigma_0^2 h}{6E} \tag{A1}$$

Since in peel test of thin copper film, the curvature K_B is large compared to K_e, one needs to evaluate the contribution to Ψ along (AB). The relationship between the moment *M* and the curvature *K* is given in that case by Eq. (4.10). With the definition $F\left(-\frac{2\gamma K}{\sqrt{3}},\frac{h}{2}\right) = -\exp\left(-\frac{\gamma K h}{\sqrt{3}}\right)\left(\frac{h\sqrt{3}}{4\gamma K}+\frac{3}{4\gamma^2K^2}\right)$ and with a change of variable $u = \frac{\gamma K h}{\sqrt{3}}$, one easily gets:

$$\int_{K_e}^{K_B} F\left(-\frac{2\gamma K}{\sqrt{3}},\frac{h}{2}\right)dK = \frac{3}{4\gamma^2}\left[G\left(-\frac{\gamma h}{\sqrt{3}},K_B\right) - G\left(-\frac{\gamma h}{\sqrt{3}},K_e\right)\right] \tag{A2}$$

where $G(x,y) = \frac{\exp(xy)}{y}$. The contribution linked to the term $F\left(-\frac{2\gamma K}{\sqrt{3}},t\right)$ in Eq. (4.10) with $t = \frac{\sigma_0\sqrt{3}}{2EK}$ is evaluated in a straightforward manner, so the plastic dissipation along the path (AB) is:

$$\begin{aligned}\int_{K_e}^{K_B} MdK = {} & \frac{\alpha h^2}{2\sqrt{3}}(K_B - K_e) + \left(\frac{\sigma_0}{\sqrt{3}} - \frac{\alpha\sqrt{3}}{2}\right)\frac{\sigma_0}{E^2}\left(\frac{1}{K_e}-\frac{1}{K_B}\right) \\ & -\frac{\beta\sqrt{3}}{\gamma^2}\left[G\left(-\frac{\gamma h}{\sqrt{3}},K_B\right) - G\left(-\frac{\gamma h}{\sqrt{3}},K_e\right)\right] \\ & +\frac{\beta\sqrt{3}}{\gamma}\exp\left(-\frac{\gamma\sigma_0}{E}\right)\left(\frac{\sigma_0}{E}+\frac{1}{\gamma}\right)\left(\frac{1}{K_B}-\frac{1}{K_e}\right)\end{aligned} \tag{A3}$$

For the unloading path (BC), the contribution to Ψ is readily:

$$\int_{K_B}^{K_B-K_B^*} MdK = -M_B K_B^* + \frac{Eh^3}{18}(K_B^*)^2 \tag{A4}$$

The last term corresponding to the reverse plastic loading phase (CD) is the most complex contribution and cannot be estimated in closed form expression in the general case. Indeed, the expression of *M* is

given by Eq. (4.16) where an integral term is already present. In addition, it is related to the position of the elastic-plastic transition t' defined by an implicit relation (4.14). Therefore, one can simply notice that:

$$\int_{K_B-K_B^*}^{0} MdK = \left[\frac{8EK_Bt_B^3}{9} - \frac{2\alpha}{\sqrt{3}}\left(t_B^2 + \frac{h^2}{4}\right) + \frac{4\beta}{\sqrt{3}}F\left(-\frac{2\gamma K_B}{\sqrt{3}}, t_B\right)\right](K_B^* - K_B) + I \tag{A5}$$

where the term *I* is provided in Eq. (4.23). As mentioned in Section 4.3, for metallic film when K_B and γ have large values, the accumulated strain (4.15) (resp. *t')* can be approximated as proposed in Eq. (4.17) (resp. by $t' = \frac{\alpha\sqrt{3}}{E(K_B-K)}$). After some classical mathematical developments, the integral term *I* is evaluated and the approximate closed form expression (4.24) is found.

References

[1] J. Venables, "Adhesion and durability of metal-polymer bonds," *J Mater Sci,* vol. 19, pp. 2431-2453, 1984.

[2] I. Mathieson and R. Bradley, "Improved adhesion to polymers by UV/ozone surface oxidation," *Int J Adhes Adhes,* vol. 16, pp. 29-31, 1996.

[3] R. S. Rivlin, "The effective work of adhesion," *Paint Technol 9,* pp. 215-216, 1944.

[4] J. G. Spies, "The peeling test on redux-bonded joints," *J. Aircraft Engng 25,* p. 64, 1953.

[5] K. Kendall, "Thin film peeling : the elastic term," *J. Phys D Appl Phys 8,* pp. 1449-1452, 1975.

[6] K.-S. Kim and N. Aravas, "Elastoplastic analysis of the peel test," *Int. J. Solids Struct, 24,* pp. 417-435, 1988.

[7] Y. Wei and J. W. Hutchinson, "Interface strength, work of adhesion and plasticity in the peel test," *Int. J. Fracture 93,* pp. 315-333, 1998.

[8] N. Aravas, K. Kim and M. Loukis, "On the mechanics of adhesion testing of flexible films," *Materials Science and Engineering, A 107,* pp. 159-168, 1989.

[9] P. Martiny, F. Lani, A. J. Kinloch and T. Pardoen, "Numerical analysis of the energy contributions in peel tests: a steady-state multilevel finite element approach," *Int. J. Adhes 28,* vol. 28, pp. 222-236, 2008.

[10] J. A. Williams and J. J. Kauzlarich, "The influence of peel angle on the mechanics of peeling flexible adherends with arbitrary load–extension characteristics," *Tribology International,* vol. 38, pp. 951-958, 2005.

[11] A. Molinari and G. Ravichandran, "Peeling of elastic tapes: effects of large deformations, pre-strainning and of a peel-zone model," *J Adhes; 84,* pp. 961-995, 2008.

[12] W. Sabbah, O. Avino-Salvado, C. Buttay, H. Frémont, A. Guédon-Gracia and H. Morel, "High temperature ageing of microelectronics assemblies with SAC solder joints," *Microelectronics Reliability,* Vols. 76-77, pp. 362-367, 2017.

[13] C. F. Coombs, "Printed Circuits Handbook," *Mcgraw-Hill,* 2001.

[14] A. Salaouelhadj, M. Martiny, S. Mecier, L. Bodin, D. Manteigas and B. Stephan, "Reliability of thermally stressed rigid–flex printed circuit boards for High Density Interconnect applications," *Microelectronics Reliability 54,* pp. 204-213, 2014.

[15] M. Freda and P. Reid, "Thermal Cycle Testing of PWBs – Methodology," *IPC Printed Circuit Expo, APEX and Designer summit procedings,* 2009.

[16] C. Kovalchick, A. Molinari and G. Ravichandran, "An experimental investigation of the stability of peeling for adhesives tapes," *J. of Mechs of Materials 66,* pp. 69-78, 2013.

[17] J. J. Benbow and F. C. Roesler, "Experiments on controlled fractures," *Proc. Phys. Soc. 70,* pp. 201-211, 1957.

[18] J. W. Obreimoff, "The splitting Strength of Mica," *Trans. Inst. Econ. Mineral, Metall.,* pp. 290-297, 1930.

[19] K. S. Kim and J. Kim, "Elastoplastic analysis of peel test for thin film adhesion," *J. Engin. Mat. Tech. 110,* pp. 266-273, 1988.

[20] Z. Peng, C. Wang, L. Chen and S. Chen, "Peeling behavior of a viscoelastic thin film on a rigid substrate," *Int. J of Solids and structures 51,* pp. 4596-4603, 2014.

[21] C. Kovalchick, S. Xia and G. Ravichandran, "Cohesive zone law extraction from an experimental peel test," *Experimental And Applied Mechanics,* vol. 4, pp. 237-245, 2013.

[22] H. Zhao and Y. Wei, "Determination of interface properties between micron-thick metal film and ceramic substrate using peel test," *Int. J. of Fracture 144,* pp. 103-112, 2007.

[23] C. Kovalchick, "Mechanics of peeling: Cohesive zone law and Stability," *Thesis, California Institute of Technology, Pasadena, California,* 2011.

[24] L. Afferrante and G. Carbone, "The ulthratough peeling of elastic tapes from viscoelastic substrates," *J of the Mechanics and Phys of Solids 96,* pp. 223-234, 2016.

[25] Y. Wei and H. Zhao, "Peeling experiments of ductile thin films along ceramic substrates-critical assessment of analytical models," *Int. J.of solids and strucutres 45,* pp. 3779-3792, 2008.

[26] L. F. Kawashita, D. R. Moore and J. G. Williams, "Analysis of peel arm curvature for the determination of fracture toughness in metal-polymer laminates," *J. of Materials Science,* pp. 241-248, 2005.

[27] G. Covarel, B. Bensaid, X. Boddaert, S. Giljean, P. Benaben and P. Louis, "Characterization of organic ultra-thin film adhesion on flexible substrate using scratch test technique," *Surface & Coatings Technology ,* vol. 211, pp. 138-142, 2012.

[28] X. Boddaert, G. Covarel, B. Bensaid, M. Mattei, P. Benaben and J. Bois, "Organic ultrathin film adhesion on compliant substrate using scratch test technique," *Thin Solid Films,* vol. 528, pp. 194-198, 2013.

[29] J. Song and J. Yu, "Analysis of T-peel strength in a Cu/Cr/Polyimide system," *Acta Materialia 50,* pp. 3985-3994, 2002.

[30] J. A. Williams and J. J. Kauzlarich, "Peeling shear and cleavage failure due to tape prestrain," *J Adhes Technol, 80,* pp. 433-458, 2004.

[31] M. J. Loukis and N. Aravas, "The effects of viscoelasticity in the peeling of polymeric films," *J. Adhes, 35,* pp. 7-22, 1991.

[32] H. Chen, X. Feng, Y. Huang, Y. Huang and A. Rogers, "Experiments and viscoelastic analysis of peel test with patterned strips for applications to transfer printing," *J. Mech. Phys solids 61,* vol. 61, pp. 1737-1752, 2003.

[33] D. H. Kaelble, "Theory and analysis of peel adhesion: rate-temperature dependence of viscoelastic interlayers," *J. Colloid Sci 19,* pp. 413-424, 1964.

[34] E. H. Andrews and A. J. Kinloch, "Mechanics of adhesive failure," *Pro R. Soc Lond A 332,* pp. 401-414, 1973b.

[35] W. T. Chen and T. F. Flavin , "Mechanics of film adhesion: elastic and elastic-plastic behavior," *J. Res. Dev. 16,* pp. 203-213, 1972.

[36] A. Gent and G. R. Hamed, "Peel mechanics for an elastic-plastic adherend," *J. Appl. Polym. Sci. 21,* pp. 2809-2817, 1977.

[37] A. D. Crocombe and R. D. Adams, "Peel analysis using the finite element method," *J. Adhes 12,* pp. 120-127, 1981.

[38] M. D. Chang, K. L. Devries and M. L. Williams, "The effects of plasticity in adhesive fracture," *J. Adhes 4,* pp. 215-221, 1972.

[39] J. Kim, K. S. Kim and Y. H. Kim, "Mechanical effects of peel adhesion test," *J. Adhes Sci. Tech. 3,* pp. 175-187, 1989.

[40] Y. Wei, "Modeling non linear peeling of ductile thin films - critical assessment of analytical bending models using FE simulations," *Int. J. of solids and Structures 41,* pp. 5087-5104, 2004.

[41] A. J. Kinloch, C. C. Lau and J. G. Williams, "The peeling of flexible laminates," *Int. J. Fracture 66,* pp. 45-70, 1994.

[42] N. Moës, C. Stolz, P. Bernard and N. Chevaugeon, "A level set based model for damage growth: the thick level set approach.," *Int. J. Numer. Meth. Eng,* vol. 86, no. 3, pp. 358-380, 2011.

[43] T. Gorris, P. E. Bernard and L. Stainier, "A study of transverse cracking in laminates by the Thick Level Set approach," *Mechanics of Materials,* vol. 90, pp. 118-130, 2015.

[44] D. S. Dugdale, "Yielding of steel sheets containing slits," *J. Mech. Phys. Solids,* vol. 8, pp. 100-104, 1960.

[45] G. I. Barenblatt, "The Mathematical Theory of Equilibrium Cracks in Brittle Fracture," *Adv. Appl. Mechs. ,* vol. 7, pp. 55-129, 1962.

[46] V. Tvergaard and J. W. Hutchinson, "The relation between crack growth resistance and fracture process parametres in elastic-plastic solids," *J. Mech. Phys. Solids,* vol. 40, no. 6, pp. 1377-1397, 1992.

[47] A. Needleman, "A Continuum Model for void Nucleation by inclusion debonding," *J. of Applied Mechanics,* vol. 54, pp. 525-531, 1987.

[48] A. Needleman, "An Analysis of tensile decohesion along an interface," *J. Mechs. Phys. Solids,* vol. 38, no. 3, pp. 289-324, 1990.

[49] V. Tvergaard and J. W. Hutchinson, "The influence of plasticity on mixed mode interface toughness," *J. Mech. Phys. Solids,* vol. 41, no. 6, pp. 1119-1135, 1993.

[50] J. Cui, R. Wang, A. N. Sinclair and J. K. Spelt, "A calibrated finite element model of adhesive peeling," *Int. J. Adhes 23,* pp. 199-206, 2003.

[51] IPC, "Peel strength of metallic clad laminates, IPC-TM-650 2.4.8," *Institute for Interconnecting and Packaging Electronic Circuits, www.ipc.org/TM/2.4.8c.pdf,* 1994.

[52] G. Girard, "Caractérisation et modélisation thermomécaniques de matériaux et de structures," *Mécanique des matériaux, Université de Lorraine,* 2018.

[53] G. Girard, M. Jrad, S. Bahi, M. Martiny, S. Mercier, L. Bodin, D. Nevo and S. Dareys, "Experimental and numerical characterization of thin woven composites used in printed circuit boards for high frequency application," *Composite Structure 193,* pp. 140-153, 2018.

[54] E. Simlissi, M. Martiny, M. Mercier, M. S. Bahi and L. Bodin, "Elastic-plastic analysis of the peel test for ductile thin film presenting a saturation of the yield stress.," *Int Journal of Fracture,* vol. 220, pp. 1-16, 2019.

[55] E. Voce, "The relationship between stress and strain for homogeneous deformations," *J Inst Metals,* no. 74, pp. 537-562, 1984.

[56] Y. Wei, "Modeling non linear peeling of ductile thin films - critical assessment of analytical bending models using FE simulations," *International Journal of Solids and Structures,* vol. 41, pp. 5087-5104, 2004.

[57] K. Kendall, "Shrinkage and peel strength of adhesive joints," *J. Phys, D Appl Phys 6,* pp. 1782-1787, 1973.

[58] S. A. S. J. Moidu K, "On the determination of fracture energy using the peel test," *Journal of Testing and Evaluation,* vol. 26, pp. 247-254, 1998.

[59] P. P. Camanho and C. G. Dàvila, "Mixed-Mode Decohesion Finite Elements for the Simulation of Delamination in Composite Materials," *NASA/TM-2002-211737,* pp. 1-37, 2002.

[60] R. Hill, "The mathematical theory of plasticity," *Oxford University Press, Oxford,* 1950.

[61] M. D. Thouless and Q. D. Yang, "A parametric study of the peel test," *Int Journal of Adhesion and Adhesives,* vol. 28, pp. 176-184, 2008.

[62] I. K. Mohammed, M. N. Charalambides and A. J. Kinloch, "Modelling the interfacial peeling of pressure-sensitive adhesives," *Journal of non-Newtonian fluid Mechanics ,* vol. 222, pp. 141-150, 2015.

[63] S. Tantideeravit, M. N. Charalambides, D. S. Balint and C. R. T. Young, "Prediction of delamination in multilayer artist paints under low amplitude fatigue loading," *Engineering Fracture Mechanics,* Vols. 112-113, pp. 41-57, 2013.

[64] B. R. K. Blackman, H. Hadavinia, A. J. Kinloch and J. G. Williams, "The use of a cohesive zone model to study the fracture of fibre composites and adhesively-bonded joints," *Int. Journal of fracture,* vol. 119, pp. 25-46, 2003.

[65] L. Caillé, J. L. Hanus, F. Delvare and N. Michaux-Leblond, "MFS fading regularization method for the identification of boundary conditions from partial elastic displacement field data," *European Journal of Computational Mechanics,* Vols. 27, pp. 508-539, 2018.

[66] J. Jung, M. Cho and M. Zhou, "Ab initio study of the fracture energy of LiFePO4/FePO4 interfaces," *Journal of Power Sources,* vol. 243, pp. 706-714, 2013.

[67] A. Hallil, J. M. Raulot and M. Cherkaoui, "Atomistic simulations of Cu2O bulk and Cu/Cu2O interface properties by using a new interatomic potential," *Computational Materials Science,* vol. 81, pp. 366-373, 2014.

List of Figures

Figure 1.1: (a) Dispositif utilisé dans les tests de pelage **(b)** Courbe force-déplacement obtenue suite au test de pelage, mettant en évidence deux phases : initiation et régime stationnaire. 3

Figure 1.2: (a) Visualisation de la zone de décohésion avec mesure du rayon de courbure. **(b)** Modèle Eléments Finis développé pour la simulation du test de pelage. 4

Figure 1.3: Force de pelage par unité de largeur en fonction de l'angle de pelage. Comparaison entre expérience et simulation. Deux épaisseurs de cuivre sont considérées : 35 µm et 70 µm. . 8

Figure 1.4: Rayon de courbure en fonction de l'angle de pelage pour des films de cuivre d'épaisseur : 35 µm et 70 µm. Comparaison entre expérience et simulation. 8

Figure 1.5: Printed circuit boards (PCB): **(a)** View of multilayer printed circuit boards and **(b)** Schematic cross section of the PCB [14]**.**..... 12

Figure 1.6: Printed circuit boards (PCB): **(a)** Cross sections of a plated through hole after thermal cycling [14]. Some cracks are observed in the electrodeposited copper and **(b)** Delamination between layers in PCB [15]. 12

Figure 2.1: Peel test: **(a)** A standard peeling machine with a dedicated rig to tune the peel angle [20], **(b)** Load-displacement curve obtained during peeling [19], **(c)** Peel force as a function of the peel angle [11]. 17

Figure 2.2: **(a)** Process zone for an elastic adhesive bonded on a rigid substrate for a peel test at 70° [21]. The film thickness is 50 µm **(b)** Process zone of copper film bonded on a rigid substrate. The film thickness is less than 10 µm [22]..... 17

Figure 2.3: **(a)** Process zone shape at five separate time increments during the steady state regime. The peel angle is 90° [23] , **(b)** Image of the process zone for a 90° peel test where an elliptical profile (red line) is fitted to reproduce the shape of the tape backing [23]..... 18

Figure 2.4: Different peeling behavior of a tape on human skin **(a)** and rigid substrate **(b)** [24] 18

Figure 2.5: Illustration of curvature measurement using digital photography [26]. 19

Figure 2.6: **(a)** Schematic presentation of T-peel test [29], **(b)** A micrograph illustrates the configuration during steady state. The curvatures are measured by considering that circles present the

best fit [29]. 20

Figure 2.7: (a) Peeling of an inextensible film on a rigid substrate. The thickness of the film is **h** and the width is **b**. **(b)** Peel force as a function of peel angle for an inextensible film. Material and geometrical parameters are listed in Table 2.1. 22

Figure 2.8: Peel force versus peel angle: comparison between elastic and inextensible film. Material and geometrical parameters are listed in Table 2.1. Comparison between the Rivlin and Kendall models. 24

Figure 2.9: Elastic film bonded on the rigid substrate, with an initial pre-strain $\varepsilon 1$. The strain $\varepsilon 2$ is due to the presence of peel force **F**. ($\varepsilon 2 = \mathrm{FEbh}$) 25

Figure 2.10: **(a)**: Effect of the pre-strain $\varepsilon 1$ on the peeling force, for small peel angle [11] and **(b)**: Effect of the pre-strain $\varepsilon 1$ on the peeling force, for large peel angle [11]. Parameters are provided in Table 2.1 26

Figure 2.11: Peel force as a function of the peel angle for a visco-elastic film bonded on a rigid substrate [20]. 26

Figure 2.12: (a) Schematic view of the process zone during peeling of elastic-plastic thin film [40] **(b)** Moment versus curvature under plane strain [40]. 29

Figure 2.13: Traction-separation relation governing separation of the interface [4]. 32

Figure 2.14: Cohesive zone for an elastic adhesive film bonded on a rigid substrate [21]. 33

Figure 3.1: Method for preparing specimens used in the peel tests. 37

Figure 3.2: The shape and the dimension of the specimen used for peeling. The 37

Figure 3.3: Tensile set-up used for determining the mechanical response of the material (copper or composite). 38

Figure 3.4: Copper specimen with different orientations for the tensile test. 39

Figure 3.5: True stress versus true strain curves for 35 µm thick copper. Tests are carried out for three orientations 39

Figure 3.6: Copper sample covered with mouchetis made by spray of paint droplets. 40

Figure 3.7: Digital image correlation during the tensile test of copper film. 40

Figure 3.8: **(a)** Stress-strain curves during an uniaxial tensile test on a 35µm thick. Unloadings are

performed to identify the Young's modulus **(b)** Transversal strain-longitudinal strain to identify the Poisson's ratio during unloading. 41

Figure 3.9: Measurement of the copper film thickness **(a)** Optical microscope image for measuring copper thickness, **(b)** Measurement on the 70µm thick film, **(c)** Measurement on the 35µm thick film 42

Figure 3.10: Experimental peeling configuration used in the PhD. 44

Figure 3.11: Force per unit width versus displacement obtained for a peel test at 90°. The peel force corresponds to the average value of the force during steady state. A 35 µm copper film is considered here. 45

Figure 3.12: The initial and final configurations of the peel test specimen. Here the film thickness is 70 µm. 45

Figure 3.13: Evolution of the peel force per unit width as a function of the displacement for different angles: **(a)** 45°, **(b)** 60°, **(c)** 90°, **(d)** 120°, **(e)** 135°. **(f)** Variation of the peel force per unit width as a function of peel angle. Experimental results are obtained for the 70 µm thick copper film. 47

Figure 3.14: Evolution of the peel force per unit width as a function of the displacement for different angles: **(a)** 45°, **(b)** 60°, **(c)** 90°, **(d)** 120°, **(e)** 135°. **(f)** Variation of the peel force per unit width as a function of peel angle. Experimental results are obtained for the 35 µm thick copper film. 48

Figure 3.15 : Determination of the film curvature during peel test. **(a)** Peeling device equipped for the measurement of the film curvature and **(b)** Picture of the 70 µm thick copper film during peeling at 90°. 49

Figure 3.16: Picture of the circle approaching the curvature of the upper surface of the film. The peel angle is 90° and the film thickness is 70 µm. 50

Figure 3.17: Evaluation of the curvature by the circle method. The peel angle is varying in the range 45° to 135°. The film thickness is 70 µm. 51

Figure 4.1: Peel test configuration. The film thickness is h. The peel angle is θ and the force per unit

width is P. The traction separation law is also presented where σ represents the peak stress and Γ the interface fracture energy. A local coordinate system is adopted so that the position z = 0 corresponds to the middle plane of the film. During peeling, the film is facing bending. Let us note R the radius of curvature of the top surface z = h2..... 57

Figure 4.2: Schematic normalized moment versus normalized curvature under plane strain. Letters correspond to specific loading phase during peeling..... 58

Figure 4.3: Elastic-plastic behavior of the metallic film. A Voce type behavior Eq. (4.2) is considered. Depending on the value of γ, the saturation state is approached for different strains. 59

Figure 4.4: Estimated moment curvature relationship for an elastic-perfectly plastic material and a material with a Voce yield stress. Effect of the parameter γ controlling the deformation for which the flow stress saturates, see Eq. (4.2). The reference material parameters are listed in Table 4.1. M_0 is the fully plastic moment. Ke is the elastic limit curvature..... 67

Figure 4.5: Work done by bending plasticity as a function of γ for two values of Q: $Q = 90$ MPa and $Q = 180$ MPa. The reference material parameters are listed in Table 4.1. 67

Figure 4.6: Work done by bending plasticity Ψ versus normalized curvature KKe during bending and reverse bending for two values of $\gamma : \gamma = 40$ and $\gamma = 160$. 68

Figure 4.7 Ratio $\frac{\Psi}{\Psi_{PP}}$ between the work done by bending plasticity Ψ evaluated based on a Voce flow stress and an elastic-perfectly plastic response. Material parameters for the Voce law are given in Table 4.1. 69

Figure 5.1: The geometry and the boundary conditions of the finite element model used for the simulation of the peel test. 73

Figure 5.2: Bilinear traction separation law for pure traction 76

Figure 5.3: Peel force per unit width versus time for different values of material parameters Q and γ. The peel angle is 90°. Other material parameters are presented in Table 4.1. 78

Figure 5.4: View of the film curvature during the bending/reverse bending process. The cohesive elements are removed for presentation purpose. The longitudinal strain ε11 is displayed. A local orientation is adopted. Thus, the direction 1 is always parallel to the central surface,

as presented in Fig. 5.1. 79

Figure 5.5: Effect of the γ parameter of Eq. (4.2) on the curvature KB of the film during a peel test at θ = 90°. The ductile film behavior is elastic-plastic with a yield stress described by a Voce law Eq. (4.2). 79

Figure 5.6: Time evolution of $\varepsilon 11$ within the film thickness for the peel angle $\theta = 90°$. 82

Figure 5.7: Maximum through thickness longitudinal strain captured by the finite element calculations. Comparison with the bending approach for three peel angles: 60°, 90° and 135°. Material parameters are those of Table 4.1 with γ = 40. 83

Figure 5.8: Loading path faced by material points along the thickness during the peeling process. **(a)** Peel angle of 90° **(b)** Peel angle of 135°. A local orientation is adopted in the finite element simulations. The reference parameters are those of Table 4.1 of chapter 4 with γ = 40. .. 84

Figure 5.9: Effect of the peel angle on the estimated interface fracture energy. The predictions based on the present work Eq. (4.22) and on Eq. (4.25) derived for an elastic-perfectly plastic material are compared. The material parameters are listed in Table 4.1 with γ = 40. 86

Figure 5.10: Force per unit width and curvature for various peel angles θ. Note that the cohesive law parameters listed in Table 5.2 are adjusted so that the peel force P(θ = 90°) is preserved. .. 87

Figure 5.11: True stress versus true strain for copper, obtained by performing a tensile test on copper foil: **(a)** 35 µm thick and **(b)** 70 µm thick. 89

Figure 5.12: Plastic response of copper foil fitted by four Voce laws: **(a)** 35 µm thick and **(b)** 70 µm thick. 89

Figure 5.13: Influence of the critical stress σ on the predicted peel force per unit width. A peel angle of 90° is adopted for the numerical model with a Γ value of $202 J/m2$ for Cu35..... 90

Figure 5.14: Influence of the critical stress σ on the predicted radius RC. A peel angle of 90° is adopted for the numerical model with a Γ value of $202 J/m2$ for Cu35 91

Figure 5.15: **(a)** Variation of the peel force at the steady-state versus peel angle **(b)** Variation of the copper film radius at the steady-state versus peel angle. Cu35 film is considered. The parameters of the cohesive elements are: Γ=202 J/m2, σ=230 MPa..... 92

Figure 5.16: F.E Peel test at 90°. Two zones of large von Mises stress are present, which correspond to the area where the material develops plasticity during bending and reverse bending. The simulation is performed for Cu35 film with Γ=202J/m2, σ=230MPa. 93

Figure 5.17: Steady-state peel force as a function of the peel angle for two thicknesses of the copper film. Finite element simulations are performed adopting the identified elastic-plastic behavior of copper and the parameters identified based on a 90° peel test. 94

Figure 5.18: Film radius as a function of the peel angle for two thicknesses of the film. Finite element simulations are performed adopting the identified elastic-plastic behavior of copper and the parameters identified based on a 90° peel test. 94

Figure 5.19: Rate of energies collected for the whole model for various angles: **(a)** 45°, **(b)** 60°, **(c)** 90°, **(d)** 120°, **(e)** 135°. Results are obtained by finite element calculations considering only Cu35 copper. 97

Figure 5.20: Accumulated plastic strain evolution for two elements located at the top and bottom of the film. **(a)** 45°, **(b)** 60°, **(c)** 90°, **(d)** 120°, **(e)** 135°. Results are obtained by finite element calculation considering only Cu35 copper. 98

Figure 5.21: Normal and shear traction-separation laws for **(a)** 60°, **(b)** 90°, **(c)** 135° and **(d)** predicted mixed-mode contribution for different peel angles. Cu35 copper is considered here..... 99

Figure 5.22: Peel force at steady-state as a function of the peel angle for a copper film with thickness: **(a)** h=35 µm and **(b)** h=70 µm..... 100

Figure 5.23: Film radius at steady-state as a function of the peel angle for a copper film with thickness: **(a)** h=35 µm and **(b)** h=70 µm..... 101

List of Tables

Table 2.1: Material and geometrical parameters of the film..... 25

Table 3.1 : Elastic modulus of the woven composite used in printed circuit boards at room temperature. The method proposed in Girard et al [53] is used to capture all components. 43

Table 3.2: Peel force per unit width measured during the steady state region, for the two thicknesses: 35µm and 70µm. 49

Table 3.3: Value of the radius of upper surface of the film (three measurements) and the corresponding value of the radius of the central surface. The copper film thickness is **70µm**. 52

Table 3.4: Value of the radius of upper surface of the film (three measurements) and the corresponding value of the radius of the central surface. The copper film thickness is **35 µm**. 52

Table 4.1 : Reference parameters for the elastic-plastic behavior of the metallic film and for the cohesive law. 65

Table 5.1: Predicted interface fracture energy. From the force and curvature measured owing to finite element simulations (here $\Gamma = 1055$N/m, $\theta = 90°$), the work done by bending plasticity is evaluated based on the present approach (4.22), the approximate solution (4.24) and the elastic-perfectly plastic approach of Aravas et al. (1989) Eq. (4.25). From the energy conservation (4.20), the interface fracture energy is estimated. 82

Table 5.2 : Couples (Γ, σ) leading to the same force per unit width for the peel angle $\theta = 90°$. 86

Table 5.3: Material parameters used to model the plastic response of the copper film for 35 µm and 70 µm thickness..... 90

Table 5.4 : The contribution of GI and GII for Cu35 copper. 99

Table 5.5: Experimental and numerical peel force and copper film radius at different peel angles for Cu35 copper. 101

Abstract

In this thesis, the identification of the interface strength in Printed Circuit Boards (PCBs) is assessed. A PCB is a passive component which allows to interconnect electronic components soldered on the outer layers in order to realize a complex electronic system. It is a multiple layer assembly made of woven composite and copper foil. Copper plays a major role in Printed Circuit Boards (PCBs) since it is the carrier of the electrical information. During its lifetime, the PCB undergoes a large number of thermal cycles which can lead to the failure of copper path. In addition, it has been detected that the use of certain combinations of based materials leads to delamination, which limits the PCB service-life. The measurement of interface strength between copper layer and composite substrate is critical and the usual method for measuring the interface properties in PCB industry is the peel test.

The PhD is divided in three main parts.

In the first experimental part, peel tests at various peel angles are performed using specimens which consist of a copper foil bonded on a woven composite substrate. Interface separation between the copper film and the composite substrate is observed. During the test, the peel force per unit width and the copper film radius at steady state are measured.

Next, a theoretical analysis of the peel test for an elastic-plastic material is proposed. A precise definition of the work done by bending plasticity for a particular class of material response is established. Indeed, we have extended previous works of the literature by considering that the plastic hardening behavior of the film is modeled by a Voce type law.

Finally, finite element (FE) simulations of peeling are conducted at various peel angles by considering that the copper material response is elastic-plastic. The isotropic hardening is identified based on uni-axial tensile tests. The woven composite is assumed to remain elastic with an orthotropic response. The interface is modeled by cohesive elements using a bilinear traction separation law. FE results are compared to experimental data. It is shown that the peel force and the film curvature are predicted accurately, for a large range of peel angles.

Therefore, from the dialog between finite element calculations and experiments, the interface fracture energy is obtained.

Keywords: peel test, interface energy, thin film, cohesive elements, modeling, interface strength

Résumé :

Dans cette thèse, la résistance des interfaces dans les circuits imprimés (PCB) est étudiée. Un PCB est un élément passif permettant d'interconnecter des composants électroniques soudés sur les couches externes. Un PCB est un assemblage multicouche, multi-matériaux fait de composites tissés et de feuillards de cuivre. Le cuivre joue un rôle majeur dans les circuits imprimés car il est le support de l'information électrique. Pendant son cycle de vie, le PCB subit un grand nombre de cycles thermiques pouvant entraîner la rupture des fûts de cuivre. Par ailleurs, l'utilisation de certaines combinaisons de matériaux peut entraîner du délaminage ce qui limite la durée de vie du PCB. La mesure de la résistance de l'interface entre la couche de cuivre et le substrat composite est alors très importante. Pour l'industrie du PCB, le test de pelage reste la méthode courante pour mesurer les propriétés de l'interface entre deux matériaux.

Cette thèse comporte trois parties.

Premièrement des tests de pelage sont réalisés pour différents angles de pelage et à température ambiante. Les échantillons étudiés et testés sont constitués d'un feuillard de cuivre assemblé à un substrat composite tissé. Lors de l'essai, la décohésion au niveau de l'interface est bien observée. Par ailleurs, la force de pelage et le rayon de courbure du film de cuivre sont mesurés en régime stationnaire.

En parallèle, une analyse théorique du test de pelage est conduite pour des matériaux élasto-plastiques. Le chemin de déformation du film de cuivre lors du test de pelage est assimilé à un mode de flexion – flexion inverse. Nous proposons une analyse théorique de ce trajet de chargement pour un matériau élasto-plastique obéissant à une loi d'écrouissage de type Voce.

Enfin, des simulations de pelage par éléments finis sont effectuées pour différents angles. Le comportement du cuivre identifié à l'aide d'un essai de traction est considéré comme élasto-plastique. Une loi d'écrouissage de type Voce est utilisée. Le substrat est supposé élastique orthotrope. L'interface est modélisée par des éléments cohésifs en utilisant une loi de type traction séparation bilinéaire. Les résultats des simulations (EF) sont comparés aux données expérimentales de la thèse. On observe un bon accord au niveau à la fois de la force de pelage mais aussi du rayon de courbure.

Au final, ce travail de thèse permet de proposer un dialogue essai / simulations numériques pour définir précisément l'énergie de rupture de l'interface.

Mots clés : test de pelage, énergie d'interface, film mince, éléments cohésifs, modélisation.